Silicon-based titania coated anodes for lithium-ion capacitors

Mats Rødne

Master Thesis in Materials, Energy and Nanotechnology (MENA)

60 ECTS credits

Department of Chemistry

The Faculty of Mathematics and Natural Sciences

Submission date: 30.06.2022

2022

Silicon-based titania coated anodes for lithium-ion capacitors

Mats Rødne

http://www.duo.uio.no/

Printed: Reprosentralen, University of Oslo

Abstract

Lithium-ion capacitors are promising energy storage devices aiming to bridge the performance differences between battery's energy density and capacitors power density. In this project we aim to bypass the inconvenient process of pre-lithiating the anode in LICs, by using atomic layer deposition (ALD) grown titania (TiO_2) grown on Si-electrodes

Different coating thicknesses of TiO_2 was tested to show their effect on the performance of the cells. The electrodes of Si and Si@TiO_2 were tested in half cells using Li-metal as counter electrodes. As cathodes for full cells, activated carbon (AC) electrodes were used due to their high surface.

The capacity of Si@TiO_2 electrodes with 5 and 8 nm coatings of TiO_2 were measured to be stable at 13.3 and 45.2 μAh/cm^2, after 5000 cycles at 34 μA/cm^2. AC|Si@TiO_2 full cells with coatings of 5 and 8 nm showed a capacity of 350 μAh/cm^2 at currents of 17 μA/cm^2 and 50 μAh/cm^2 at currents of 34 μA/cm^2. The samples stabilized at 13 and 17 μAh/cm^2 for currents of 340 μA/cm^2. The full cells showed great capacity retention and no capacity degradation after rate capability tests.

With the use of cyclic voltammetry, the means of storage was determined for both half cells and full cells fabricated in this project. The first half cells of Si|Li have Faradaic charge transfer through redox reactions, as is known for LIBs. For the full cells of AC|Si@TiO_2 they initially show Faradaic charge transfer through redox reactions before shifting to pseudocapacitive mechanisms as known for SCs.

Keywords: Electrochemical energy storage, Li-ion capacitors, anatase titanium dioxide, atomic layer deposition, porous electrode coating, atomic layer deposition.

Acknowledgements

This project was carried out in the Nanostructures and Functional Materials (NAFUMA) group at the University of Oslo. NAFUMA is part of the Department of Chemistry and Faculty of Natural Sciences. This is a joint work between the Institute of Energy Technology (IFE) and the NAFUMA group at the UiO. I would like to start and thank everybody in the NAFUMA group for all the wonderful weekly meetings and events through the year. Secondly, I want to thank all nice people over at IFE for always helping me when suddenly being asked questions by some random student from the UiO.

The first person I want to thank, is my main supervisor associate Professor Alexey Y. Koposov for making this project possible. I really appreciated all the informative discussions we shared, and that you always are available, even though you have a hectic life. I also want to give a special thanks to my second supervisor, Professor Ola Nilsen, for asking me the important questions, giving me the tools to answer them and being the mind behind all the activity regarding ALD.

Many thanks to my supervisor over at IFE, adjunct Professor Samson Y. Lai for our long and educating discussions through the last year, and for always seeing the positive in every situation. I would like to extend my sincere thanks to my fourth supervisor, Doctor Carmen Cavallo, for practically running the laboratory while teaching me and everybody else everything there is to know about anything.

Ander Brennhagen also deserves a special thank for always dropping everything to come and help me fix one of the many things that I broke during my master project. I am also thankful for Veronica Anne-Line Kathrine Killi teaching me how to operate the ALD reactor, motiving me through tough times, and always checking in on me. Furthermore, I want to thank Martin Jensen for helping me with the SEM.

Before ending, I need to thank all family and friend for sticking with me through this process. At last, I want to thank my fiancé, Ingrid, for all the love and support you have given me through this hectic time. You are truly my everything.

Abbreviations

a-TiO_2	Anatase TiO_2
AC	Activated carbon
AC| Si@TiO_2	Indicates Cathode|Anode. In this example, the active material on the cathode is AC, and the active material on the anode is Si@ TiO_2.
ALD	Atomic layer deposition
BSE	Backscattered electrons
BET	Brunauer-Emmett-Teller theory
CV	Cyclic voltammetry
CVD	Chemical vapor deposition
DoD	Depth-of-discharge
EDS	Energy dispersive spectroscopy
GC	Galvanostatic cycling
GPC	Growth per cycle. Related to growth rate
HSC	Hybrid super capacitor
LIB	Li-ion battery
LIC	Li-ion capacitor
MSE	Mean square error
n	Index of refraction
NAFUMA	Nanostructures and functional materials – research group at the University of Oslo
OCV	Open circuit voltage
RE	Reference electrode
RTIL	Room temperature ionic liquids
SC	Super capacitor
SEM	Scanning electron microscopy
SE	Secondary electrons
SEI	Solid electrolyte interphase
Si@ TiO_2	TiO_2 deposited on silicon electrode
WE	Working electrode

Terminology

Active material	The active material is generally referred to as the electrochemically active material participating in the charge transfer processes and which interacts with alkali metal ion (Li^+ in LIBs). For Si-based anodes it is Si that is the active material, even though the electrode also contains small amounts of graphite, carbon black and CMC.
ALD window	The range of experimental conditions at which the ALD growth is stable.
ALD cycle	An ALD cycle is defined as the sequence of "purge–precursor1-purge-precursor2", which is repeated through the course of an experiment.
Anode	The electrode going through oxidation (delithiation in LIBs) during discharge, also referred to as the negative electrode. It has the lowest potential *vs* Li^+/Li of the two electrodes in a full cell.
Areal capacity	The total capacity of the electrochemical cell divided by the area of the electrode.
Battery	A battery refers to a single secondary (rechargeable) electrochemical cell.
C-rate	A description of a rate at which an electrode (or battery) is discharged or charged relative to its capacity. 1C indicates that the full theoretical capacity of the battery is emptied in 1 hour.
Cathode	The electrode going through reduction during discharge also referred as the positive electrode. It has the highest potential *vs* Li^+/Li of the two electrodes in a full cell.
Capacity retention	The ability of a cell (or electrode) to maintain its capacity during cycling. A perfect capacity retention will have Coulombic efficiency of 100 %. A low capacity retention is indicative of side reactions and/or poor material stability. A high capacity retention typically leads to a high cycle life.
Coating (ALD)	An ALD process herein describes deposition of a thin film of a material (TiO_2 in the present work) on the surface of an electrode. In this project the ALD coatings have thicknesses in the range of 2 – 30 nm.
Coating (Slurry)	The process of applying a wet slurry on top of the current collector for the preparation of electrode. When dried, this will result in an electrode. In this work the slurry coatings have a thickness around 75 – 300 µm with Si, AC or SiP_x as active materials.

Coulombic efficiency	The Columbic efficiency is the ratio between the total charge that is actually taken out of the battery during discharging compared to the total charge that was put into the battery during charging.
Counter/ reference electrode (CE/RE)	In this project only 2-electrode set-ups are being used. The RE and the WE will therefore in both cases be the Li-metal in the half cells. This is a non-ideal RE and CE as it is involved in the process and current is running through it.
Cyclic voltammetry	An electrochemical technique, where a cell is tested with a constantly changing applied voltage (with a constant rate), while measuring the current. Abbreviation: CV.
Cycling	The term describing "going through cycles". This is true for both an electrochemical cycle and an ALD cycle.
Depth-of-discharge (DoD)	Defined as the amount of charge removed from the battery divided by the total available amount of charge in the battery. Cycling at a DoD of 30% will only draw out 30% of available charge during a cycle.
Differential capacitance plot	Change in capacity per change of voltage, dQ/dV and derived from GC data. The technique is complementary to CV and generally used for evaluation of redox processes.
Electrochemical cycle	An electrochemical cycle is defined as when an electrochemical cell is both charged and discharged.
Full-cell	An electrochemical cell, where both cathode and anode are present. The capacity contribution of the electrodes needs to be balanced.
Galvanostatic cycling	Cycling the batteries with a fixed current, while measuring the change in voltage. Abbreviation: GC.
Growth rate	Describes how fast the Si@TiO_2 film grows on the films during ALD. Related to GCP.
Half-cell	An electrochemical cell having Li-metal as RE versus the WE. Such cells are used to evaluate the electrochemical performance of the WE (either cathode or anode).
Loading	The loading of the battery refers to the amount of electrochemically active material in the battery. The current being applied to the cell during cycling is proportional to this.
Primary cell	Primary cells are electrochemical cells that are not rechargeable.
Room temperature	Defined as 25 °C. It is common to use this temperature for electrochemical testing of batteries. Temperature has a great impact on electrochemistry, ref. Nernst equation.
Secondary cell	Secondary cells are electrochemical cells that are rechargeable.

Specific capacity	The ability to store lithium (Li) per unit of weight. Units: mAh/g.
$Si@TiO_2$	$Si@TiO_2$ refers to an Si electrode being coated with TiO_2. The TiO_2 will be the active material, and the Si would work as a “scaffold” holding up the TiO_2 structure.
Working electrode	Defined as the electrode where the reactions are taking place. In half-cells with Li-metal, this will be the other electrode than the Li-metal electrode. In this project, working electrodes being used as Si, SiP_x, $Si@TiO_2$ and AC.

Table of Contents

Table of Figures

1. Introduction

Today's society aims to gradually reduce and ultimately eliminate the use of energy obtained from non-renewable sources. However, many of the renewable energy sources are intermittent, such as wind turbines and solar cells. As a result, the harvested energy needs to be stored so that it can be promptly delivered to the consumers when it is needed. Furthermore, to fully rely on renewable energy sources, it is expected that a combination of energy storage solutions will be used to account for the different intermittency of the energy sources. For instance, the efficiency of solar cells and windmills are highly dependent on uncontrollable factors such as light intensity and wind velocity, which varies greatly over time.[10,11,12] Energy storage solutions differ by the energy stored and power output, and they can therefore be designed for a specific application.

Windmills can go from producing vast amounts of energy to almost nothing within minutes. Solar panels have daily cycles of electricity production as they are dependent on the intensity of light. Solar cells tend to have a more predictable energy production; but since solar cells produce negligible amounts of electricity during night, power shortages will occur every night without complementary energy storage.

To effectively store the harvested energy from intermittent energy sources, a combination of lithium-ion batteries (LIBs), supercapacitors (SCs), and capacitors are expected to be used as stationary energy storage (i.e., for electrical grid stabilization). Capacitors and SCs are currently used to compensate for the quickest changes in energy production. Their ability to charge/discharge in the range of milliseconds to seconds makes them ideal for both receiving and delivering large energy bursts for short periods of time. LIBs normally use over 15 minutes to charge/discharge but can store substantially more energy per unit than the capacitors and supercapacitors. This makes the LIBs ideal for the long-term storage of large amounts of energy, while capacitors and SCs could be used to flatten the peaks in the energy production. However, the energy storage capacity of capacitors and SCs alone is not sufficient for such applications.

Li-ion capacitors (LICs) have been designed to deliver a better balance between the energy density and power density of SCs and LIBs. The schematic Ragone plot in Figure 1 illustrates that LICs do in fact deliver the properties somewhere between LIBs and SCs,[7]. The Ragone plot compares the power density with the energy density for these energy storage solutions, displaying the amount of energy that can be stored in a device vs. the rate at which the energy can be extracted.

At present, LICs still have only a minor market share compared to other energy storage solutions; however, the performance benefits in terms of balance between power and energy make LICs an ideal addition to current energy storage systems. With further development, LICs will find their market and become as normal to consumers as capacitors and LIBs.

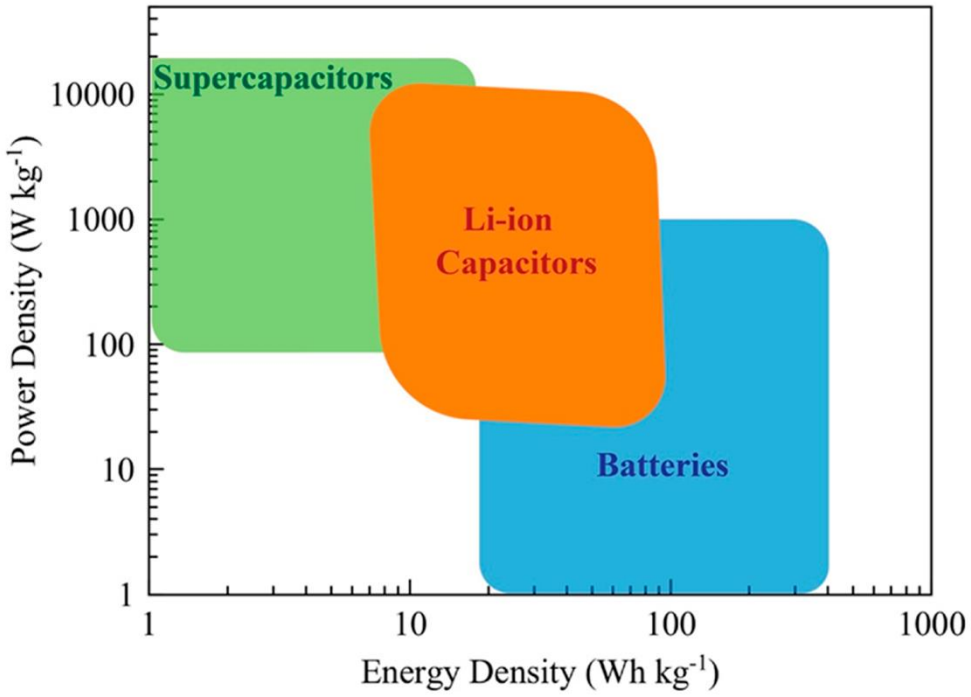

Figure 1: Ragone plot illustrating the relation between the amount of energy per kg stored in a device (energy density) vs. the work to be done by a device per unit of time per kg (power density). Reproduced from Lai et al.[7] under the terms of the Creative Commons Attribution 4.0 license.

In this chapter, additional background and the goals of the project will be defined. This will be followed by a historical overview of the electrochemical energy storage, focusing primarily on LIBs and hybrid super capacitors (HSCs).

1.1. Background

LICs and LIBs both use Li-ions to transfer charge inside the cell, which means there needs to be a source of Li somewhere in the system.

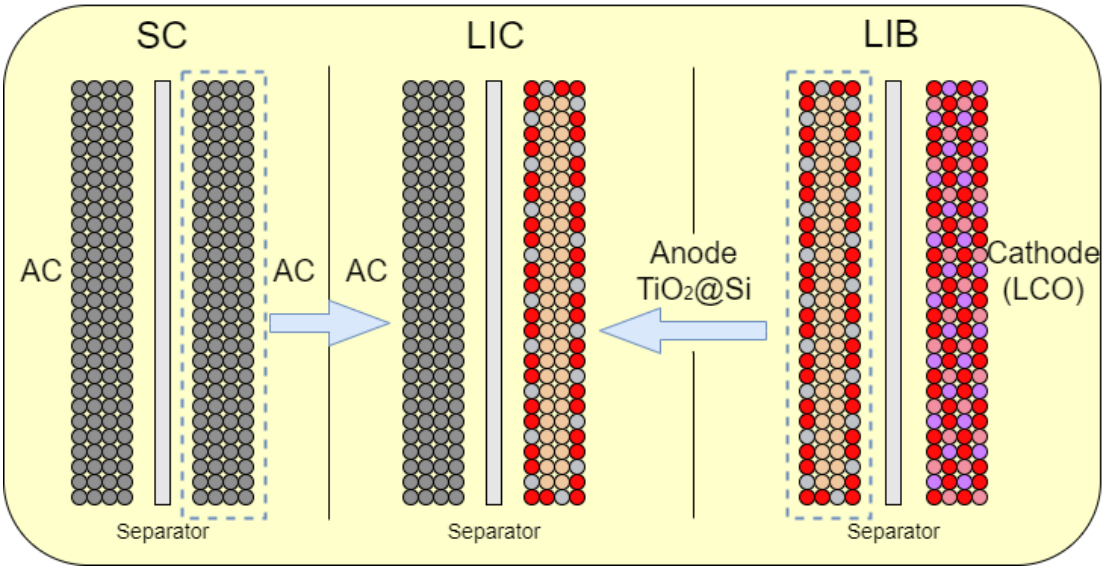

Figure 2: Schematic of comparison between a capacitor, SC, and LIC. The LICs have a LIB anode as its anode and one of the electrodes from the SC as its cathode. In this case, the LIB anode is a Si electrode coated with TiO_2, while the SC has two AC electrodes. As the positive electrode for the LIB, a schematic LCO cathode has been used. Dark-grey is used to represent carbon atoms, while light-grey is titanium (Ti). Red is oxygen(O), while beige is Si. Purple is Li. The red/blue color is cobalt.

Figure 2 illustrates how the LIC is a combination of one electrode from the SC and the anode from the LIB. In this illustration, AC electrodes are chosen for the SC, while a TiO_2 coated Si ($Si@TiO_2$) anode is chosen for the LIB. This approach is relevant to this project as the LIC represented is the LIC currently being studied.

There are, however, some challenges occurring when going from an LIB to an LIC. In LIBs, the important Li is integrated in the structure of the cathodes, as it is with LCO ($LiCoO_2$), NMC ($LiNiMnCoO_2$), and LFP ($LiFePO_4$). LIBs can therefore make use of the cathode as its source of Li during cycling. As seen in Figure 2, the LIC loses its source of Li as it exchanges the Li-containing LIB cathode with a Li-free SC electrode.

Li is essential for doing faradaic charge transfer through redox reactions in LIBs and LICs. The result of this is a system dependent on Li that does not have a source of Li. The exception is the Li that is contained in the electrolyte, which will be discussed later in this thesis.

Today, the lack of Li in the LICs is solved by pre-lithiation of the anode.[7] Pre-lithiation is the process of filling the electrode with Li, prior to making a full cell. There are many methods for doing this, which will be discussed later in this thesis. Each of the methods is, in one way or another, either expensive, complicated, time-consuming, or not scalable. Therefore, it is beneficial to remove pre-lithiation in the process of efficiently producing LICs.

1.2. Objectives

The primary objective of this project is to evaluate thin films of TiO_2 on Si electrodes (Si@TiO_2) as anodes for LICs without pre-lithiation. The purpose of this project is not to create a stabilizing layer on the Si electrode, but to create a thin film of electrochemically TiO_2 on top of a silicon electrode. The Si-electrode will act only as a "scaffold" holding up the TiO_2 structure and increasing its surface area. TiO_2 shows lower capacity than Si but has a higher capacity retention and cycle lifetime, making it more ideal for LICs. The TiO_2 thin films in the range of 3–15 nm will be synthesized using ALD for maximal thickness control.

One of the secondary objectives to help answer the primary objective will be to successfully obtain Si@TiO_2 electrodes using ALD. Half cells of AC, Si, SiP_x, and Si@TiO_2 electrodes will be tested and analyzed to balance the capacity of the anode and cathode in the full cells. It will be a secondary objective to achieve specific capacities of 500 mAh/g from Si and SiP_x after 100 cycles. This will be tested with active masses around 1 mg and currents of C/10. Half cells of Si@TiO_2 should have an areal capacity of 50 µAh/cm^2 for 5000 cycles at current rates at 17 µAh/cm^2. The capacity of the cell as well as the storage mechanism can be determined by doing CV scans of the samples and GC measurements of the half cells.[13-15]

To answer whether or not the coatings are successful, it will be essential to characterize the coated electrodes using ellipsometry and SEM. Ellipsometry will tell the thickness, gradient, and penetration through pores of the TiO_2 coating on the electrode. SEM pictures will serve as a qualitative evaluation of the electrode structure and agglomeration of particles. It will also give an estimated particle size of the Si particles.

Using GC and CV, electrochemical testing will also be made of all electrodes to determine how they work in a half or full cell. CV scans before and after rate capability tests show the mechanism of storage by examination of oxidation/reduction peaks. The CV scans for full cells will be done twice at 0.1 mV/s for 3–5 cycles.

Two kinds of GC measurements will be performed. The first is a rate capability test where the capacity at stepwise currents from 8–340 $\mu A/cm^2$ as well as capacity retention during high currents are being tested. A long-term GC will follow the rate capability test and will show the capacity retention over time for low currents. All tests will be done with different coating thicknesses to evaluate the impact the TiO_2 has on areal capacity and capacity retention at both high and low currents.

The primary objective will be answered by analyzing the results from the GC and CV measurements of full cell LICs. These LICs are AC|Si and AC|Si@TiO_2 full cells with different coating thicknesses. A successful LIC component should achieve areal capacities close to 25 $\mu Ah/cm^2$ at high currents and up to 400 $\mu Ah/cm^2$ at low currents. The LICs should also have a high-capacity retention close to 80% after 500 cycles when cycled at 1 $\mu A/cm^2$. These numbers are based on results from the literature.[14-16, 17] The capacities of various LICs will be compared to each other and half cells in this project to determine the impact of the coatings on capacity and capacity retention.

The hypothesis being tested is that the amount of available Li in the electrolyte will be enough to drive the faradaic redox reactions in the LIC. The question to be explored is whether this will come at the expense of drying out the electrolyte and thereby decreasing the ionic conductivity. The hypothesis is based on the assumption that during shallow cycling, only a small portion of the Li in the system will be needed to operate the cell. The reasoning behind this hypothesis, definitions of terms such as shallow cycling, and the discussion of the results will be discussed later in this thesis.

1.3. Historical background

In this section, the historical progress of the lithium-ion battery (LIB), the supercapacitor (SC), and atomic layer deposition (ALD) will be presented.

1.3.1. Li-ion battery (LIB)

In 2019, the Nobel Prize in Chemistry was awarded to John. B. Goodenough, M. Stanley Whittingham, and Akira Yoshino "for the development of Li-ion batteries."[18] The Li-ion battery's high power-density and rechargeability enables it to replace most other competing battery technologies, such as the lead acid battery. This offers a unique opportunity to improve the mobility of components such as electrical vehicles, mobile phones, and laptops. [18]

1.3.2. Whittingham - Proof of the rocking-chair concept

The foundation of the LIB was laid during the oil crisis of the 1970s when Stanley Whittingham worked on an alternative to fossil-fueled energy storage systems. His work on superconductors led him to the discovery of a material capable of housing Li-ions, a process Whittingham defined as intercalation.[19] The material was made from titanium disulfide, and from 1976 to 1978 it served as the first cathode material for Whittingham's employer Exxon as their patented rechargeable battery.[20] The anodes being used together with this cathode were either Li-metal or LiAl, providing an energy density somewhere between 40 and 45 Wh/kg and a voltage of 2.2 V.[20] Another great advantage was that there is no phase transformation for Li_xTiS_2 ($0 < x < 1$) during full intercalation. Irreversible phase transitions are often a degrading mechanism as the aim is to leave the host (the electrode hosting Li) as unchanged as possible during cycling.

Other battery chemistries were also tried such as Li/MoS_2, Li/V_2O_5, Li/V_3O_8, and Li/MnO_2.[20] In each of these cases, the anode consists of Li-metal, and the cathode is a mix of a d-block metal and a chalcogen. The choices for both cathode material and anode material today are mainly based on the same logic as Whittingham used—and this will be discussed further in the section on theory.[21] Despite it was promising, Exxon ended the project because of the major safety issues connected to the formation of dendrites on the electrode.

The LCO was the first "rocking chair"[20] battery, later known as Li-ion battery (LIB), and the reason behind its name was that the electrodes acted as both source and sinks for the Li-ions. (The principles behind this will be further discussed in the section on theory.)

1.3.3. Goodenough – Father of the good enough cathode

The LFP battery was patented in 1996 by J. B. Goodenough et al.[22] This is the same man who in 1980 invented the LCO ($LiCoO_2$) battery.[20] This work was inspired by the work of Hagenmuller et al., who were studying Na_xCoO_2.[23] LCO benefits from better conductivity and higher stability in air than the $NaCoO_2$ battery. Today, many researchers aim to replace the Li with Na, as Na is more abundant and evenly distributed throughout the world.

The LCO cathode material revolutionized the battery world, and these cathodes have become the most commercialized one in recent years.[23] The LCO battery is still widely used today but is losing market share to newer technologies such as the LFP mainly because of cost, safety, and performance. The LCO battery system developed by Goodenough increased the nominal voltage of the system from 2.5 to 3.9 V vs Li^+/Li.[23] Goodenough's work led to new ideas such as the $Li(Ni_xMn_yCo_z)O_2$ (NCA) cathode material. The utilization of oxides together with metals that are proximate to cobalt in the periodic table of elements (Ni, Mn, Fe) became a trend that continues today in the development of cathode material.

The pristine LFP developed by Goodenough's group has some drawbacks, such as poor electronic conductivity (less than 10^{-9} S cm^{-1}), which in turn leads to high impedance.[24] Combined with a low rate of Li-ion diffusion (around 10^{-15} cm^2 S^{-1}), this should not have been a popular choice for cathode material. However, the properties were enhanced by using nano particles of LFP and then coating the surface of these particles with a carbon layer. Using nanoparticles reduces the diffusion distance and provides a large surface for exchange of electrons and ions. The size should be under 50 nm in order to obtain sufficient tunnelling of electrons. The carbon coating is normally done by pyrolysis and increases the conductivity significantly by increasing the kinetics of the surface electron charge transport. Because of their good cycling stability, cheap production, long cycling life, and high thermal stability, LFP LIBs are among the most used cathode materials today.[21,24]

1.3.4. Akira Yoshino – Safe anode

For a long time, metal Li was used as anodes for batteries; however, significant safety issues required this material to be replaced if the Li battery were ever to be commercialized.[23] The safety issues were connected to the uncontrollable formation of dendrites that lead to short-circuiting the battery cell, resulting in highly self-sustaining battery fires. The solution was patented in 1985 by Ashani Chemical Ind., Japan, based on the work of Yoshino et al.[23] Yoshino proposed to use a carbonaceous material (petroleum coke) as an anode for the Li-ion battery.[23]

1.3.5. More on carbon-based anodes

The possibility of inserting Li into graphite had already been demonstrated in 1955 and proven by synthesis in 1965.[23] This was before Ashani patented Yoshino's carbon-based anodes and his demonstration that this could be performed electrochemically. Later in 1976, the electrochemical insertion of Li into graphite was performed by Besenhard and Eichinger.[23]

At this time graphite was studied as a cathode material, according to Reddy et al.,[23] but it was discarded because no suitable electrolytes were able at the time to prevent co-intercalation

in the system. Co-intercalation differs from intercalation in that it inserts solvated ions instead of ions into the structure which, in this case, is graphite.[25] Co-intercalation is a particular problem for graphite and the solvents used at that time (e.g., propylene carbonate, PC) because it results in the exfoliation of graphite.[26]

1.3.6. The quest for the right electrolyte

Armand et al. proposed a solution in 1978 to the problem of co-intercalation by developing a polymer electrolyte.[23] By using this electrolyte, Armand et al. could prove that graphite was indeed a suitable and stable anode material. This was a solid-state electrolyte that benefits from being highly stable, which makes it safe, while having low self-discharge and high cyclability. The major drawback has always been balancing the poor ionic conductivity with the attributes of a satisfactory price, electrode combability, stability, and performance. Armand et al. also made a full-cell battery that allows both the cathode and anode to intercalate Li-ions into its structure. By having Li-ions go back and forth between the electrodes during charge/discharge, the battery was called a "rocking chair battery," based on the principles Whittingham et al. had proven with the LCO cathode battery system.[20] The "rocking chair battery" (or "shuttle battery") was later renamed "Li-ion battery (LIB)."[27]

Another solution to the problem of the exfoliation of graphite was to use another liquid electrolyte. One of the first successful alternatives was ethylene carbonate (EC).[26] EC has the significant advantage that it creates a stable solid electrolyte interface (SEI) layer on the graphite to keep it from exfoliating.[26] (The SEI-layer is a complicated concept that will be discussed in a later section.) By using EC as the organic solvent in the electrolyte instead of PC, Dahn et al. produced the first recyclable Li-ion battery with graphite.[26] At this stage the LIB was commercialized with great success by Sony and Asahi (Yoshino) with an LCO cathode and hard carbon anode.[23,26]

PC was the original electrolyte solvent; however, after discovering the efficiency of EC, Guyomard and Tarascon in 1993 introduced mixing dimethyl carbonate (DMC) as solvents in the electrolyte, creating a new super electrolyte.[26] The LP30 electrolyte that is used today in graphite LIBs throughout the world is 1.0 M $LiPF_6$ dissolved in 1:1 EC: DMC. Additives such as vinylene carbonate (VC) and fluoroethylene carbonate (FEC) have also been added to the electrolytes in order to passivate and enable the SEI to maintain a certain thickness.[28] From 1994 to the present, almost all commercial LIBs contain graphite (in larger or smaller amounts) in their anodes, as it is abundant, cheap, reliable, has good capacity retention, and is safe.

1.3.7. The history of supercapacitors

Supercapacitors (SCs) are a subsection of capacitors that rely instead on a solid dielectric and use an electrostatic double layer (EDL) for capacitance. For this reason, SCs are often referred to as chemical capacitors.[29] Pseudocapacitors and hybrid capacitors also utilize faradaic electron transfer reactions such as redox reactions.[29] The theoretical framework that describes how the non-faradaic electron transfer occurs in supercapacitors is described by Helmholtz, Stern, Grahame, Gouy, and Chapman.

Figure 3 illustrates the differences between these methods of energy storage. Helmholtz was the first to show that charged electrodes, combined with an electrolyte containing charged particles, will apply a force on charged ions in the solution. The electrodes will therefore have a larger concentration of oppositely charged ions close to them. The result is a molecular dielectric that can maintain electrical charge electrostatically—called the electric double layer (EDL).[29] The amount of charge this EDL could hold was provided by a linear relation of the voltage applied to the system in the operation voltage window where the electrolyte is stable.

This was later modified by both Gouy and Chapman, working separately, to be dependent on the ionic concentration as well. With the use of Maxwell-Boltzmann statistics, it was demonstrated that the electrical potential decreases exponentially away from the interface between electrodes and electrolyte. A merging of these models was proposed by Stern to compensate for the highly charged ions, which the model does not account for. In the new theory, Helmholtz's idea of ions sticking to the surface of the electrodes is considered a partial explanation, while the rest of the ions create a diffusion layer, as proposed by Gouy and Chapman.[29] The inner layer can be used to determine the size of the ions and is used in determining the ionic radii in this case.[29]

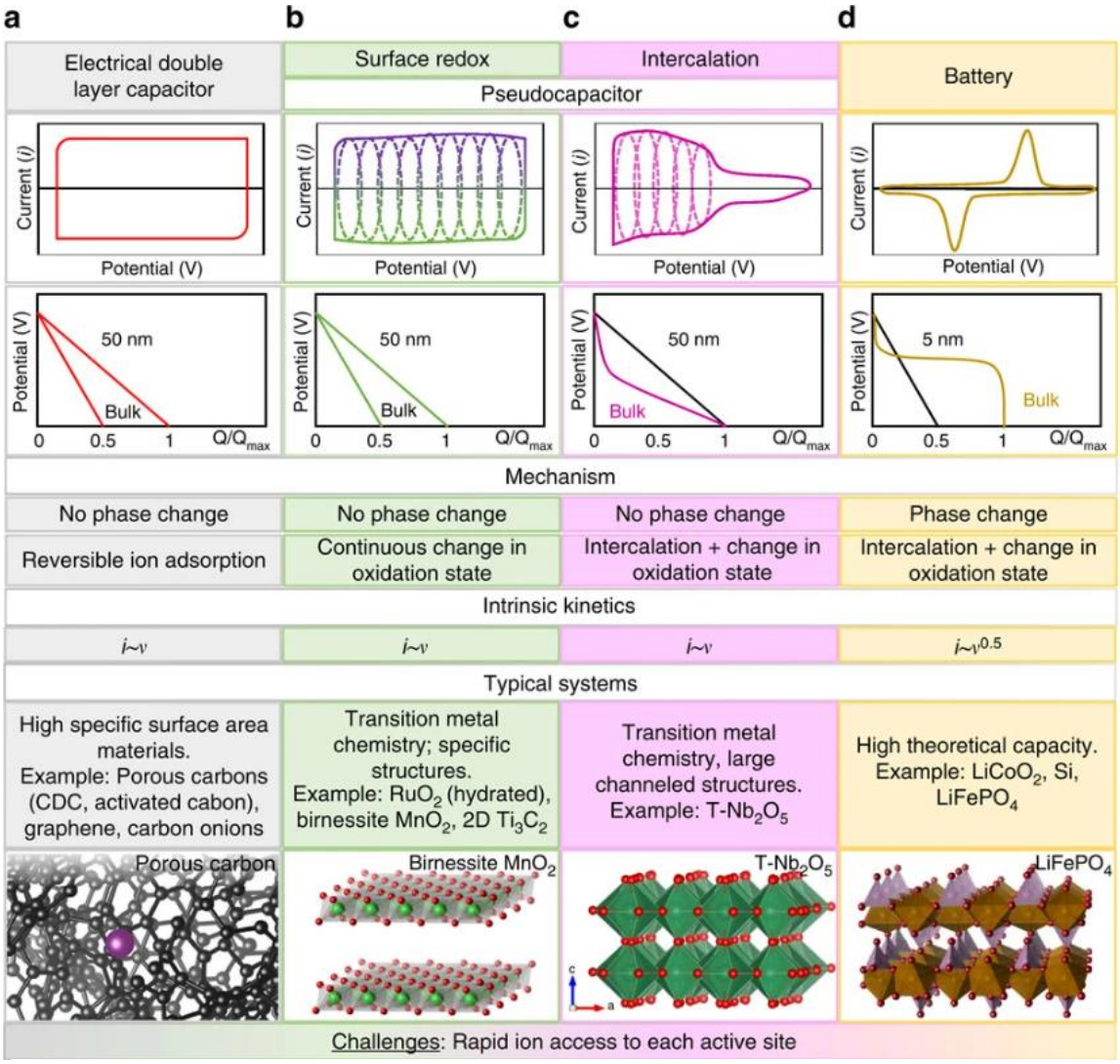

Figure 3: Figure describing the different means of storage for capacitors, batteries, and pseudocapacitive mechanisms. The first line of figures shows CV plots of the various components. The last line of figures shows an atomic representation of one of the different systems listed in the section above, where typical systems are listed. The kinetics are also described by relating the voltage to the current of the CV plots. Reproduced from Lukatskava et al. with permission under the CC BY 4.0 license.[8]

The limitations of the model, as improved by Stern, are as follows: it treats ions as point charges, it assumes that all the interactions are Columbic and that the viscosity of the liquid electrolyte is constant, and it assumes that the dielectric permittivity comes through the EDL. Grahame proposed that, despite normally being a layer of solvent molecules occupying the space closest to electrodes, it is possible that some ions could go through this layer if some of the ions loses their capsule of solvent molecules. The model consists of three regions: the inner Helmholtz plane (IHP), the outer Helmholtz plane (OHP), and the diffuse layer.

The model has been adjusted several times later, including adjustments in how the solvent aligns to the charged electrodes in the double-layer. Through the study of ruthenium dioxide films, the researchers showed that a charge transfer takes place between the electrode and the ions in direct contact with the electrode. This finding was a contribution to the term "pseudocapacitance," which stated that redox reactions also take place in some supercapacitors in the form of intercalation (or insertion, alloying, or conversion), in addition to the non-faradaic electron transfer one can see in the EDLCs. These reactions form the foundation of the pseudocapacitors.

In the 1990s three pseudo capacitive processes were described by Conway et al.[30] as follows:

> i) *the underpotential deposition occurs, when the cations in the electrolyte form an adsorbed monolayer on the surface of different metal electrode at a certain potential, which is well above their redox potential.*
> (ii) the redox pseudocapacitance that happens when, ions are specifically adsorbed through electrochemical means at the surface of an electrode (i.e., electrode/electrolyte interface) with a simultaneous faradaic charge-transfer,
> the intercalation pseudocapacitance occurs, when ions intercalate into the a redox active host material accompanied by a faradaic charge transfer without crystallographic phase change.[31]

From this the distinction between faradaic and pseudo-faradaic needs to be made. Faradaic electron transfer is related to the bulk of the active material and is limited by the diffusion to the material bulk.

For batteries, faradaic processes such as redox reactions, which change the oxidation numbers of the active material, are made possible by alloying/intercalating/inserting/converting cation ions into the active material during cycling. Pseudo-faradaic electron transfer is sometimes described as "surface-limited electron transfer" as it is only the surface of the active material that contributes to the reactions. This makes pseudo-faradaic reactions, as seen in pseudocapacitors, mainly limited by the surface and not diffusion as it is in the faradaic processes in batteries.

There is a clear advantage in utilizing pseudocapacitors that rely on surface limited pseudo-faradaic electron transfer as compared to the diffusion-limited faradaic electron transfer in the bulk of the active materials in batteries: pseudocapacitors can release and store energy more quickly, hence yielding higher power density.[31] The battery has the advantage that it can store more energy inside its structure, making it reach higher capacity densities.

Naskar et al. stated that the combination of non-faradaic, pseudo-faradaic, and faradaic electrodes opens up possibilities for optimizing the energy-power characteristics of these components.[31] By combining various supercapacitors/battery electrodes that exhibit different kinds of faradaic behavior, another subsection of supercapacitors emerges—namely, hybrid capacitors.[7]

As a subsection under hybrid capacitors, Li-ion capacitors (LICs) are of particular interest to this thesis. In 1984 Yata et al. synthesized a polyacenic semiconductor (PAS), which is a carbonaceous material. In 1987 PAS was proven to be able to store Li^+-ions through insertion.[31] Proving Li^+-ion insertion was the first step towards research on LICs, and 2001 witnessed the first LIC made from combining a battery electrode with an electrode from an EDLC.[31]

The first LIC had an activated carbon (AC) cathode and an $Li_4Ti_5O_{12}$ (LTO) anode and was developed by Amatucci et al.[31, 32] The electrolyte used had $LiPF_6$ as salt dissolved in ethylene carbonate (EC) and dimethyl carbonate (DMC).[32] Another way to write this is to display it as AC||LTO with 1 M $LiPF_6$ dissolved in EC:DMC (2:1). The cell produced in this paper was tested using an operational voltage window between 1.5–3.0 V; a current of 10 C was applied, resulting in 90% of the capacity being utilized for each cycle. It was reported that the cell had 85–90% capacity retention after 5000, which was far superior to LIBs.[31] Later, it was again reported that an improved version of this LIC could show up to 80% capacity retention after 9000 cycles while using 100% of the capacity available during cycling. It should be noted that the capacity of an LIC is lower than an LIB; therefore, the current for the LIC at 10 C is lower than 10 C for LIBs, as the C-rate is related to the capacity of the component.

1.3.8. The history of atomic layer deposition (ALD)

As seen earlier, applications have multiple names, and atomic layer deposition (ALD) is no exception. ALD was introduced around 2000; prior to this, it was known as "atomic layer epitaxy" (ALE).[33] Other names such as "molecular layer epitaxy" and "reaction sequence chemistry" have also been used.[33] The reasons why the term ALE was replaced with ALD is because some reactions defined as ALE were not indeed epitaxial to their surface; products from ALD synthesis are often amorphous, making the description inaccurate, which was solved by using a more general term like "deposition."[34]

It is somewhat difficult to reconstruct the history of when and where ALD started, as similar synthesis techniques have been developed at different times.[34] A German patent from the 1950s described vacuum evaporation of compounds but failed to specify the saturation of the monolayers, which the ALE patent filed by Suntola described well in the 1970s. In the USSR, the research groups of Stanislav Koltsov and Valentin Aleskovskii studied a synthesis technique, naming it "molecular layering" (ML).[34] Studies in which ML was synthesized with TiO_2 and GeO_2 were reported in the 1960s; but as the articles were available only in Russian, they were overlooked by the rest of the academic world.[35]

The early studies from the USSR focused mainly on high surface area substrates such as silica gel and 1-10 ALD cycles.[35] Aleskovskii and Suntola met in 1990 in connection with a review paper published by Suntola that mapped the early works of the ALE but which did not include Aleskovksii's ML work. They concluded that the ALE was invented separately from the ML, and even though the work of Aleskovskii included a deep understanding of the surface chemistry related to ALE/ML, samples or applications of the ML was not included in the presentation of Aleskovskii's work.

After several patent hearings, Suntola held the patent for the ALE (later ALD) technique from 1974 on; the patent was updated in 1979 to include compound precursors instead of only elemental reactans.[34] Suntola has later said that he believes the patent was accepted so easily in the USSR in 1978 because the examiners only saw the limitations of the ALE technique as it was too complex and slow for industry.[34]

The history of Suntola's ALE began in the 1970s.[34] Suntola's team was working with semi-conductors such as humidity sensors at Instrumentarium Oy. He needed a new way of producing thin film electroluminescence (EL) devices. Earlier attempts with evaporation and sputtering had not been fully successful because of the components that needed to be made with a "well-controlled crystal structure." He stated at that time that "To obtain a controlled material structure, 'deposition,' or material transfer, may not be sufficient—in principle, what is needed is to create conditions for the controlled build-up of the material layer."

The idea of the ALE was to create monoatomic layers sequentially on top of a surface, which should be possible if the introduced to the system would bind stronger with the atoms on the surface than with each other.[34] The first successful ALE experiment was in fact a semi-ALE experiment that could be categorized as a hybrid atomic layer epitaxy physical vapor deposition (ALE-PVD) experiment.[34] Suntola's goal was to make a zinc sulfide thin film on top of a substrate and, in order to do this, he used precursors of elemental zinc (Zn) and S (sulfur) that was heated to 360 °C and 100 °C under 2×10^{-2} and 3×10^{-3} torr pressure, respectively.[34] Reaction time was two cycles per second; Suntola expected to gain one monolayer per cycle and was surprised as it turned out to be closer to one third of a monolayer per cycle.[34]

Characterization of the film was achieved by X-ray diffraction (XRD) and the “look and feel” method of the thin film. After comparing it to the thin films made by other techniques, such as sputtering or evaporation, Suntola discovered that the ALE-PVD technique grew a mechanically stronger hexagonal structured thin film. Moreover, the ALE-PVD synthesis technique produced hydrophobic thin films of ZnS, while later ALE experiments produced hydrophilic samples.

Later, Suntola began to use zinc chloride ($ZnCl_2$) and hydrogen sulfide (H_2S) as molecular precursors.[35] The advantage of going away from solid elemental S to gaseous H_2S is that the gas flow is more constant over time as the flow of reactants will be affected by the surface area of the solid S.[35] This makes the synthesis function by a viscous flow instead of by high vacuum conditions.[35] Furthermore, the temperature needed to evaporate the reactants makes the process more complicated as it may not be the desired temperature for reacting in the chamber. The disadvantage of this specific process adjustment, however, is that H_2S is flammable, corrosive, and poisonous when concentrations are over around 350 ppm; moreover, it will spread much easier than solid sulfur as it is a gas at standard conditions.

Suntola demonstrated that controlled growth of thin films of ZnS could be achieved by sequential saturation of monolayers, first from elemental reactants and later from compound precursors. It is now considered to be one of the pioneers of the current ALD synthesis technique.[34] Most of the early components made from ALD were in the scale of micrometers, which required thousands of cycles. One of the early products made by ALD for the public was a screen at the Helsinki-Vantaa airport displaying the flights. This screen operated for over 15 years, starting in 1983, and was a ALD-synthesized electroluminescent Mn-doped ZnS with dielectric nanolaminate Al_2O_3–TiO_2, also made by ALD.[35] During the 1990s, Suntola demonstrated that ALD could be used for large quantities of high surface area materials by a magnitude of several kilo grams.[35]

1.4. Previous works

A thorough search of the relevant literature yielded no articles claiming to have explored the possibility of bypassing pre-lithiation for LICs by applying ALD coatings. However, coating of electrodes for batteries and capacitors produces results. The closest project found was presented by Cheah et al.[36] In Cheah et al., 3D Al_2O_3 electrodes coated with 17 nm of TiO_2 using $TiCl_4$ and H_20 as precursors were used in a half cell.[36] Furthermore, Wang et al. produced $Li_4Ti_5O_{12}$(LTO) that is incorporated in a graphene nanosheet matrix using ALD seeding of TiO_2 to be used in an LIC using ALD. The results from these articles have provided direction for the objectives of this project. The next section will focus on highlighting some characteristic advantages and drawbacks of applying coatings on high surface area materials, such as particles and porous materials. Since the capacitive contribution from the electrodes are proportional to the area of the electrodes, ALD on flat surfaces will not be considered in this section as they do not provide enough surface area.

1.4.1. ALD coating of high surface materials

ALD is used mainly for applications where conformal coverage and thickness control on atomic scale is important.[37] The mechanism behind the techniques is described in the theory section, where the technique is also discussed.

1.4.1.1. ALD-coated electrodes

Riyanto et al. reported that a 1 nm Al_2O_3 layer coating will increase the electrochemical performance of various anode materials. These coatings aim to be a stabilizing layer on top of other electrochemically active electrodes. The Al_2O_3 will reportedly reduce the unwanted reactions happening on the anode while acting as an SEI by forming Li-Al-O. This layer is reported to be a good ionic conductor as well as being electron isolating.

Furthermore, LCO cathodes that have thin Al_2O_3 and TiO_2 coatings will increase their capacity retention significantly. Al_2O_3 also reduced the side reactions between the electrolyte and the cathode, resulting in greater stability. The study concluded that Al_2O_3 had more potential as a coating material since it showed promising results for both cathodes and anodes.

1.4.2. Particles coated with ALD

ALD has been used for deposition on powders since the early 1990s.[37] Flow-type ALD reactors were used in the initial attempts. In 2000 a pump-type ALD reactor proved to produce uniform coating on powders as well. Particles in the micron range were successfully demonstrated by using a fluidized bed reactor (FBR). An FBR was later used by Hakim et al.[37] to produce a conformal coating on high surface area nanoparticles. The introduction of rotary reaction chambers that mechanically agitate the particles made stationary reactions relevant again for ALD coating on powders. The opportunity to use both thermal and plasma enhanced deposition also made this approach more attractive. The latest approach is the spatial ALD reactors, patented by van Ommen et al. in 2010. Since all these approaches have different drawbacks and benefits, it is ideal to combine components from each technique. King et al. added mechanical vibration, rotation, and gas pulsing to an FBR to prevent agglomeration and enhance fluidization of the nanoparticles.[37]

1.4.2.1. Using a pump-type ALD reactor with a grid setup

Ferguson et al.[37] reported in 2000 that a uniform coating of powders was possible using an ALD pump-reactor. In this paper the setup was a thin tungsten support grid with tantalum foil supporting resistive heating. Since it conducted *in situ* Fourier-transform infrared spectroscopy (FTIR) measurements, it needed to avoid FTIR interference with the reactions, applying some limitations on coatings.

Pump-type reactors have the advantage of not needing purging gas to flush. The technique has its limitations when it comes to the ability to up-scale. This limitation, as noted by Longrie et al., is due to the fact that "the very nature of the set-up renders upscaling to larger batches impractical."[37]

1.4.2.2. Using a pump-type ALD reactor with a crucible set-up for coating of particles

Bulk substrates supported by stationary crucibles have been shown to produce many successful coatings using the pump reactors. On the other hand, there are problems with scalability for use with coating particles. All particles are being subjected to different amounts of the precursor gases if the powder amount is too large. The amount of gas the particle is subjected to is decreasing when the volume of powders on top of it is increasing, which results in uncoated particles in the bulk of the powder.[37]

1.4.2.3. Fluidized bed reactor for atomic layer deposition of particles

Compared to other reactor types, using a fluidized bed reactor (FBR) for ALD will ensure a uniform particle mixing and temperature gradients during deposition. Having the option to run an uninterrupted process is highly beneficial for producing material over time. However, there are several challenges related to keeping the particles fluidized. By adding mechanical rotations and vibrations to the chamber, King et al. reported successful ALD-FBR reactions in 2007.[37] For operating under low pressure conditions, a rotary vane pump was also added to the system. Rotary vane pumps are good for low viscosity fluids; in this case, they made the system more efficient as the precursor was in contact with the particles for longer. Longrie et al. stated that either agitation or fluidization of particles is required if the ALD coatings are to be successful.[37]

1.4.2.4. Properties of mechanical agitation of particles during ALD coating

The system does not consume purging gas but requires some pumping power to operate. By supplying energy to the system by plasma instead of thermally heating the sample, the reactor can operate at lower temperatures than a thermal rotary ALD reactor can.[37] Other static reactors may suffer from uneven coating of particles when the powder amount is too large. This is because the particles on the surface will be exposed to more precursors than the powder in the center of the powder pile. This is in other reactors solved by numerous methods such as gas fluidization, but many of them have the drawback of using substantially more precursor or flow gas to obtain this effect.

In the rotary ALD reactor, it is possible to switch between static and pulsing mode by closing a valve, thus giving it a broader range of operation. By mechanically agitating the powder, it is possible to maintain a low consumption of gas, uniform coating of particles and making the agglomeration of particles less likely to occur. Furthermore, the system is easy to up-scale since it applies a constant particle flow to an open inner tube, making it possible to continuously collect coated particles.[37]

2. Theory

This section describes energy storage systems, focusing on their components, means of function, and properties. Capacitors, SCs, LIBs, and LICs have already been briefly introduced in this thesis in the section for historical background. The goals of the thesis relate to LICs, but understanding SCs and LIBs are essential to building an overall understanding of the system. The next section will describe ALD as it is crucial for understanding the synthesizing of the electrochemically active TiO_2 used in the LICs in this project.

2.1. Energy storage systems (ESSs)

Grid storage is mentioned in the introduction of this thesis as an example of multiple energy storage devices working together. It is common to combine capacitors, SCs, and LIBs to utilize the strengths of each component. Cameras use capacitors for the intense flash of light before each picture, and they use LIBs for powering its screens and other functions. Electric vehicles use capacitors and SCs to increase the acceleration and to harvest kinetic energy from braking of the car. LIBs are used for re-charging the capacitors and powering all other functions of the car.

2.1.1. Components of energy storage systems (ESSs)

The energy storage systems (ESS) discussed in this thesis all have two electrodes separated by some medium. Capacitors have conductive plates with a dielectric between them. LIBs, SCs, and LICs all have electrodes separated by an electrolyte-soaked separator. Separators are what physically separates the electrodes, thus avoiding an internal shortage. The job of the separators is therefore to work with the electrolyte to have an electronic insulating and ionic conductive pathway between the electrodes.

2.1.2. Properties of the energy storage systems (ESSs)

As mentioned previously, several properties can be used as a basis when comparing different energy storage systems. The three most important properties are capacity, energy, and power The performance of energy stored in the device and how quickly it can convert it is often quantified by specific energy and specific power. Capacity describes how many Li-ions can be stored in the device which, multiplied with the voltage, this will give the amount of energy stored in the system. Power describes the rate at which it is converted or transferred.

2.1.2.1. Energy

Energy may be defined as "the capacity for doing work." Energy in LIBs is mainly stored as chemical energy and transformed directly to electrical energy. The unit of energy is joule, which can be expressed in SI-base units as $J = \frac{kg\ m^2}{s^2}$.

2.1.2.2. Capacity

In general usage, "capacity" is defined by the Cambridge Dictionary as "The total amount that can be contained or produced." This is not far from the definition used in electrochemistry, which can be described as the quantity of electricity involved in the electrochemical reaction of the battery. In other words, capacity is the number of electrons one can store in the battery, where a high capacity indicates that a considerable amount of energy may be stored in the system.

Capacity is expressed in the units of ampere hours, *Ah*; but often specific capacity, also called gravimetric capacity or volumetric capacity, will be more descriptive of the application in mind. Specific capacity is expressed in the units of ampere hours per weight unit, i.e., *Ah/g*. Volumetric capacity is expressed in the units of ampere hours per volume unit, namely Ah/cm^3 or Ah/L. Areal capacity is commonly used for some applications, such as when thin film electrodes are involved. Areal capacity is expressed in the units of Ah/cm^2.

2.1.2.3. Power

Power is the amount of energy being transferred per unit of time and is termed *Watt*. By using the units base SI-units, *Watt* can be expressed as $W = \frac{J}{s} = \frac{kg\ m^2}{\boldsymbol{s^3}}$. Just as with capacity, it is common to use specific power or volumetric power with the units of $\frac{W}{g}\ and\ \frac{W}{cm^3}$, respectively. The relationship between how much energy and power a system can deliver is portrayed in the Ragone plot in .[38] This is used to describe that even though there is more specific energy stored in a battery system than in a supercapacitor energy system, the amount of specific energy the system can deliver per time unit is larger for the super capacitors than for the battery systems. The solution to this "gap" is to turn the Li-ion capacitor (LIC) into an energy storage system that can hold more energy than a supercapacitor and deliver it more quickly than a battery.

The Ragone plot does not fully describe the device. The lifetime of the device is described in cycle life, which indicates how many cycles with charge/discharge it can undergo before losing too much of its ability to store energy. It is important to note that this does not tell the whole story, as LIBs normally have much more energy per cycle than supercapacitors. Therefore, an SC needs to run through multiple cycles to transfer the same amount of energy as one battery cycle.

2.2. Li-ion batteries (LIBs)

This section will discuss LIBs as this is relevant for understanding and comparing the LICs. Beginning with an introduction to the general principle behind an LIB, the section will then explore the theory of anodes and the various storage mechanisms. Finally, a short explanation of SEI and electrolytes will be provided as well as a discussion of why they are so essential to understanding anodes.

2.2.1. How LIBs work

LIBs store and release energy by reversible redox reactions occurring between the electrodes and the electrolyte. The diffusion of Li-ions between the electrodes was initially described as the "rocking chair" function by Whittingham.[20] This is the mechanism that differentiates a Li-battery from a Li-ion battery (LIB). Both electrodes in the LIB act as hosts for the Li-ions. During discharge the negative electrode served as a "Li source" and the positive electrode served as a "Li sink," while the roles of "sink" and "source" were switched during charging.[20] The Li-ions were "rocking" back and forth during cycling (which refers to charge/discharge)—like a rocking chair. The impact of the rocking chair principle is not only that the Li metal anode could be avoided. It was also necessary for the cathode of the batteries to contain Li in its structure to function as the Li source. A schematic figure of the LIB is shown in Figure 4.

2.2.2. The electrodes of the LIBs

The electrodes of LIBs and SCs must meet similar criteria such as mechanical and chemical stability, low volume expansion, no irreversible processes, high Li diffusivity, and high specific capacity. Ideally, they should also be made from abundant, safe, non-toxic, and ethically gained materials. Furthermore, as a component, all pieces should be compatible with the electrolyte, have a good connection to the percolating network, and have low production complexity and cost.[39]

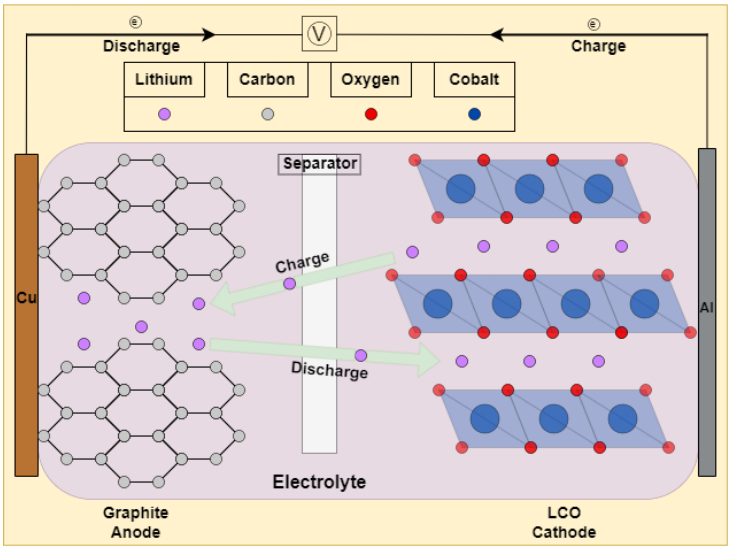

Figure 4: Schematic picture of an LCO|Graphite LIB, showing the components and how it works during charge and discharge. Reproduced from [2].

In addition to these general qualifications, the anode needs to have a voltage versus Li-metal that is close to, but not under, zero. This will help achieve the largest possible voltage difference between the cathode and anode. Likewise, the cathode needs to have a high potential difference versus Li/Li^+ for the same reason.

2.2.3. Anodes

As the focus of this project is on anodes, this section will describe some of the most important anode materials and their ways of storing lithium.

2.2.3.1. Li-metal anode and dendrites

As mentioned previously, the inventor of the Li-metal anode was awarded the Nobel Prize in chemistry for taking the first step towards LIBs. In theory, the Li-metal would be the perfect anode with low potential versus the standard hydrogen electrode (SHE), high capacity, and a virtually "unlimited" source of Li.[40] To understand why Li-metal anodes is not used today, dendrites need to be briefly explained. The word "dendrites" comes from Greek word for tree, and they are moss or needle-shaped Li growing on the surface of the Li-metal anodes or when rapid charging is used.[20] In addition to consuming Li and being an energy-consuming parasitic reaction, these dendrites will grow to puncture the separator before eventually short circuiting the entire battery. It became clear that the Li-metal anode was not yet ready for use in batteries; however, recent work continues to explore the possibilities of using Li-metal as anodes in the future.[20]

2.2.3.2. Graphite anodes

Graphite is the dominating anode material in most commercial applications today and is therefore the reference point for further research. Graphite has a specific capacity of 372 mAh/g, high capacity retention, and is relatively inexpensive to produce.[41] Graphite is an intercalation material, which is a subgroup of insertion materials. This means that Li is stored between the graphite layers (graphene), which is made of carbon rings (see Figure 3). The reaction describing lithiation and delithiation of graphite is as follows:

$$LiC_6 \leftrightarrows C_6 + Li^+ + e^-$$

The difference between insertion and intercalation is that intercalation requires that there be a layered host (graphite) that takes up guests (Li) within its interlayer gaps. Insertion materials will be discussed later in the section on anodes, 2.2.3.5.

2.2.3.3. $Li_4Ti_5O_{12}$ (LTO) anodes

The $Li_4Ti_5O_{12}$ (LTO) was introduced as an alternative to the graphite anode in 1990s.[23] Two disadvantages of the LTO is that it is a poor electronic conductor compared to graphite and has only around half of the theoretical specific capacity (175 mAh/g for crystalline spinel[42]) of graphite (372 mAh/g[26]). LTO also has a higher voltage (1.5 vs Li^+/Li), which limits the maximum voltage of the full cell. The total operating cell voltage is calculated from subtracting the voltage of the anode (vs Li^+/Li) from the voltage of the cathode (vs Li^+/Li). A significant advantage of LTO is that it is highly stable and can be used in applications where high capacity retention and energy density are more important than high capacity. Graphite anodes are stable compared to silicon anodes, but even graphite cannot match the capacity retention of LTO anodes. LTO is also reported to have excellent reversible specific capacity in Na-ion batteries, with reports of 155 mAh/g.

2.2.3.4. Amorphous and anatase TiO_2 anodes

TiO_2 anodes are closely related to the LTO anodes. They both fall under the category of insertion materials, as the Li "guests" are "hosted" in the lattice of the anode material. This is similar to the intercalation that we see in graphite, with the key difference that the host does not need to be a layered structure.[43] The theoretical capacity of TiO_2 anodes is 336 mAh/g and is generally described by the following equation:

$$Li_xTiO_2 \leftrightarrows TiO_2 + x\ Li^+ + x\ e^-$$

However, bulk anatase TiO_2 and amorphous TiO_2 suffer from low electronic and ionic conductivity and will be limited to 235 mAh/g at currents equal to 1 C. There are numerous ways of battling this, but thin films are showing promising results. Moitzheim et al. reported that thin films of an anatase and amorphous TiO_2 in the range of 5–10 nm could achieve specific capacity of 116 mAh/g at currents of 500 C.[44] The TiO_2 thin film was coated on Si-wafers using ALD.

2.2.3.5. Silicon anodes

Silicon anodes are among the few that can compete with the Li-metal anodes when it comes to low potential and high specific capacity. The theoretical capacity of Si is approximately 10 times that of graphite, and Si is one of the most abundant elements. Reactions (2) and (3) will give a specific capacity of 3580 and 4200 mAh/g, respectively.[41,45] Si is in the class of alloying materials that break the Si-Si bonds to form Si-Li bonds. Describing the lithiation/delithiation process of Si anodes is not a straightforward process, as Si and Li can form many alloys such as the following:

$$Li_{15}Si_4 \leftrightarrows 4\ Si + 15\ Li^+ + 15\ e^-, \qquad (2)$$

$$Li_{22}Si_5 \leftrightarrows 5\ Si + 22\ Li^+ + 22\ e^-, \qquad (3)$$

The lithiation of Si leads to a massive volume expansion of 300%, which places considerable stress on the structure.[45] Si will therefore always be amorphous during electrochemical cycling, regardless of whether it is crystalline or amorphous in its initial form. This is because the Si atoms do not "remember" which Si atom they used to be bonded to before finding an Li atom, making it difficult to acquire the same structure as they previously had. This becomes increasingly difficult during the formation of solid electrolyte interphase (SEI). Taken together, these factors limit the capacity retention of the cell.

2.2.4. Solid electrolyte interphase (SEI)

The SEI layer brings benefits and drawbacks to batteries. SEI formation is essential to make most batteries perform well, but it is also the main reason why an electrochemical cell stops functioning. It helps stabilize the electrodes in a larger voltage window and helps with electrochemical isolation, preventing co-intercalation. However, it also consumes electrolyte and grows where it can. In particular, Si starts growing on the already expanded Si, making it impossible to return it to its initial state. Choosing the correct electrolyte and additives are essential for stabilizing the SEI, which will be explained in the next section. Figure 5 shows a TEM image of an SEI in picture A, while picture B shows a schematic illustration of what an SEI can be chemically composed of.[2]

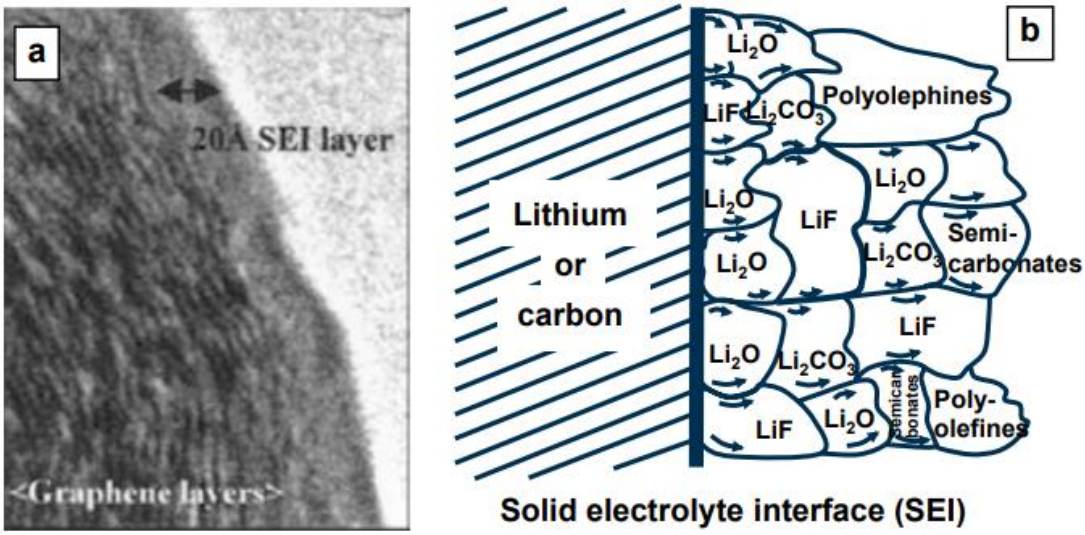

Figure 5: TEM picture and schematic illustration on a SEI layer. Reproduced from with permission from [2].

2.2.5. Electrolytes

Diffusion of the Li-ions between the electrodes is made possible by the electrolyte.[46] The electrolyte's main purpose is to be electronic isolating and ionic conductive. Electrolytes also need help creating a chemically stable SEI layer on the electrode. An electrolyte may be liquid or solid; over the last decade, however, room temperature liquids have been the dominant LIBs.[46] The standard liquid electrolyte used in LIBs will typically be Li-salts, such as $LiPF_6$, dissolved in organic solvents.[46] $LiPF_6$ suffers from low thermal stability and may release HF gas; however, it benefits from low electronic conductivity. $LiPF_6$ also passivates for aluminum metal current collectors and is compatible with the alkycarbonates, which is important in the process of SEI formation.[46]

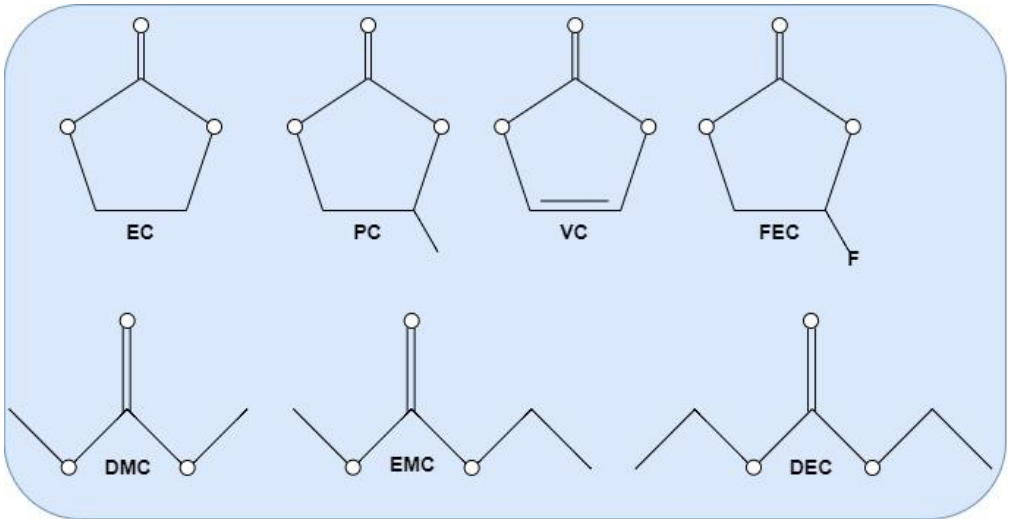

Figure 6: Organic solvents and additives commonly used in electrolytes together with $LiPF_6$ for LIBs and LIC. Reproduced from Nowak et al. [4] and Michan et al.[9]

Some of the most common organic solvents used in electrolytes are DEC (diethyl-carbonate), DMC (dimethyl-carbonate), EC (ethylene-carbonate), PC (propylene-carbonate), VC (vinylene carbonate), and FEC (fluoroethylene carbonate). These options are shown Figure 6. All these carbonates have different advantages and disadvantages and are frequently used together to optimize the properties of the electrolyte. DEC and DMC are linear carbonates, while EC, FEC, VC, and PC are cyclic carbonates. One common electrolyte commercialized for research purposes is the LP30. The LP30 is a mixture of 1.0 M $LiPF_6$ and 1:1 EC/DMC as solvent.

2.2.5.1. Additives

FEC and VC is sometimes added in amounts ranging from 5–10% and 2% as additives in the electrolyte as this combination is beneficial for establishing a stable SEI layer on the anode. During lithiation, various undesirable processes such as “cracking,” electrode delamination, or SEI instability will reduce the capacity retention of the anode.[47] Alloy materials generally have more problems with losing capacity retention and are therefore more dependent on additives than other electrode materials.

2.3. Capacitors

Capacitors are a common denominator for devices that rely on the storage of electricity in an electric field.[48] The current project will focus on SCs, which is a subgroup of capacitors. It is therefore important to understand the basics of a capacitor before going into the special case of SCs. Capacitors are commonly displayed by the parallel plate capacitor, having two identical conductive plates with a dielectric in between, which gives the conductive plates a separation distance. The amount of charged electricity is measured in capacitance, with units of farad or coulomb per volt;[48] the amount is given by the formula $C = \frac{Q}{V}$ or $C = \frac{dQ}{dV}$, depending on how relevant the charge build-up is for the component.[48] (Figure 3Figure 3: Figure describing the different means of storage for capacitors, batteries, and pseudocapacitive mechanisms. The first line of figures shows CV plots of the various components. The last line of figures shows an atomic representation of one of the different systems listed in the section above, where typical systems are listed. The kinetics are also described by relating the voltage to the current of the CV plots. Reproduced from Lukatskava et al. with permission under the CC BY 4.0 license.[8] illustrates the different ways of storing energy in capacitors.)

2.4. Supercapacitors (SCs)

Supercapacitors (SCs), ultracapacitors (UCs), or electrochemical capacitors are all the same thing with different names. The supercapacitors are a subcategory of capacitors. The idea behind capacitors and supercapacitors differs from LIBs as they rely on non-faradaic (capacitive) processes in contrast to batteries, which rely on faradaic electron transfers.

2.4.1. Electric double layer capacitor (EDLC)

Electric double-layer capacitors (EDLC) store energy using the principles of electrostatics.[29] This is one of the most common commercially available supercapacitors on the market. The energy storage is done in the double layer at the interface between a conduction material and an electrolyte; the non-faradaic processes are taking place in the electric double layer (EDL).[49] Non-faradaic electron transfer occurs when the charged particles do not cross the interface, and the electricity is carried by charging/discharging of the EDL. The EDL can resemble a capacitor connected in a electrical series with an ohmic resistance.[49]

An example of an EDLC is a symmetric supercapacitor with two identical electrodes made of activated carbon on current collectors, an electrolyte containing the ions for the reaction, and a separator to keep the electrodes apart to avoid short circuiting the cell.[50] Activated carbon is a common choice for supercapacitors as it conducts electricity and has enormous specific surface area that is measured at several thousand m^2/g using BET measurements.[51] The material is abundant as it is made from carbon; moreover, it is inexpensive to make, non-toxic, and well known for industry. In contrast to the peaks observed in the CV plot for faradaic processes, the non-faradaic processes will be displayed as close to a square in the CV plot, which means that the current, and hence the capacity, is independent of the voltage.[29]

Due to the properties of EDLCs, the applications for the EDLCs are where high-power density and long cyclability are important. EDLCs can report having power densities in the area of 15 $kW\ kg^{-1}$, compared to batteries, which are typically some $kW\ kg^{-1}$.[52] In general, the greatest drawback of the supercapacitors compared to a Li-ion battery is the low gravimetric energy density, which lies in the area of 250 Wh kg^{-1} and 5 Wh kg^{-1} for LIBs and supercapacitors, respectively.[7] In other words, LIBs are used to store large amounts of portable energy, while supercapacitors are used to store smaller amounts of energy ready to be used in a matter of seconds.

2.4.2. Pseudocapacitors

Pseudocapacitors differ from other capacitors in that they can store energy both by a non-faradaic charge storage in the electric double layer, as seen in EDLC, as well as by the faradaic electron transfer, as seen in batteries.[29] Examples of materials being used in pseudocapacitors are RuO_2 and MnO_2. The faradaic electron transfer taking place in these materials utilizes the many oxidation stages of, for example, Mn.[29] The metal centers of the material contribute to the electron transfer. It is important to note that it is only the oxides close to the surface that contribute the pseudocapacity, and the pseudocapacitor reactions are also therefore sometimes referred to as surface redox reactions.[29]

Faradaic electron transfer is electrons crossing the interface by a chemical reaction, as is true for reduction or oxidation of Li back into the form of metal or ion.[49] The result of this transition will give peaks in a cyclic voltammetry (CV) plot while having faradaic processes. Faradaic processes will go to constant values for composition and voltage.[49] These processes are shown in Figure 3. Non-faradaic processes will be displayed as squares, while faradaic processes will have large peaks of oxidation and reduction (see Figure 3.)

2.4.3. Hybrid supercapacitors

Hybrid supercapacitors, or asymmetric supercapacitors, are described as the bridge between a battery and a supercapacitor.[7] The abbreviation for this type is HASCs, as it is a hybrid asymmetric supercapacitor. One of the electrodes is of the same type as those used in batteries, while the other is like those used in supercapacitors.[30] The theory behind this is that HASCs can utilize both the high faradaic electron transfer coming from redox reactions in LIBs with the fast non-faradaic electron transfer one can find in capacitors and supercapacitors. It should also be noted that since the battery materials are often somewhat conductive and have a specific surface area, they will also contribute with a small non-faradaic portion. The supercapacitors also have a faradaic electron transfer contribution; however, this is only true for the oxides close to the surface of the pseudocapacitors and not for the EDLCs, as mentioned previously. LIBs often struggle with slow kinetics as alloying and insertion are slow diffusion limited reactions.[30]

The positive ions that carry charge in the hybrid supercapacitors are the same as in batteries, such as Li^{+1}, Na^{+1}, K^{+1}, Ca^{+2}, and so forth.[7] This means that the electrolytes being used in these applications should contain one of these as the cation in the salts. When it comes to the choice of electrodes, Lai et al. stated that “using a porous EDL material as the positive electrode coupled with a Li-ion intercalation/alloying material as the negative electrode” is what is required to achieve the “high power and acceptable energy densities” for the hybrid supercapactiors.[7]

2.4.4. Li-ion capacitor (LIC)

Li-ion capacitors (LICs) are also referred to in the literature as “hybrid capacitors,” “hybrid asymmetric Li-ion capacitors,” “hybrid Li-ion capacitors,” “supercabattery,” and “supercapattery.” This component is a subsection of hybrid supercapacitors. An HASC is classified as an LIC when charged Li-ions and electrons are transferred across the electrode. This makes LICs fall under the category of components relying on faradaic processes.[49]

Given its “porous EDL material,” the LICs provide many opportunities, but in this thesis the focus will be on activated carbon (AC) as cathodes. The cathode is coupled with a standard LIB-anode such as silicon or LTO. An example of an LIC is displayed in Figure 2

2.5. Atomic layer deposition (ALD)

Atomic layer deposition (ALD) is a synthesis technique based on sequential monolayer deposition. It introduces the reactants sequentially, building layer by layer. The idea behind ALD is to saturate the surface for each introduction of reactants, as mentioned in Section 1.3.8.[34] ALD is a subgroup of CVD (chemical vapor deposition) but differs in that the ALD approach introduces the precursors sequentially. This makes it possible to use more highly reactive precursors. CVD needs to consider if the precursors could react in gas-phase, putting limitations on the selection of precursors. The advantage of CVD compared to ALD is that CVD may produce in minutes what the ALD produces in days.

ALD is well known for its abilities to form films of Al_2O_3 and TiO_2; the latter is a focus in this thesis. This is a binary process, consisting of four steps that together are called an ALD cycle. The cycle is repeated until the desired film thickness is acquired. (This is not to be confused with a charge/discharge cycle from electrochemistry.) Before starting the ALD cycling, it is customary to have a waiting period (~1 hour) during which vacuum (~1 torr) is maintained and temperature is stabilized.

The first step in the cycle is to pulse precursor 1. The second step is to purge the chamber by flushing out precursor 1 with the flow gas. The third step is to introduce precursor 2. The fourth step is to purge again with the flow gas. There are many ways of introducing the precursor gases into the system, some of which are discussed in the previous section. One of these methods is the pressure-type ALD reactor, which introduces the precursors by spraying them into the substrate by pressure cycling. The principle behind this is to push the precursors—and therefore also the coatings— deep inside the substrate to fill pores or reach all powder particles in a batch.

For a binary reaction such as TiO_2 from H_2O and $TiCl_4$, $TiCl_4$ is the source of the cation. $TiCl_4$ has Ti as the metal center, surrounded by Cl-ligands. H_2O is the source of the anion to the finished product and is frequently used for oxides. H_2O is one of the easiest, least expensive, and safest ways to introduce oxygen to the process, but gaseous ozone is also known to be used. The flow/carrier gas needs to be inert as it is used to prevent further reactions. Flow gasses are normally N_2 or Ar_2.

It is easy to think, as Suntola initially did, that the ALD synthesis establishes a completely linear relationship between the number of cycles and the growth of the film, as one cycle gives one monolayer of film.[34] This is a qualified truth at best. A common way to estimate how many cycles are needed for a given film thickness is to use similar experiments and calculate the growth per cycle (GPC). By assuming this to be linear, one can simply divide the film thickness by the number of cycles, resulting in a value that gives the growth per cycle.[53] The growth of the film is slower in the beginning of the process because of . Nilsen et al. suggests a that formation of islands occur on the surface of the substrate. The formation of islands may be connected to it being easier to grow a film on previous film, rather than to grow on the substrate itself. As time passes by, the islands start to grow at meet while making the surface more covered with the deposited film. This makes the GPC of the experiment deviate from the linear relationship suggested in Nilsen et al. when the film is thin,[53]. This will be further discussed in section 5.1.

2.5.1. Precursors

Choosing the right precursors are necessary to determining the reactivity, reaction mechanics, biproducts, and possible contamination. Generally, higher growth rates are obtained by smaller ligands. As an exception to the rule, Aarvik et al. noted that $Ti(OCH_2CH_3)_4$ and $Ti(OCH(CH_3)_2)_4$ have higher growth rates than $TiCl_4$. The reactions were conducted in the temperature range from 100–400 ^oC, with H_20 or H_2O_2 as the oxygen precursor. This will be discussed further in Chapter 5.

2.5.2. Gas fluidization of particles

The idea behind using the fluidized bed reactor (FBR) for ALD coating of powders is to make the powder behave like a fluid by pressing a gas (or liquid) through it. This is referred to as fluidizing the powder, and it is a good technique to ensure that all the particles have equal access to precursor gasses. The principle is to have the force acting from the gas on the particles to be equal to the force that pulls the particles to the ground.[37]

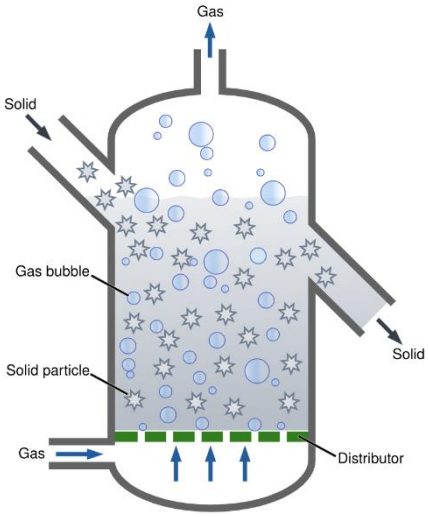

Figure 7: Schematic picture of a fluidized bed reactor for ALD depositions. Acquired from WikiCommons artist YassineMrabet. The work is part of the public domain and is free to use by all for all purposes.[6]

Figure 7 shows a reaction chamber in which the solid enters the upper left and exits the right side of the reactor, ensuring continuous operation. A gas flow enters the bottom of the chamber, passing through the distributor. The gas continues flowing through the particles before going out the top of the reactor.[37]

2.5.3. Mechanical agitation of nanoparticles for atomic layer deposition

Regarding ALD reactors, the agitation of particles may be introduced by rotating the chamber, mechanically stirring the sample, or vibrating the particles. It is a pump-type reactor, so purge gases are not used. There are two ways of supplying energy to drive the reactions: the rotary PE-ALD reactor supplies energy by plasma, while the thermal reactor supplies energy by thermal heating of the precursors.

Rotary reactors have a spinning reaction chamber that agitates the particles during cycling. Particles are pushed towards the walls of the reaction chamber because of the centrifugal force.[37] The reactors can switch between working with high vacuum static reactions or large batches of mechanically agitated nanoparticles. To go from static mode to pulsing mode, a valve needs to be closed at the pulsing system and the rotary reactor.

2.5.4. Spatial ALD reactor

The spatial ALD reactor relies on separating the areas where the half reactions of the synthesis occur. This is achieved by having the precursor gases fixed to different areas in the system and then making the fluidized particles move through the system. For a reaction of two precursors α and β, the particles will be carried by an inert carrier gas from zones A to B. Only inert carrier gas and particles may be in the area between zones A and B and will purge the particles in this area. Carrier gas pushes away the excess gases because it will move faster than the particles. This is an efficient self-purging process, but it only works for particles that are larger than several micrometers. When dealing with smaller particles, “purge ports” may be used.

2.6. Characterization

2.6.1. Spectroscopic ellipsometry

The ellipsometry instrument is an optical device found in facilities where thin films are being studied because it can determine coating thickness and index of refraction. It provides an accurate, non-destructive method for evaluating the thickness (*d*) and optical properties of the sample. The absorption coefficient (α), refraction index (*n*), and extinction coefficient (*k*) are among the optical properties being studied.[54]

The refractive index (n) is a quantification of the ability of a medium to bend a beam of light, often described through Snell's law. The refractive index is a dimensionless number related to the velocity at which light travels through a medium.[54]

$$n_i \sin(\Theta_i) = n_r \sin(\theta_r)$$

The left side of the equation describes the angle, Θ_i, between the medium and the incoming light beam before being refracted, while n_i is the refractive index of the medium the light beam travels in before being refracted. The right side describes the angle the light beam will have after being refracted, Θ_r, by entering medium 2 with a refractive index n_r. This is known as Snell's law.[54]

An ellipsometer measures the change in the polarization of the light by sending a polarized monocratic light on a reflective surface. The optical properties are described as a function of the wavelength of the light. By using Cauchy's transmission equation, one can relate the refractive index to the wavelength of the light connected to a transparent sample.[54] The complete Cauchy's equation is given by the wavelength (λ), the refractive index (*n*), and a set of optical constants (*A,B,C…*):

$$n(\lambda) = A + \frac{B}{\lambda^2} + \frac{C}{\lambda^4} + \cdots$$

In most cases, this is simplified to an expression containing only the two or three first terms:

$$n(\lambda) = A + \frac{B}{\lambda^2} + \frac{C}{\lambda^4}$$

Most samples have material-specific regions of wavelength where the light is not absorbed; these transparent wavelengths can be fitted with Cauchy's transmission equation. Light with wavelengths that are absorbed need to adjust its real and imaginary optical values. Advances in computers and mathematical models have improved the accuracy and efficiency of the instrument, as the calculations are computationally demanding.

2.6.2. Scanning electron microscopy (SEM)

Scanning electron microscopy (SEM) differentiates from the standard optical microscopes in that it “sees” by handling the feedback from electrons instead of light. This is achieved by sending a thin electron beam through a system of condenser lenses and lens apertures onto a thin sample. This technique is used mainly for morphological assessments of the samples as the electrons cannot go too far into the material with the expectation to return. Figure 8 presents a schematic illustration of the areas where the signal comes from.

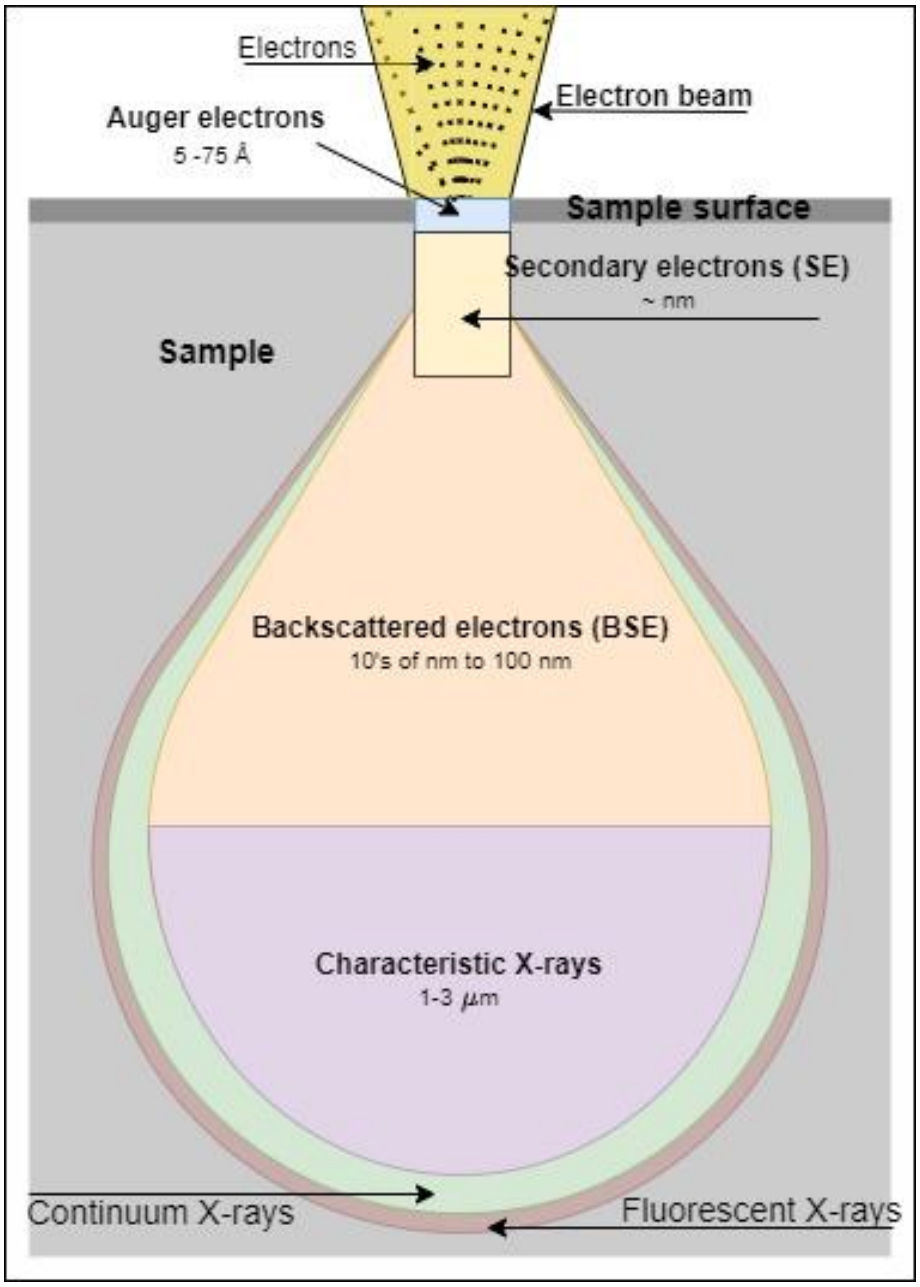

Figure 8: Schematic figure of the signals gained from a SEM measurement. Reproduced from [1].

Pictures of the surface come from secondary electrons (SEs) and backscatter electrons (BSEs). SEs result from inelastic collisions between the primary electrons (PEs) from the electron beam and the atoms, and they provide highly detailed information about elevations on the surface. The mechanism behind the various signals obtained from the SEM measurements are shown in Figure 9.

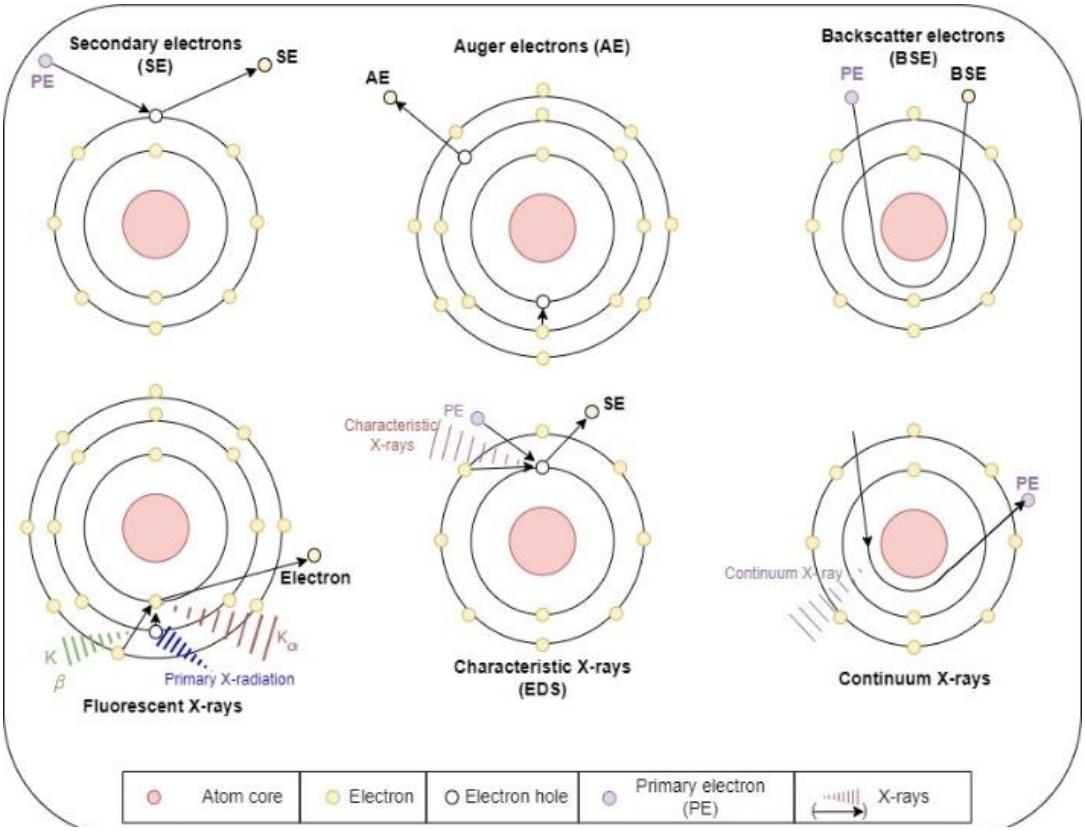

Figure 9: Schematic figure showing how the different signals gained by a SEM instrument. Reproduced by,[1].

BSEs result from elastic collisions in the sample and display heavier atoms that are brighter than atoms of lower mass. This is because the PEs are bent more by heavier atomic cores, which means that more electrons can return with higher intensity.

Auger electrons (AEs) have discrete element-specific energy values that can be used to map the elements in the selected region. AE spectroscopy is when the sample is bombarded with a narrow high-energy electron beam. Characteristic X-rays occur when a PE transfers some if its energy to the atoms of the sample.

This will result in the one of the electrons either “jumping” one step to a higher energy shell or leaving the sample. Either way, this results in a positive hole in the electron shell that it left. This will be filled by an electron from a higher energy shell “jumping” one step down to a lower energy shell. Characteristic X-rays of this atom are then released due to the energy difference in this transition. These X-rays are used in EDX analysis of samples, describing both the types of elements and the ratio among the elements in the given area of the sample. The mechanisms and areas of origin of fluorescent X-rays and continuum X-rays are also schematically shown in Figure 8 and Figure 9, but will not be further discussed as they lie beyond the scope of this thesis.

2.6.3. Galvanostatic cycling (GC)

Galvanostatic cycling is defined as cycling with a given current while measuring the change in voltage.[55] This method is the most common way to measure the capacity of the cells as one can measure how long it is possible to apply a given current to a cell before reaching the cut-off voltage of the measurement.[55] Cut-off voltage is a term used for the upper and lower limit of the potential window while cycling. The capacity is the amount of electrical charge inserted or drawn out of the cell before reaching the cut-off voltage and is measured in *mAh*. It is often more relevant to refer to specific capacity, which is defined as capacity per active material. It is common to differentiate the charge capacity from the discharge capacity with the distinction of putting in or taking out electrical charge into the cell, respectively.[55]

2.6.4. Cyclic voltammetry (CV)

Cyclic voltammetry (CV) is performed by applying a constant change in voltage per time unit through the voltage window of operations while measuring the voltage and current. CV is classified as one of the linear sweep techniques.[56] CV is useful for studying the reduction and oxidation processes occurring in the LIB, LIC, or SC by observing the electron transfer.[56] By inspecting the curves, valuable information on the processes can be gathered. The positioning of the peaks gives the voltage of the oxidation and reduction process and determines, for example, the voltage region for charging and discharging.

Studying the shape of the CV curves makes it possible to gather considerable information, as seen in Figure 3.

2.6.5. Shallow cycling

Shallow cycling for LICs and LIBs is a term used to describe when only a portion of the stored Li is being utilized. Depth of discharge (DoD) is a term used to describe how much of the available charge is being drawn out. Shallow cycling will be represented by a low percentage number of DoD. To obtain shallow cycling, high current rates will be applied to ensure that the Li-diffusion does not reach deep inside the bulk of the electrode. A large amount of Li will go into forming a SEI as well as going into the bulk of the Si in these initial cycles. Since all the Li needs to come from somewhere, this would lead to drying up the electrode's supply of Li. The slow kinetics of the multi-step Si alloying process going from de-lithiated to lithiated Si can generally be described by equation (1),[2]:

$$Li_xSi_y \leftrightarrows y\,Si + x\,Li^+ + x\,e^-, \qquad (1)$$

By shallow cycling of a Si@TiO_2 electrode, the aim is to avoid filling the Si-bulk with what "full-depth" cycling will produce, and instead to fill the volume of the thin film TiO_2. The electrolyte will hopefully give enough Li to the system to drive the faradaic charge transfer while not drying up the electrolyte. Drying up the electrolyte means taking all the Li out, greatly reducing the ionic conductivity of the electrolyte. The Li diffusion length seems to be around 8 nm, making atomic layer deposition (ALD) an ideal synthesis technique for this purpose. ALD provides excellent thickness control for coating in the nm range and is non-destructive towards the Si samples.[57]

3. Experimental

This chapter presents a traceable overview of the methods, instruments, and software used to produce the results represented in this thesis. Fabrication of electrodes, thin film depositions, and coin cell assembly and characterization will also be discussed in this chapter.

3.1. Choice of materials

The Si used in this project is nanosized amorphous Si (a-Si). The silicon used in this project is amorphous spherical Si-nanoparticles (a-Si NPs) from IFE, which is made in a free-space reactor by the silane pyrolysis synthesis method. A silicon-phosphor SiP_x alloy will also be investigated in half cells. The SiP_x is made by IFE in a similar process as all the other Si, but phosphine has been added to the synthesis.

All TiO_2 electrodes are Si electrodes coated with a thin film of TiO_2 (Si@TiO_2). By avoiding the voltage values for oxidation/reduction of Si and graphite, Si and graphite will be assumed to make a negligible capacity contribution to the system. This assumption will be verified by testing Si and graphite electrodes (without the TiO_2 film) in the same voltage window and measuring the capacity contribution.

An Si anode was chosen as a reference to TiO_2 because it is known to work together with AC as electrodes for LICs.[7] This LIC device does, however, require pre-lithiation. The AC|Si LIC device will serve as a reference system to the AC|TiO_2 LIC device.

3.2. Fabrication of electrodes

3.2.1. Anode slurry

The procedure for anode is based on Lai et al.[38] The slurry is produced in a 60:15:15:10 ratio for Si:CMC:SuperP:Graphite. The standard size of the slurry is 300 mg; it consists of 240 mg silicon, 60 mg sodium carboxymethyl cellulose (Na-CMC), 15% carbon black (C65, Super P), and 10 % graphite (T804).

Compound	Description	Formula	Supplier	Role
Silicon	Si-nanoparticles	Si	IFE	Active material
Silicon phosphorous	SiP_x-nanoparticles	SiP_x		Active material
Graphite	T804	C	TIMCAL	
Carbon black	Super P – Super C65	C	TIMCAL	Conductive additive
Carboxymethyl cellulose (CMC)		$C_8H_{15}NaO_8$		
Citric acid		$C_6H_8O_7$		
Potassium hydroxide		KOH		

The binder, CMC, is first dissolved in a mix of 1.0 mL type II water and 0.6 mL buffer solution with an ideal theoretical pH of 2.87. The pH is measured using pH strips and is therefore somewhat uncertain. The buffer solution aims to be close to pH 3. The buffer is made from 150 mL type II water, adding 0.6 g of KOH and 1.1 g of citric acid. After mixing by a magnet stirrer for at least one hour, the buffer solution is ready to use. Since the buffer contains OH^-, the buffer will start to precipitate over time. The precipitation of the particles in the buffer will change the pH of the buffer, making it lose its pH-balancing abilities. Since it is crucial to have the correct pH to ensure homogenous mixing of CMC and silicon, the buffer solution is remade every four weeks.

It is important that the powder is carefully distributed on top of the liquid, so that the CMC powder is in contact with the liquid and not itself. This is done to avoid bits of solid material in the CMC gel. The solution is mixed in an ARE-250CE centrifuge by Thinky Co., which will be referred to as the ‘‘Thinky-mixer.’’ The mixing procedure is five minutes at 2000 rpm + two minutes of defoaming at 700 rpm before checking the gel. The gel should be smooth, uniform, and clear. If the CMC gel contains any bits of solid material, a spatula is used to chop up the solid material to make it a homogeneous liquid. The gel is then centrifuged at 2000 rpm for three minutes + one minute of defoaming at 700 rpm. After this, the solution will be a clear transparent gel; silicon, graphite, and carbon black are added next to the gel with 0.6 mL water. The same mixing procedure that was used for the CMC is repeated after adding all the components to the mixture.

The slurry is coated on top of an 18 µm thick dendritic copper foil using a Hohen handheld slurry-coating blade on a flat glass surface. The aim for the thickness of the wet slurry coating is 100–150 µm, which should be between 1 and 2 mg of dried active mass.

3.2.2. Cathode slurry

Two different methods were employed for making the cathodes. Initially, self-standing electrodes were produced with 1000 mg of active material mixed with 5, 10, or 20 w % of PTFE. AC C80 and C50 AC were both tried as the active material. Water, isopropanol, and THF were also tried at various points as solvents. The mixture was mortared by hand for up to 20 minutes before being rolled out like a dough. This dough was rolled to the desired thickness before electrodes were made using a 15 mm electrode cutter. Ball-milling was also attempted to improve surface contact. The self-standing electrodes crumbled to dust after being dried up and were not electrochemically tested as they were too fragile to be put into cells. It was also difficult to make the electrodes small enough to balance the capacity contribution of the thin-film Si@TiO_2 electrodes, which rendered them not relevant in the end.

After this was proven unsuccessful, it was decided to make AC electrodes coated on C-covered Al foil. These electrodes were made in 300 mg slurry batches with an 80:10:10 (w %) ratio of C80 AC, Super P, and PVDF. The procedure is equivalent to how anodes were made. The first step is to make the gel by adding 0.9 mL of solvent to a Thinky-cup before 30 mg of PVDF is evenly distributed over the liquid solvent. The solvent used was 1-methyl-2-pyrrolidinone (NMP) from Sigma Aldrich. This is done to avoid bits of solid material, just as with the CMC method as previously discussed for anodes. If there are bits of solid material in the gel, these are carefully cut up with a clean spatula before adding 0.2 mL extra NMP solvent and repeating the mixing procedure. A picture of the electrode tape is shown in Figure 10.

Figure 10: AC electrode tape with holes where electrodes have been punched out.

The slurry is then mixed in the Thinky-mixer for three minutes at 3000 rpm + 2.5 minutes at 700 defoaming. Next, 240 mg of AC and 30 mg of Super P are also distributed carefully over the gel and 0.9 mL of NMP is again added to the slurry. The mixing procedure is repeated, before an inspection of the viscosity and homogeneous slurry is done. If the slurry is still lumpy, the same procedure as for the gel is repeated. It is worth noting that the total amount of solvent should not differ from the designated 1.8 mL to avoid having a fluid with too low viscosity. Furthermore, NMP is reported to be a potential health hazard (especially to unborn children),[58] and it was therefore always handled with care in the fume hoods.

The slurry is coated on a C-coated aluminum foil using a handheld coating blade with a preset thickness of 100 µm. The dried coating was measured to be around 70 µm as the thickness of the foil and the evaporated solvent need to be subtracted. After drying the electrode tape overnight, the 11 mm diameter electrode disks are cut out using an electrode cutter.

Before going into the glovebox and being made into coin cells, the electrodes are dried overnight at 60 °C in a tube vacuum oven from Büchi. The electrodes are always measured on a scale inside the glovebox just before assembling the cells. This leads to some uncertainty as the pressure in the glovebox changes. By keeping the movement during weighing to a minimum and tiering the weight between each sample, the error is reduced. If the pressure should change between tiering and weighing, the tiering is repeated.

3.2.3. Slurry casting

During slurry casting (or slurry deposition), the Cu/Al foil is held in place by applying small amounts of ethanol under the copper foil, making the foil stick to the plate by surface tension. After slurry casting, the electrode tape is dried in air overnight. It is important to inspect the slurry before using it. The electrode tape is then either cut into strips of 3 by 8 cm with cleaned scissors or punched out to 11 mm or 15 mm diameter circular electrodes. These electrodes are then dried under vacuum at 60 °C in a vacuum tube oven from Büchi overnight.

It is important that the electrodes are not exposed to high-temperature heating. There is a balance between removing the water and retaining the structure of the binder-gel that needs to be kept during heat treatment. It is even more important that the electrodes cool down as slowly as possible as experience shows that the electrodes start to delaminate and the active material delaminates from the current collector. This is a result of the difference in thermal expansion of the binder-gel and Cu or Al foil.

All electrodes are transferred to an Argon (Ar 5.0, purity 99.999%) atmosphere LABmaster SP glovebox from MBRAUN with less than 0.1 ppm of H_20 vapor and O_2 gas in the vacuum-sealed Büchi tube.

3.3. Atomic layer deposition (ALD)

The TiO_2 coating was made by ALD synthesis using a custom-made pressure-cycling reactor named DUNE that is made by the NAFUMA group of the Department of Chemistry at the University of Oslo, UiO. (See Figure 11) The reaction chamber is fabricated by the local glassblowers at the UiO. Standard operating procedure for creating titania (TiO_2) coated anodes begins by producing the Si-based electrodes, as described in section 3.2.1.

Figure 11: The two pictures on the left show the outside of the DUNE reactor. The top left is the oven. The top right picture is inside the oven. The lower left is a picture of the software used to run the depositions.

3.3.1. Precursors

In this thesis, ionized water (H_2O) was chosen as a precursor to the oxygen in titanium oxide (TiO_2), while titanium tetra chloride ($TiCl_4$ or TTC) was chosen as a precursor to the titanium.

Name	Chemical formula	Supplier	Purity	Index #	Batch #
Titanium (IV) chloride	$TiCl_4$	Merck	≥ 99%	022-001-00-5	S6301782 122
Water (Type II)	H_2O	UiO	Resistivity (MΩ cm) > 1		

3.3.2. Substrates

Silicon wafers, with a thin oxide layer on top, were used as the model substrate in this work. Si-anode electrode tapes made with silicon, graphite, carbon black, and CMC, dissolved in water and coated on dendritic cobber foil. The silicon wafers were cut into A, B, and C substrates. The A-substrates were 10 cm long and 1.0 cm wide, and the B and C substrates were 4.5 cm long and 1.5 cm wide (see Figure 12). A-substrates were marked with an "A" on the non-reflective side of the silicon wafer, while the C-substrates had an arrow placed at the edge of its short side, pointing towards its middle. This arrow indicated the side that was open to flow during the synthesis, which will be described in further detail below. The marking was created by a pen with a tungsten carbide tip.

All substrates were cleaned with ethanol and plasma in a Harrick Plasma PDC-002-CE for 8 minutes. All the A and C substrates had a thin silicon oxide layer on the reflective surface that had been measured with an α-SE ellipsometer by J.A. Woollam Co., Inc. before the deposition to ensure the correct measurement of the TiO_2 film. The A-substrate had three measuring points (A1, A2, A3), counting from left to right, with the "A" marking indicating the reading direction. A1 and A3 were in the middle of the short sides, while A2 was located in the absolute center.

The C-substrate had seven measuring points evenly spaced apart (C1, C2, …, C7), starting from the non-marked short edge and moving towards the “arrow”-marked short side, with C4 as the middle of the substrate. See Figure 12 for a better understanding. It is important to measure along a line in the middle of the substrate as this will be where the titanium will be deposited during synthesis.

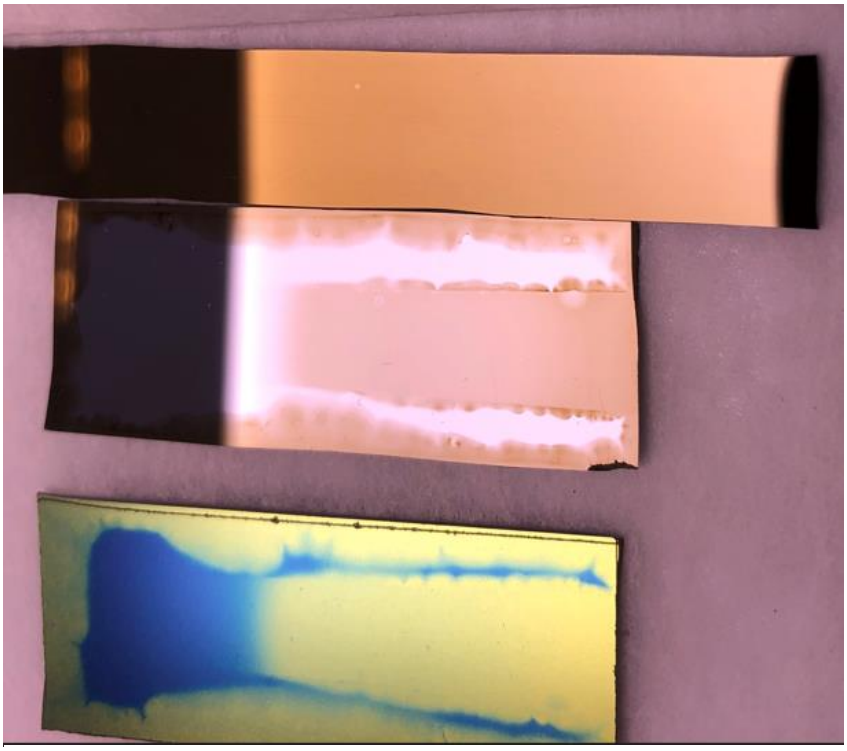

Figure 12: Picture of Substrates A, C, and B (in that order) after deposition.

A “sandwich” substrate was used to verify the coating's penetration of porous materials. The sandwich was made by placing the C-substrate with the reflective side up and placing a horseshoe-like Kapton tape film so that all sides except the one marked with the arrow. See . This Kapton tape is rectangular and the same size as the B and C substrates, but with an open section of the rectangle to expose it to the precursors during synthesis, as seen in Figure 12. After the Kapton tape film was placed on the C-substrate, the B-substrate was placed on top, with the non-reflective side toward the Kapton tape film and C-substrate. To keep the sandwich together, two paperclips were placed at the sides of the opening in the horseshoe Kapton film near the arrow and another along the short side opposite of the opening.

The sandwich substrate offers information on the penetration of the coating by measuring the thickness of the film grown on the C-substrate. In the ideal scenario, there should be an even thickness gradient from the inlet side of the horseshoe (C7) to the inner point (C1) indicating that the precursor gas was transported both in and out of the sandwich substrate. See Figure 13.

Figure 13: Picture of the sandwich before deposition.

The precursors must both be able to penetrate and leave the pores so that the surface of the electrodes can be evenly coated without plugging up the pores. Since a high surface area is important to the area-dependent properties of the electrode, it is necessary to avoid plugging the pores.

The sandwich was placed at the bottom of the reaction chamber, and the A-substrate was horizontally aligned with the electrode tape to make the conditions of the A-substrate and the electrode tape as equal as possible. The reaction chamber was connected to the ALD reactor, and the pump was switched on. The pressure inside the chamber was reduced to ~0.6 Torr for 5 minutes before introducing the nitrogen flow gas, after which the pressure rose to ~4 Torr.

The electrode tapes were cut out to approximately 3 cm in width and 8 cm in length. Two paper clips were placed at each end to attach the tapes to a silicon wafer that was used to support and hold the electrode tape fixed during the deposition (see Figure 14). One electrode strip produced four electrodes with a diameter of 15 mm that could be utilized in electrochemical cells. The edges of the electrode strip should not be used for making electrodes since the thickness of the slurry-coating is more irregular than the short side edges. Furthermore, the surface covered by paper clips was not coated with TiO_2. In general, any contact with the surface of the electrode influences the conditions for the ALD coating and therefore should be avoided if possible.

Figure 14: Si electrode strip attached to a Si-wafer using paper clips.

Table 1: Table showing the specifics of the Si wafers used in this project.

Wafer type	Wafer diameter	Wafer thickness	Dopant type	Dopant element	Lot #	Country of origin
Silicon wafer	200 ± 0.2 mm	> 600 µm	P	Boron	MG960	Japan

3.3.3. Pulsing parameters and pulsing ratios

Table 2 describes the schedule for each cycle.

Table 2: Table showing the ALD script.

	$TiCl_4$	Pump	Wait	Pump	Wait	H_2O	Pump	Wait	Pump	Wait	Pump	Wait
[s]	2.5	50	15	15	20	**1.5**	50	20	20	20	20	20
	$TiCl_4$		**Purge 1**			**H2O**		**Purge 2**				

3.3.4. Description of the atomic layer deposition (ALD) synthesis of TiO_2

The reactions in the TiO_2 synthesis took place in three steps, which are illustrated in Figure 15 and described by the reaction equations described below, [59]. It is imperative to point out that *(g)* refers to a gas-phase species, and *(s)* refers to a surface species [60]:

$$SiO_2 + H_2O \rightarrow SiO(OH)_2, \qquad (1)$$

$$n(-OH)\ (s) + TiCl_4\ \ (g) \rightarrow (-O-)_n TiCl_{4-n}\ (s) + n\ HCl\ (g), \qquad (2)$$

$$(-O-)_n TiCl_{4-n}\ (s) + (4-n)H_2O\ (g) \rightarrow (-O-)_n Ti(OH)_{4-n}\ (s) + (4-n)HCl\ (g), \quad (3)$$

The number *n* in equation (2) and (3) is defined as the average number of Cl-ligands detached by the titanium precursors ($TiCl_4$) [60].

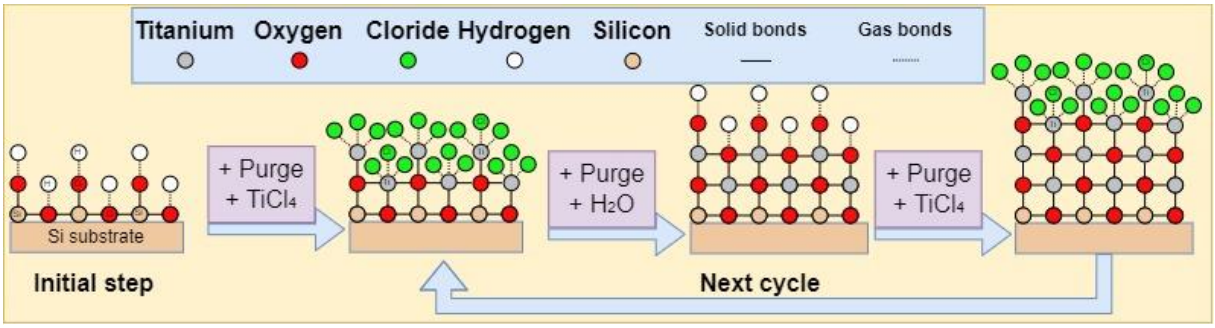

Figure 15: Schematic figure of the deposition of TiO_2 from $TiCl_4$ and H_2O. Reproduced from,[3].

Equation (1) describes the initial layer grown on the Si wafer. Equation (2) and (3) describes the growth of the Ti layer and an O layer, respectively. The process of growing thin films by ALD is a self-limiting process, meaning that all active sites were filled before proceeding to the next step. Nitrogen gas (N_2) was used as the inert purge gas to flush out the remaining gases between cycles. The first step in the cycle was to make the water react with the oxygen in the oxide layer on the surface substrate, leaving hydroxide groups in all active sites on the substrate's surface.

3.4. Coin cell battery assembly

While cells may be packed in various forms, only coin cells built out of a stainless-steel casing were considered in this thesis. Coin cell assembly was carried out in an Argon (Ar 5.0, purity 99.999%) atmosphere LABmaster SP glovebox from MBRAUN with less than 0.1 ppm of H_20 vapor and O_2 gas. The standard operative procedure (SOP) for cell assembly was based on the recipe described by Brennhagen,[5] which reverses the customary assembly order used in the battery industry (see Figure 16).

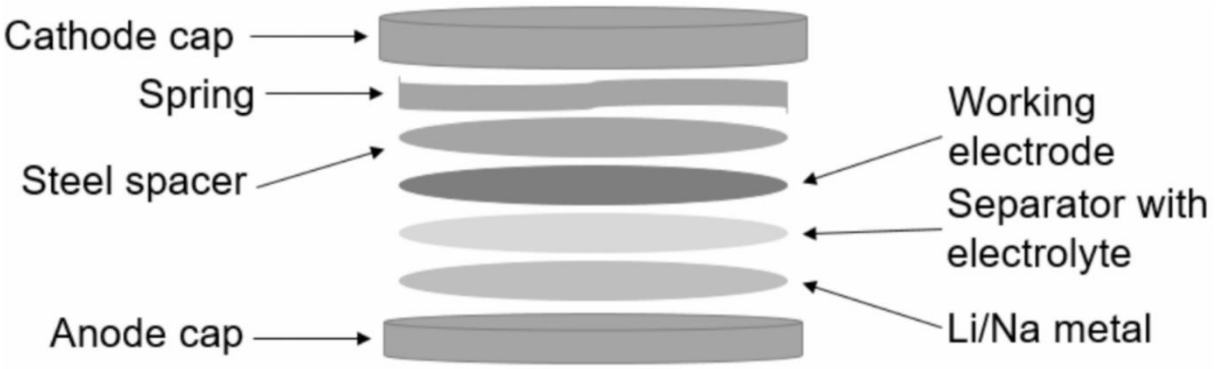

Figure 16: Illustrative description of the chronological order of coin cell battery assembly. Reproduced with permission from Brennhagen,[5].

To make half cells, the initial step was to place the steel 304 anode cap with the toroidal seal facing up. The next step in the process was to brush off the oxide layer of the Li-metal electrode using a toothbrush. By brushing the surface of the Li-metal, it slightly increased the surface of the Li-metal electrode. The Li metal was placed in the anode cap and covered by a 16 mm Whatman glass fiber separator. The total weight of the electrodes was measured on a scale inside the glovebox. After weighing all the silicon electrodes in the glovebox, 80 µL of electrolyte were added by a VWR pipette. The electrolyte was a 1.2 M $LiPF_6$ in 3:7 ethylene carbonate:ethyl methyl carbonate (EC:EMC) with additives of 10 wt.% fluoroethylene carbonate (FEC) and 2 wt.% of vinylene carbonate (VC), made by Solvionic.[38] Next, the silicon working electrode was added with the slurry-coated side facing down toward the separator. On top of the current collector side of the electrode, a steel spacer and a spring were added to apply pressure to the stack. The stack was sealed off with a cathode cap and pressed together with a coin cell press.

Table 3: Table of the components being used in making of cells. The electrodes and electrolytes are excluded as they are described elsewhere.

Coin cell part	Material	Specifications	Supplier
Cathode cap	Stainless steel, 304	CR2032	Pi-Kem
Steel spring	Stainless steel, 304		Pi-Kem
Steel space	Stainless steel, 304	Diameter: 15.8 mm Thickness: 0.5 mm	Pi-Kem
Separator	Glass fiber - Whatman paper grade GF/C	Diameter: 16 mm Porosity:	GE
Anode cap	Stainless steel, 304	CR2032	Pi-Kem

Table 4: Table showing the specifics of the Li-metal RE.

Component	Description	Specifications	Purity	Supplier
Half-cell reference electrode	Pre-cut Li-metal discs	Diameter: 15.5 mm Thickness: 0.4 mm	≥99.9 %	China Energy Li CO

Table 5: Table showing salts, solvents and additives used in the electrolytes of this project.

Name	Abbreviation	Chemical structure	Role
Lithium hexafluorophosphate		$LiPF_6$	Salt
Ethylene carbonate	EC	$(CH_2O)_2CO$	Solvent
Ethyl methyl carbonate	EMC	$C_4H_8O_3$	Solvent
Fluoroethylene carbonate	FEC	$C_3H_3FO_3$	Additive
Vinylene carbonate	VC	$C_3H_2O_3$	Additive

Source for tables, Brennhagen,[5].

3.5. Morphological characterization

This section discusses the characteristics of the TiO2 coating that were deposited on Si wafers, and electrodes. Characterization methods used as was spectroscopy ellipsometry, visual inspection, and SEM pictures.

3.5.1. Spectroscopy ellipsometry

As a bonus, the B-substrate serves as visual control of the synthesis's success. When visually inspecting the color and shape on the non-reflective side of the silicon wafer, certain criteria need to be met. The substrate should have a coating in the shape of a horseshoe with a gradient from the open to the closed side, as shown on the right in Figure 17. The presence of this horseshoe shape indicates that the coating has penetrated the porous material rather than merely remaining on the top surface. A gradient on the A-substrate indicates that the coating is uneven, which is not desirable (see the left side of Figure 17).

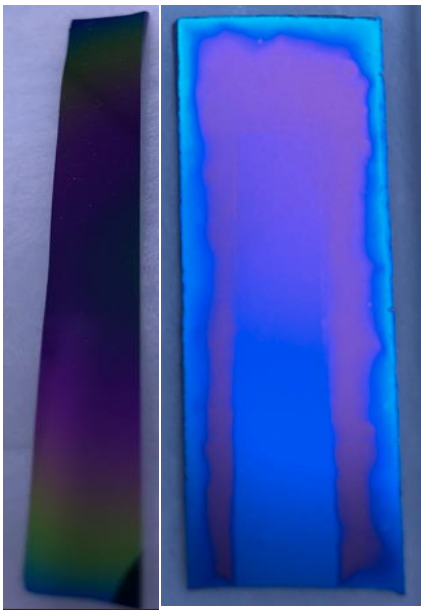

Figure 17:To the left is an A-substrate with a coating gradient, shown by a color shift. To the right there is a B-substrate with a horseshoe shaped coating with a coating gradient inside.

3.5.2. Visual inspection of B-substrate

As a bonus, the B-substrate serves as visual control of the synthesis's success. When visually inspecting the color and shape on the non-reflective side of the silicon wafer, certain criteria need to be met. The substrate should have a coating in the shape of a horseshoe with a gradient from the open to the closed side, as shown on the right in Figure 17. The presence of this horseshoe shape indicates that the coating has penetrated the porous material rather than merely remaining on the top surface. A gradient on the A-substrate indicates that the coating is uneven, which is not desirable (see the left side of Figure 17).

3.5.3. Scanning electron microscopy (SEM)

All SEM measurements were made through the in-house Hitachi SU8230 Ultra High-Resolution Cold FE-SEM, as shown in Figure 18. There were problems with the samples accumulating charge, making it difficult to obtain quality pictures in high magnification. Charge accumulation in the sample may result in drift in the SEM, lower topological contrast, and lines stretching over the pictures. These effects were visible in most of the pictures obtained by the SEM instrument.

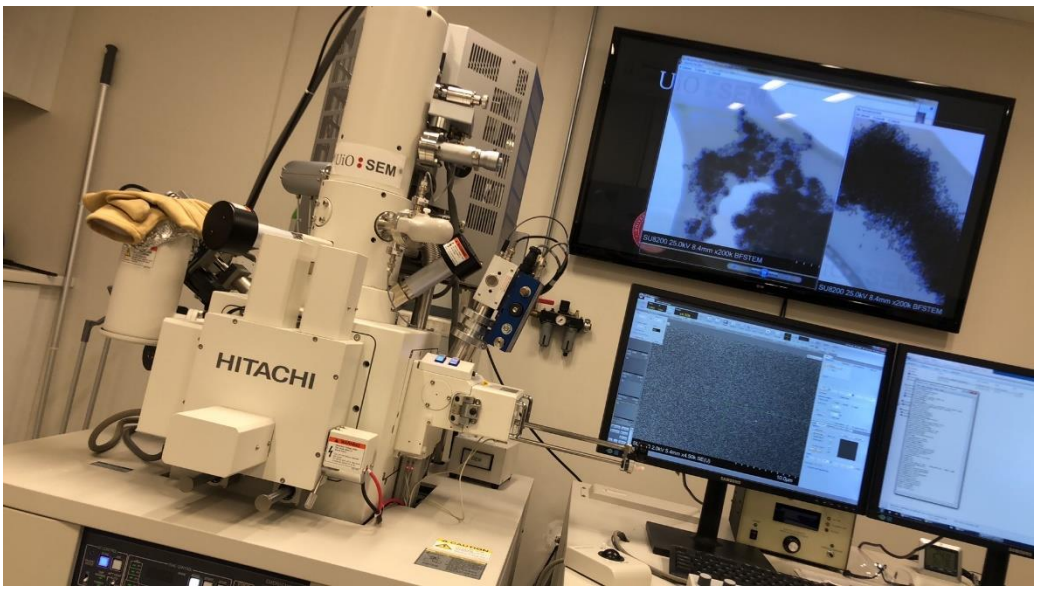

Figure 18: Picture of the internal SEM setup at the UiO.

A few things needed to be considered to obtain the best possible images. First, the samples were made as thin as possible to reduce the ratio of bulk to the surface and reduce the charge accumulation. Furthermore, reducing the working distance between the last lens of the SEM and the sample improved the picture resolution but lowered the depth of focus. This was only considered for pictures of the surface as an EDX analysis mapping the atoms in the sample requires much higher working distances.

During imaging, an acceleration voltage of 1, 2 and 5 kV and an emission current of 10 µA were used. The charge accumulation inreased for Si and SiP_x powders as they have limited electron conductivity. Si and SiPx electrodes have the current collector as well as graphite and carbon black to help the electron conductivity. On the other hand, the electrodes also have more bulk to accumulate charge in.

3.6. Electrochemical characterization

In the following chapter, the characterization methods to determine the electrochemical properties of the cells will be descried. The electrochemical characterization is evaluation of the cells actual performance and is therefore it is separated from the characterization of the surfaces.

GC test of half cells were done on the NEWARE battery tester instrument in the voltage range 50 mV to 2.9 V. The voltage range were adjusted according to what was being tested. All test of full cells and CV tests of the half cells were done on the Biologic MPT-2 research grade battery tester instrument, with a maximum current and voltage resolution of 760 pA and 5 µV, respectively. In the voltage range of 0 – 3 V, the resolution was 50 µV. All tests of full cells were done in the voltage range window of -3.3 - 3.3 V, with bandwidth of 4. This increased the voltage resolution to 100 µV.

Electrochemical characterization includes GC and CV measurements of the cells. The different scripts are described later in the experimental part. The CV measurements are plotted as potential versus current and shows the peaks of reduction and oxidation for the cells. Multiple scan rates are used on the initial full cell to determine the shift of peaks.

The GC measurements are done in two separate ways, giving three different plots of representations. Standard long-term GC measurements where one current is used during the whole test, apart from the three first cycles of Si. These three first cycles referred to as the “formation cycles”, where the current is half of the testing current. These measurements often last until the capacity of the cell is diminished and can therefore last for many cycles.

Rate capability tests are also GC measurements, but here the current is fixed for five cycles, before doubling the current. This is repeated going from 0.5 A/g to 20 A/g for the full cells. The table in the experimental section also states what this will be in areal specific current. See later in the experimental section for more details. These two GC measurements are displayed as cycle number versus capacity. The last way of representing results, is to take the data from the long-term GC measurement and display them as capacity versus potential. This will give information on the capacity until that potential value. All plots will be mentioned and described in the results sections and no illustrations will therefore be given at this point.

All numbers for capacity when either AC or TiO_2 is involved are always presented as a function the anode areal, as determining the mass of the active material is difficult for several reasons. First of all, there may be several active materials with different contributions dependent on the voltage window. Secondly, it is difficult to determine the mass of the thin TiO_2 layer on the porous surface. This is done as an alternative to specific capacity. For Si|Li or SiPx|Li systems, where the voltage window includes the oxidation peak of Si, the specific capacity is used since the mass of Si is easily determined and will be dominating the capacity. When the oxidation/reduction peaks are not included, the data is presented per area of Si@TiO_2 electrode. The samples being compared are made from the same electrode tape and is only separated by different durations of ALD treatment.

As a final remark, it has to be said that all cells being compared are made from the same electrode tape. They have the same active mass of AC, same surface area of anode and Solvionic electrolyte. They are all cycled by the same program described in the experimental part under “Full cells”. All full cells are cycled at 0.1 mV/s, unless otherwise stated, and the initial test for all full cells are a CV measurement. The cycling script is identical for all comparable full cells.

3.6.1. *Si and SiP_x half cells*

Table 6: Testing schedule for Si and SiPx half cells

Duration	Current	Mode	Units
12 hours	0	Rest	[hours]
3 cycles	180	GC	mA/g
500 cycles	360	GC	mA/g

For testing of half cells, GC measurements of three formation cycles was done at what is equal to C/20 for Si. The rest of the program was at C/10. Multiple voltage ranges were tested. Firstly 0.05 – 2.0 V was used to test the first half cells containing Si, while 0.1 – 2.0 V was also used. Later, 0.05 – 2.8 V was also used as this is includes the voltage of the TiO_2 thin films.

3.6.2. *Maximum capacity tests*

Some of the cells have been tested for its maximum capacity in the first cycle before long-term cycling. This means that the cell will have 5 steps of discharging at different currents before charging. These steps will use a fixed current during the initial discharge until the cut-off voltage is reached. This will initiate a 15-minute waiting sequence before discharging again, without charging. The reason behind doing it this way is that the insertion of the Li-ions becomes increasingly demanding for the structure because of diffusion, meaning it takes more time to add Li to the electrode. This could also be solved by running the experiment at minimum voltage during the first cycle, but that would have been way too time consuming. The lower current limit for the NEWARE instrument is 20 µA, so the last step will for many cells be set to this value instead of what would be C/200 and C/400. An alternative way to this is the CCCV technique which reduces the voltage to the cut-off voltage using a fixed current, such as C/20, followed by holding the cut-off voltage applying a variable current.

Table 7: Table describing the current being used in GC measurements of the half cells. Both with C-rates and specific current.

C-rate	C/10	C/20	C/50	C/100	C/200	C/400
Specific current [A/g]	360	180	72	36	18	9

3.6.3. Initial full cell test

The testing schedule of the first balanced full cells was done in the voltage range of 1.0 – 2.8 V, and is shown in Table 8. It was divided into two parts, where the first consist of multiple CV scans with multiple scan rates. This is The testing schedule is inspired by the work of Calcagno et al. for TiO_2 beads as anodes in LICs,[61]. This was done because literature has shown LICs of AC|TiO2 to be stable in this area, [61]. It is worth noticing, that the first cycle was a "Maximum capacity test" which is described in the section by the same name. This will give a high initial capacity for the cell, but also lower the capacity retention as it puts a lot of stress on the structure.

Table 8: Testing schedule for the CV and GC measurements of the initial full cell of AC|Si@TiO2

Mode	CV	CV	CV	CV	CV	CV	CV	CV	CV
Scan rate [mV/s]	50	20	10	5	1	5	10	20	50
Cycles	5	5	5	5	5	5	5	5	5
Step #	1	2	3	4	5	6	7	8	9

Mode	GC	GC	GC	GC	GC	GC	GC	GC	GC	GC	GC	GC	GC	GC
Specific current [A/g]	0.5	1	2.5	5	10	15	20	15	10	5	2.5	1	0.5	1.0
[µA/cm²]	8	17	42	85	170	250	340	250	170	85	42	17	8	17
Cycles	5	5	5	5	5	5	5	5	5	5	5	5	5	5000
Step #	2	3	4	5	6	7	8	9	10	11	12	13	14	16

3.6.4. Full cell tests

For characterizing the TiO2, the voltage window was set to 0.8 – 2.8 V, as mentioned before. This was done to exclude the potential values where alloying of Si and Li occurs, and hence eliminating the capacitive contribution from Si. As references, tests of pure Si have been done in the voltage window of 0.1 – 2.8 V.

The specific current is set to be related to the areal of the anode, which is set to be 1.77 cm^2. Since weighing the AC electrodes inside the glovebox is connected to significant uncertainty, all electrochemical tests have been conducted under the assumption that the electrodes have equal active mass. This is justified by doing by weighing several electrodes in air multiple times and taking the average or the mass.

The electrochemical test is divided into parts to explore all properties of the device. An initial CV-diagnostic is done to monitor the reactions happening during the initial cycles. This is followed by a rate capability test to measure the capacity retention of the system after both high and low currents. In an ideal case the measured capacity step 2 should be the same as in step 14.

Mode	CV	GC	GC	GC	GC	GC	GC	GC
[A/g] or [mV/s]	0.1	0.5	1	2.5	5	10	15	20
µA/cm²		8	17	42	85	170	250	340
Cycles	3	5	5	5	5	5	5	5
Step #	1	2	3	4	5	6	7	8

Table 9: Testing script for all full cells tested on the Biologic is listed in the table below. Due to the length of the script, the table needed to be divided into two parts. It is a CV scan at step 1, then a rate capability test from step 2 to 14, before a new CV comes at step 15. In the end it is a long-term GC measurement.

Mode	GC	GC	GC	GC	GC	GC	CV	GC
[A/g] or [mV/s]	15	10	5	2.5	1	0.5	0.1	1.0
µA/cm²	250	170	85	42	17	8		17
Cycles	5	5	5	5	5	5	3	5000
Step #	9	10	11	12	13	14	15	16

3.7. LICs in this thesis

The LICs discussed in this thesis have an AC positive electrode versus a Si-based or Si@TiO2-based negative electrode. All TiO2 electrodes produced during this project were Si electrodes coated with a thin film TiO2, Si@TiO2. By avoiding the voltage values for the alloying of Si and Li, it was assumed that Si had a negligible capacity contribution to the system. The remaining capacity contribution from the anodes then came from TiO2. This assumption was verified by testing Si electrodes (without the TiO_2 film) in the same voltage window and measuring the capacity contribution. During shallow cycling, only the Li in the near-surface layer contributed to the faradaic charge transfer, while the rest of the Li in bulk was inactive. A large active surface area meant that there were more reactions close to the surface.

4. Results

This section will present the results obtained through the course of the present master project, while a deeper explanation and rationalization will be done in the discussion part of this thesis. We will start to introduce the results from the ALD coating of the electrodes. This will be followed by the electrochemical characterization of the cells made in this project. First, half-cells will be considered to lay the fundamentals for further exploration of full cells. For full cells, some initial electrochemical tests will be done to help construct the full cells. In the end, the results from electrochemical tests performed at different full cells will be presented.

4.1. Electrode characterization

4.1.1. Deposition of titanium oxide

This section is dedicated to present the ellipsometry results of the ALD modified samples. These measurements have been performed on model Si-wafers to estimate the thickness, penetration, and growth of the TiO_2 coating on the electrodes, Table 10. Additional results, including the gradient values and raw data, are shown in Table 13.

Table 10 summarizes the results from the ALD depositions. The details of the depositions are described in the experimental section. The first column, labeled “ALD ID”, indicates the ID number of the experiment. This list starts at MR5009 as the prior depositions were test depositions performed to ensure ALD growth, and not CVD growth. CVD growth occurs when water is in contact with $TiCl_4$, caused by i.e., a leakage. The initial depositions were performed at 100 °C, however the experiments conducted in parallel project allowed us to increase the operating temperature to 120 °C for the rest of the project, [62]. The compromise between the CMC decomposition temperature and the ALD temperature window for TiO_2 deposition from H_2O and $TiCl_4$ was the deciding factor of the choice.

The last two columns, labeled “Film gradient substrate C” and “Film gradient change substrate C”, describes the coating gradient of the C-substrate which is related to the penetration of coating through the pores of the electrode. These numbers represent the average gradient of the coating and the average change between them, which will be the first and second derivative of the coatings.

The second column, labeled “Cycles”, indicates how many ALD cycles were performed. Each cycle takes 254 seconds, and with an hour waiting, a deposition of 405 cycles takes almost 30 hours. The third column, labeled “Cell ID”, indicates which electrochemical cells were fabricated from the given deposition. In the list, you may see that many of the depositions has not produced electrodes. This is because some of the experiments failed to produce any testable electrodes, and hence they are not given a “testing name”. Each deposition produces up to four electrodes suitable for electrochemical testing.

The fourth column, labeled “Avg. Thickness”, contains the average thickness of the 3 points measured on the A substrate, which is described in the experimental section. The growth per cycle, GPC, of the film is listed in the fifth column, labeled “GPC”, indicates how much the film grows on average per cycle. The sixth and seventh column describes means of estimating the unevenness of the coating thickness on the A substrate.

As an example, deposition MR5026 has a thickness of 22.91 nm, but the difference in thickness between the highest measured value and the lowest is 92 %. Furthermore, the middle of the of the wafer has 18 % less coating than the average of the sides. From this we can say that this deposition has a very thick coating on one side, and rather thin on the other side. This makes the deposition very uneven, and the electrode tape should not be used for further electrochemical testing.

Table 10: Information on ALD depositions.

ALD ID MR50xx	Cyc	Cell ID MR_B_	Avg. Thickness [nm]	GPC nm/cycle	Film gradient (Max-Min) [%]	Film gradient (Mid-Side) [%]	Film gradient Substrate C	Change of film gradient Substrate C
9	200		5.46	0.027	6.7	-2.6	0.65	-0.21
10	200		4.00	0.020	18.9	-9.0	0.31	0.02
11	200		6.64	0.033	2.1	5.2	2.80	3.23
12	200		7.97	0.040	9.6	20.8	0.38	0.56
13	285		10.75	0.038	3.8	4.6		
14	353		12.99	0.037	3.6	7.1		
15	407		243.95	0.599	10.1	31.7		
16	353		24.08	0.068	1.6	4.4		
17	216		20.69	0.096	14.4	21.9		
18	132		9.45	0.072	10.6	29.2		
19	169		21.69	0.128	21.7	37.1		
20	145		7.83	0.054	7.4	14.9		
21	185	71,72,73	7.76	0.042	23.1	15.7	0.93	0.05
22	238		14.05	0.059	21.4	41.8	0.27	-2.73
23	200		19.33	0.097	15.8	47.2	0.50	0.31
24	200		16.30	0.082	70.5	44.8	2.47	0.24
25	140	77,78,79	5.26	0.038	3.0	-18.0	0.34	-0.07
26	160		22.91	0.143	92.0	-18.0	0.06	0.18
27	160		7.09	0.044	7.6	38.8	0.18	0.00
28	180	80,81,82	6.77	0.038	6.6	19.8	0.61	0.25
29	220	83,84,85	7.73	0.035	8.3	19.0	0.77	0.10
30	285		11.91	0.042	39.5	21.8	0.75	0.33
31	310		9.54	0.031	11.5	8.5	1.42	0.62
32	310		10.07	0.032	24.9	-2.9	0.60	0.47
33	310		0.00	0.000	0.0	0.0	0.00	0.00
34	140	86,87,88	3.03	0.022	4.0	9.6	0.27	0.04
35	200		4.87	0.024	7.5	6.4	0.59	0.21
36	205	89,90,91	7.70	0.038	17.3	16.5	0.89	0.20
37	310		9.34	0.030	5.3	1.4	0.97	-0.17
38	330		8.93	0.027	0.4	-2.7	0.57	-0.31
39	205		7.32	0.036	10.3	18.8	0.45	0.43
40	205	96,97,98	7.88	0.038	0.1	14.9	0.24	-0.07
41	205	99,100,101	4.76	0.023	6.0	12.5	0.14	0.26
42	310		8.35	0.027	3.7	15.0	0.42	0.37
43	405		8.72	0.022	3.9	11.5	0.56	0.08
44	215	124,125,126	8.18	0.038	6.1	9.0	0.99	0.36
45	197	109,110,111	16.37	0.083	16.9	20.1	0.82	0.35
46	160		4.40	0.027	4.4	21.9	0.24	0.01
47	170		3.32	0.020	4.5	8.1	-0.07	0.16
48	205	127,128,129	4.70	0.023	1.8	10.5	0.51	-0.03
49	215	112,113,114	4.73	0.022	11.5	7.6	0.22	-0.11
50	300	115,116,117	6.46	0.022	0.8	13.8	0.48	0.09

4.1.2. SEM

This section describes the results obtained from SEM characterizations of the Si powders and various electrodes used in this project. shows the Si nanoparticles used in this project to make electrodes. The picture shows that we have relatively uniform size distribution of spherical Si nano particles. There are traces of particle agglomeration, as is known to occur for gas phase pyrolysis synthesis of Si,[63]. The lines on the picture are effects from charge accumulation and should be disregarded. Keep in mind that the x20.0k zoom is only valid for the screen of the machine the picture was taken on and is there just as a reference between the pictures.

From the scalebar in Figure 20 we can, by using ImageJ by Fiji, estimate an average particle diameter size of 100 randomly selected particles. This is done by relating the number of pixels on the picture relative to the scalebar of 2.0 µm. From this we have that by the average diameter of the particles are 56 ± 20 nm. This value covers 95 % of all samples using 2 standard deviations, (σ). The histogram showing the size distribution is shown in Figure 19.

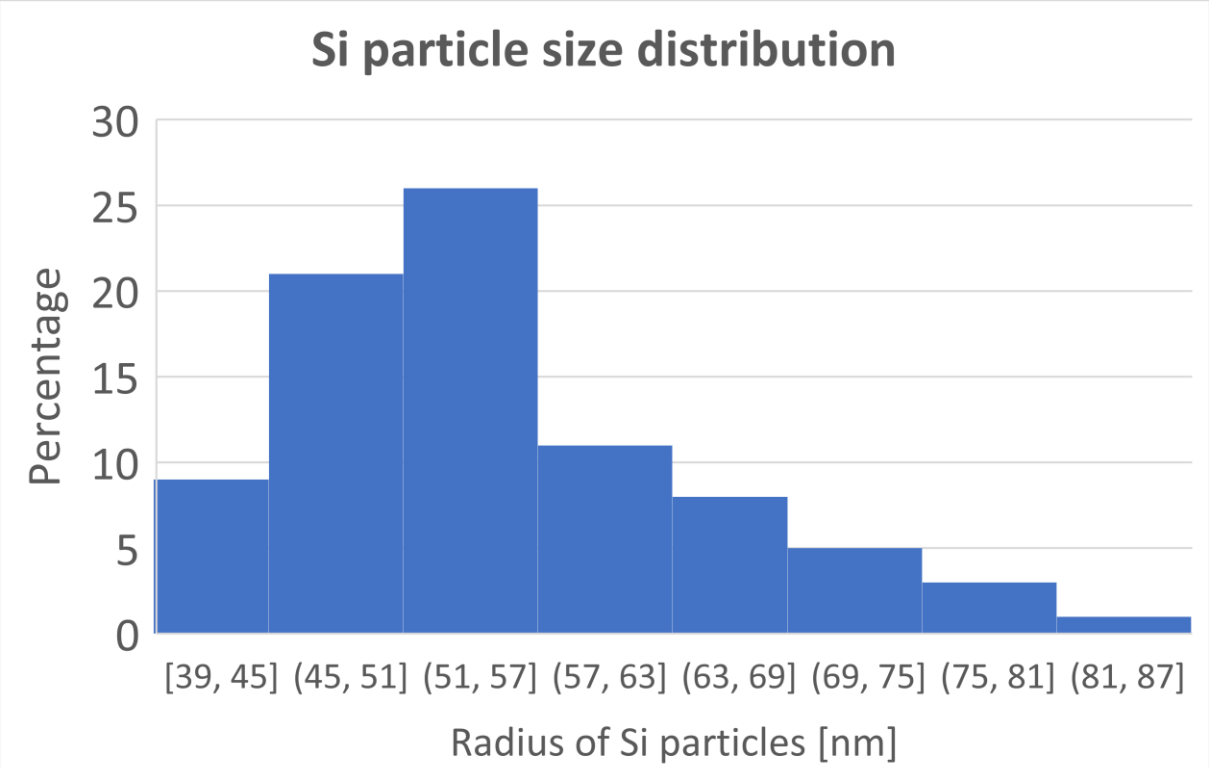

Figure 19: Histogram showing the size distribution of Si particles.

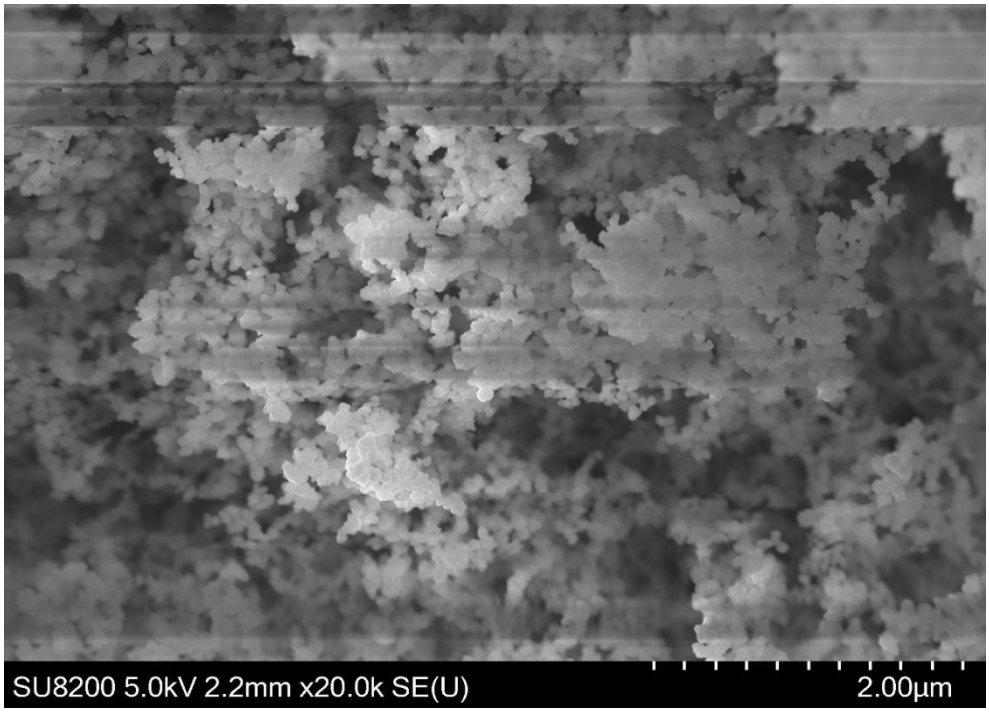

Figure 20: SEM picture of the Si-powder used in this project.

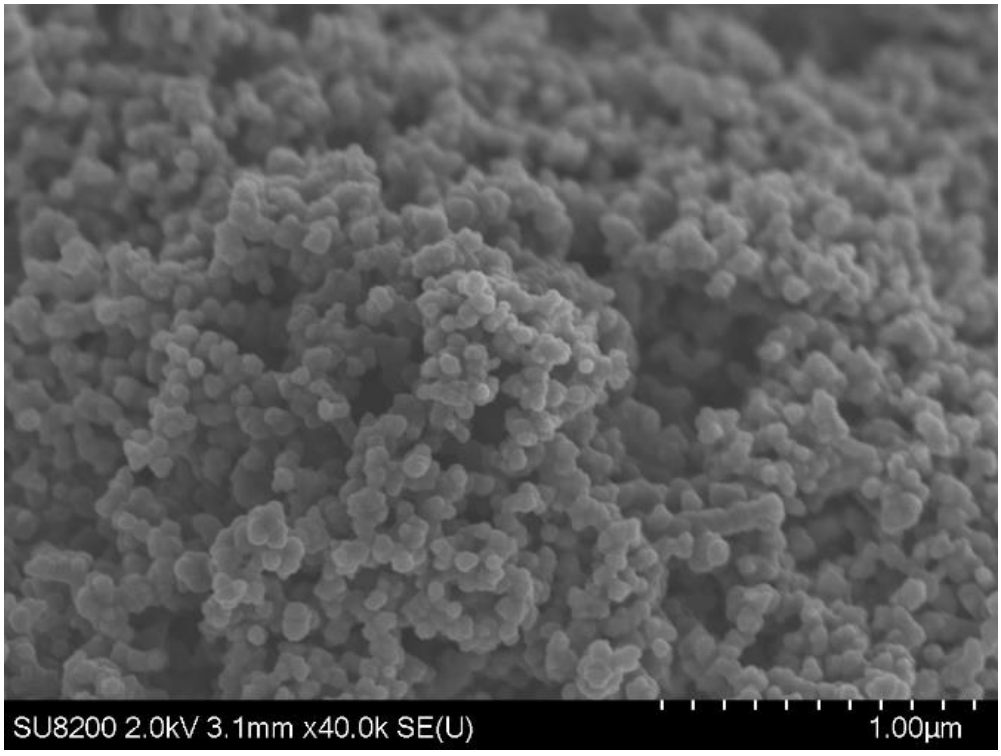

Figure 21: Picture showing one of the Si@TiO_2 electrodes being used in this project.

Figure 21 shows a picture of the same pristine Si@TiO_2 electrode which is being used in this project. Here the high porosity of the microstructure becomes more visible. Figure 22 shows the SiP_x electrodes used in this project.

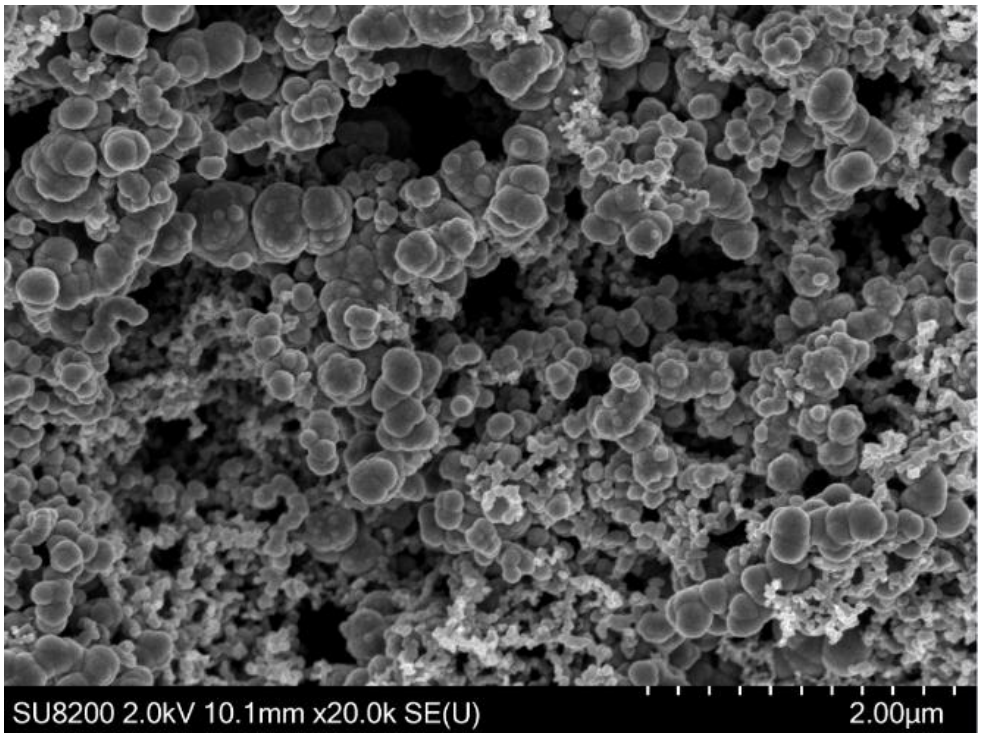

Figure 22: Picture of one of the SiP_x electrodes that is being used in this project.

4.2. Electrochemical characterization

In this section the data from electrochemical tests is presented, and some important aspects are highlighted. These points will be described in further details in the discussion section. In the end, the meaning of these results will be answered by comparing them to relevant results from this project and literature.

4.2.1. Half cells

4.2.1.1. Validation of voltage ranges

Determination of the voltage window was made possible by checking literature for oxidation voltages and conducting CV scans of Si|Li, SiP_x|Li and Si@TiO2|Li half cells. We check for the highest oxidation peak for Si, as the testing of TiO_2 needs to be done over this potential. Different scan rates and voltage windows of 0.05 V – 2.9 V, 0.8 V - 2.8 V and 1.0 V - 2.8 V were conducted to test this. Literature suggested oxidation peaks around 0.54 V, for Si in Si|Li half cells, when scanning at 0.1 mV/s,[64]. This was used as a reference point before conducting the CV scans, and our results displayed in Figure 24 supports this claim. The peaks indicate a Faradaic charge transfer due to redox reactions.

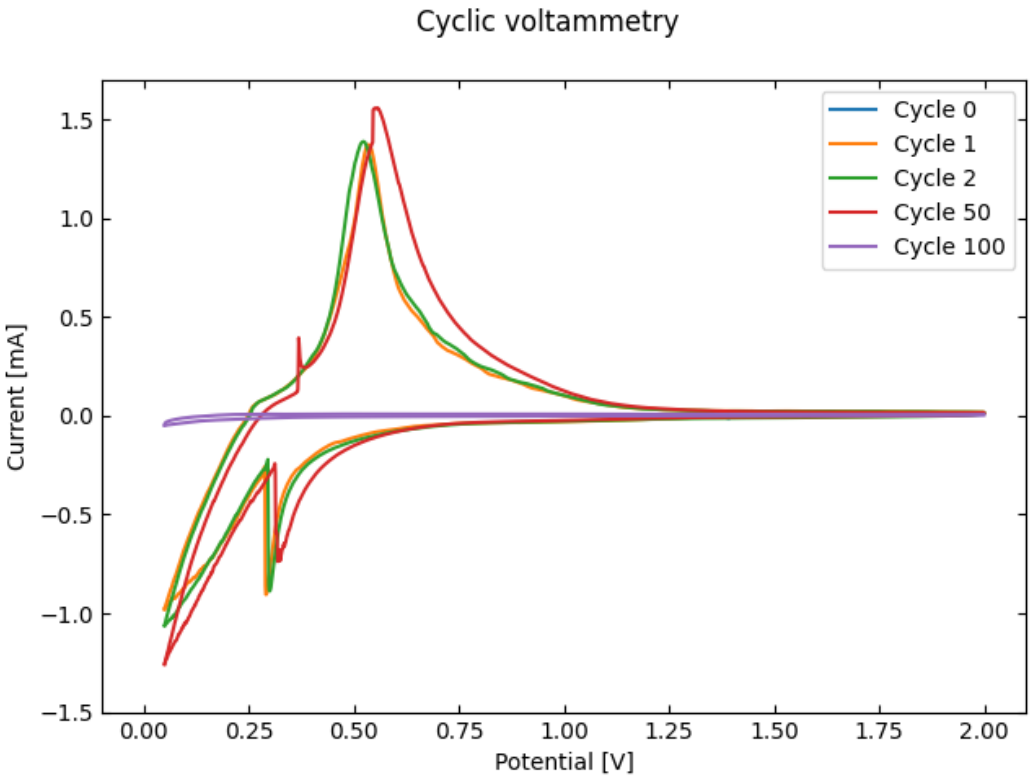

Figure 23: Results from a 100 cycles 0.1 mV/s CV scan of SiP_x|Li half cell.

When the window voltage was to a value higher than the reduction/oxidation peaks of Si, there should be no alloying of Si and Li. To be certain that Si does not contribute electrochemically directly, a lower cut off voltage of 0.8 V was set during testing. TiO_2 have multiple oxidation peaks, depending on various factors which will be investigated in the discussion section. Selecting of the upper cut-off voltage was therefore set to be 2.9 V based on reports from Liu et al. on anatase TiO_2,[65]. The voltage window of the cell tested in present work was later adjusted to be from 0.8 to 2.8 V.

4.2.1.2. Half cells of Si@TiO_2|Li

Half cells of Si@TiO_2|Li was tested in the voltage window 0.8 - 2.9 V using long term GC testing. The two upper pictures in Figure 25 shows the results from the capacity versus potential for two different coating thicknesses. The samples have a 5 and 8 nm thick TiO_2 coating on Si-electrodes. Out of the 5000 cycles recorded, every 500th cycle is included in addition to initial five cycles. Some relevant cycles between cycle 5 and 500 are also chosen.

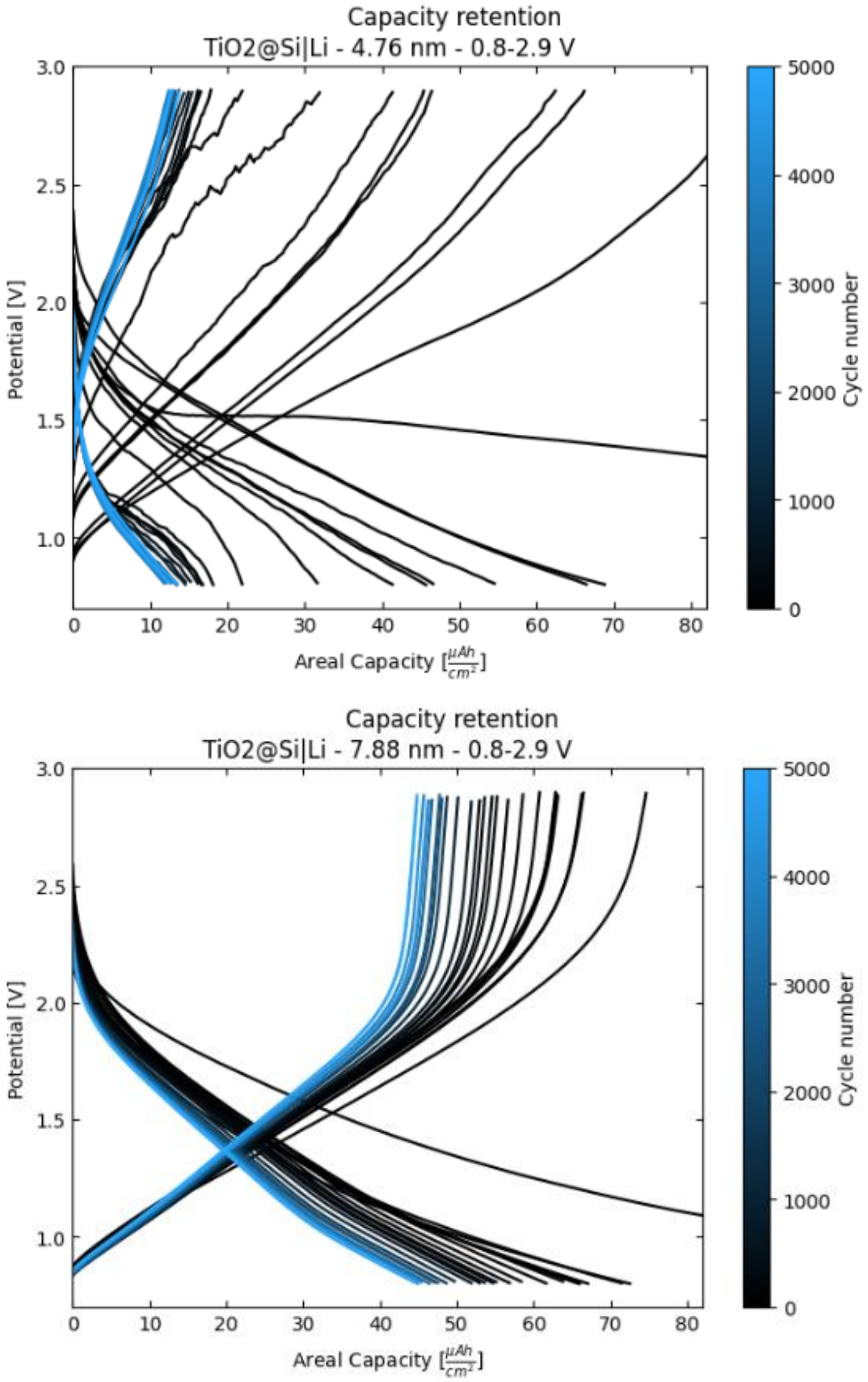

Figure 24: Capacity versus the potential for two electrodes with 5 and 8 nm thick TiO_2 coatings are labeled as 4.76 and 7.88 nm.

4.2.2. Full cells

In this section the results directly connected to the full cell LICs presented as well as the comparisons are made between the performance of reliable cells measured under similar conditions. However, before this is initiated a justification of the process of balancing the anode and cathode in LICs will be presented. The balancing is based on the results acquired from the half cells.

4.2.2.1. Balancing of full cells

To optimize the LIC full cell components, it is important to properly balance the storage contribution from the anode and cathode. The capacity contributions of both electrodes need to be about the same for achieving balance. Since the production of anodes are the most time-consuming due to the ALD process, the choice was made to balance the AC cathodes versus the actual capacity contribution of the anode.

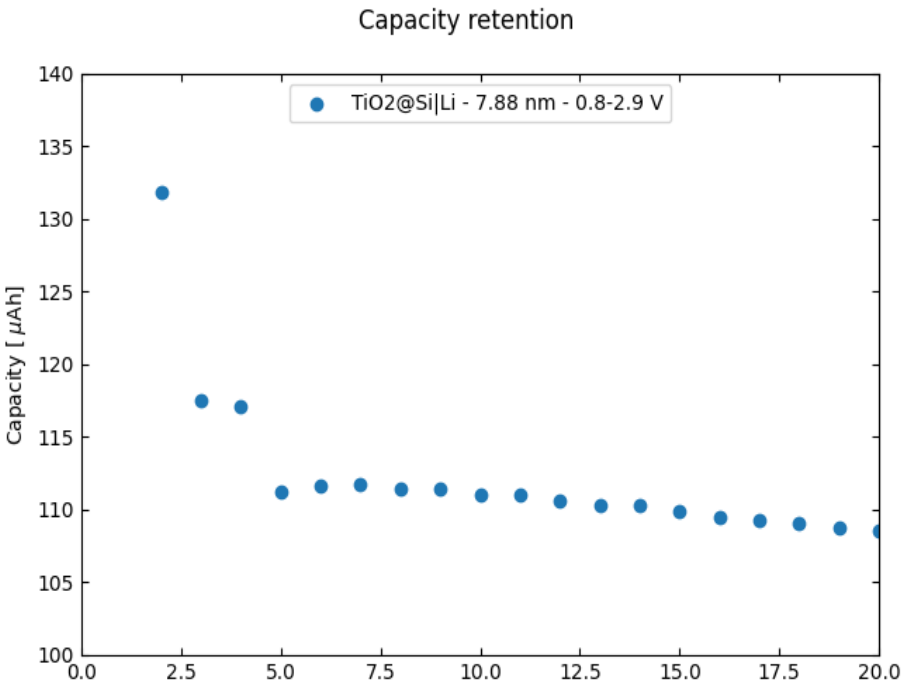

Figure 25: Capacity data from a Si@TiO2|Li half-cell.

A zoomed in version of the capacity data of the 8 nm thick Si@TiO_2 electrodes from Figure 32 are presented in Figure 26. Figure 26 does not consider the mass or area of the electrodes, but rather the measured capacity of the device. The first three cycles are excluded from the calculations because they do not fit the trend of the graph. The average capacity in this selection of points is rounded to be 110 µAh, which will be the capacity we are aiming for with the AC electrodes when balancing full cells.

Once the desired capacity for the AC electrodes is established, all we need to find out is how much active mass of AC this will represent. This is done by utilizing the theoretical capacity of AC. In this equation *Q* is the capacity and *m* are the mass.

$$m_{Active} = \frac{Q_{measured,TiO_2}}{Q_{theoretical,AC}} = \frac{0.11\ mAh}{333\ mAh/g} \approx 0.33\ mg$$

By making 300 mg batches of slurry, the supply of AC electrodes was no limitation. This meant that only electrodes measured to have a mass equivalent to 0.3 mg of active material were used. A rough estimation on the coating thickness for producing AC electrodes with the given capacity was done. Supporting information is displayed in Table 12. This is based on the formula given by:

$$\rho = \frac{m}{V} \rightarrow h_{coating} = \frac{m_{slurry}}{A_{electrode} \cdot \rho_{slurry}}$$

In this equation ρ is the density of the dried AC slurry on top of the electrodes. This was calculated by measuring the mass of previously made AC electrodes and subtracting the current collector mass. The remaining mass was divided by the volume of the slurry, which was the area of the electrode multiplied by the coating height. An average of multiple cells was done to increase accuracy of the density estimate. Furthermore, *m* is the mass of the slurry, *A* is the area of the electrode and *h* is the coating thickness. In the following equation *r* represents the mass ratio of active material in the slurry, which is 80 wt%. Now we can expand the equation given above and plug in the numbers:

$$h_{coating} = \frac{m_{slurry}}{A_{electrode} \cdot \rho_{slurry}} = \frac{r \cdot m_{active}}{A_{15mm} \cdot \rho_{slurry}} = \frac{0.8 \cdot 0.33\ mg}{1.77\ cm^{-2} \cdot 64\ g/cm^{-3}} \approx 33\ \mu m$$

By these calculations, it was decided to make AC electrodes with diameters of 11 mm instead of 15 mm, as the coating would be so thin that the uncertainties would be dominating. Below, the calculations for AC electrodes with 11 mm diameter are done.

$$h_{coating} = \frac{m_{slurry}}{A_{electrode} \cdot \rho_{slurry}} = \frac{r \cdot m_{active}}{A_{11mm} \cdot \rho_{slurry}} = \frac{0.8 \cdot 0.33\ mg}{0.95\ cm^{-2} \cdot 64\ g/cm^{-3}} \approx 63\ \mu m$$

4.2.2.2. Initial full cells

The first full cell being tested was an AC|Si@TiO_2 cell with a TiO_2 thickness of 16 nm, (labeled 16.37 nm). The testing script described in the experimental section under “Initial full cells”. Figure 27 shows the CV curves at different scanning rates. It is difficult to spot the oxidation or reduction peaks in the upper picture, but if we look at the bottom picture in Figure 27 this will show oxidation peaks around 2.1 V. Pay attention to the difference in the values for the current.

Figure 28 shows the GC testing of the cell, performed after the CV measurements. The rate capability test shows the capacity at different currents and the capacity retention after being subjected to high currents. The standard long-term GC measurement will show capacity retention over a longer period with a constant current. The areal capacity is calculated from the area of the electrode, which is 15 mm.

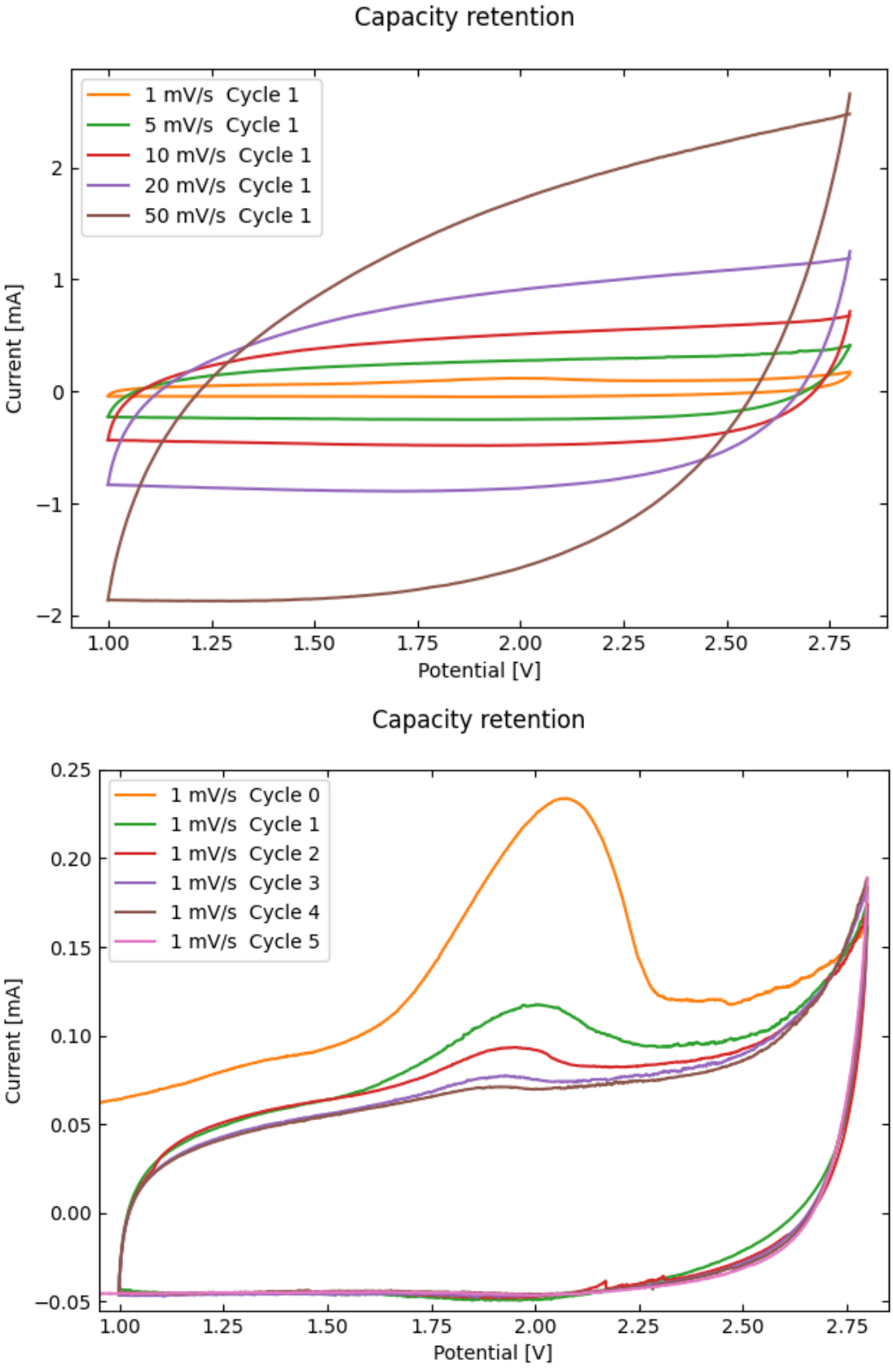

Figure 26: CV measurement of AC|Si@TiO2 full cells in the voltage window of 1.0 – 2.8 V.

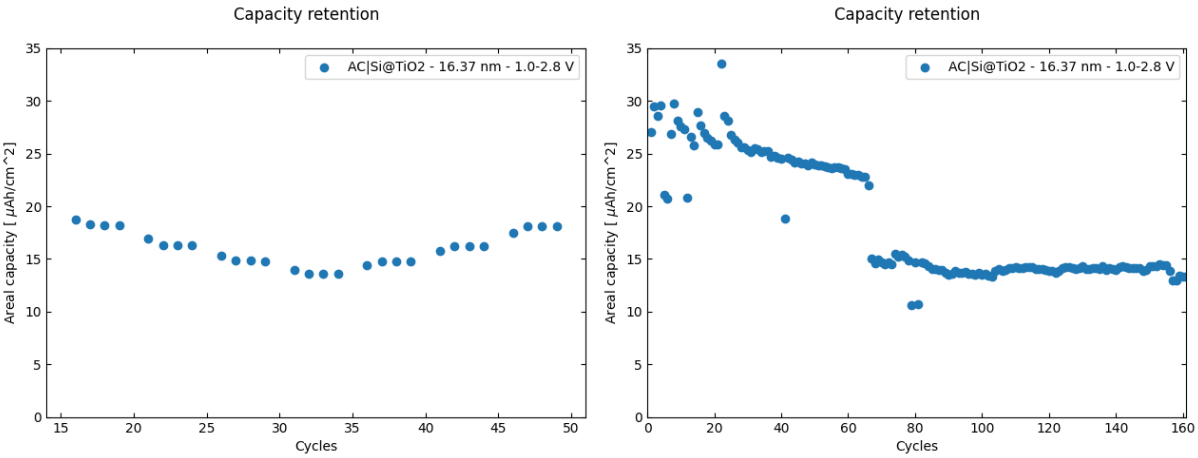

Figure 27: The figure on the left is a rate capability test. The one on right is a constant current GC measurement.

4.2.2.3. CV scans of full cells

In this section we look at the results from the CV measurements of the full cells Figure 29 present the data from AC|Si full cells and Figure 30 presents data from AC|Si@TiO_2 full cells. The upper picture describes the Si|AC full cells that are cycled in the voltage range of 0.1 – 2.8 V. This choice was made to include the oxidation and reduction peaks of Si. Here we can see a small elevation in the positive current curve, from 0.1 V - 1.0 V, on both cycles. Meanwhile, the negative current curve has a similar elevation in opposite direction from about 0.6 - 0.1 V.

The lower picture in Figure 29 shows the results from the Si|AC cells that are identical to the previous picture but has a voltage window that was adjusted to not include the oxidation and reduction peaks of Si. There is no sign of any peak is present in this picture.

Looking at the picture of Figure 30, we notice that all the three initial cycles have different peaks and shapes. The first half cycle, labeled cycle 0, has peaks at roughly 0.6, 0.9, 1.4 and 2.1 V for the samples labeled 4.70 nm, while they are present at 0.6, 0.9 and 2.1 for the 8.18 nm samples. The second cycle shows oxidation peaks at 2.05 V for both as well as some strange behavior between 0.8 and 1.2 V. An additional peak at 1.6 V are showing for samples coated with a 5 nm thick TiO_2 layer. Samples coated with a 8 nm thick TiO_2 layer shows a peak at. No reduction peaks are visible here. The third cycle is for both without any peaks, except for the rounded corners in the experiment.

Again, pay attention to that the y-axis is not equally scaled on the pictures, while the x-axis is. This has been done since the current values of the coated samples are roughly ten times of the uncoated ones. No means of smoothing functions have been applied to the CV curves.

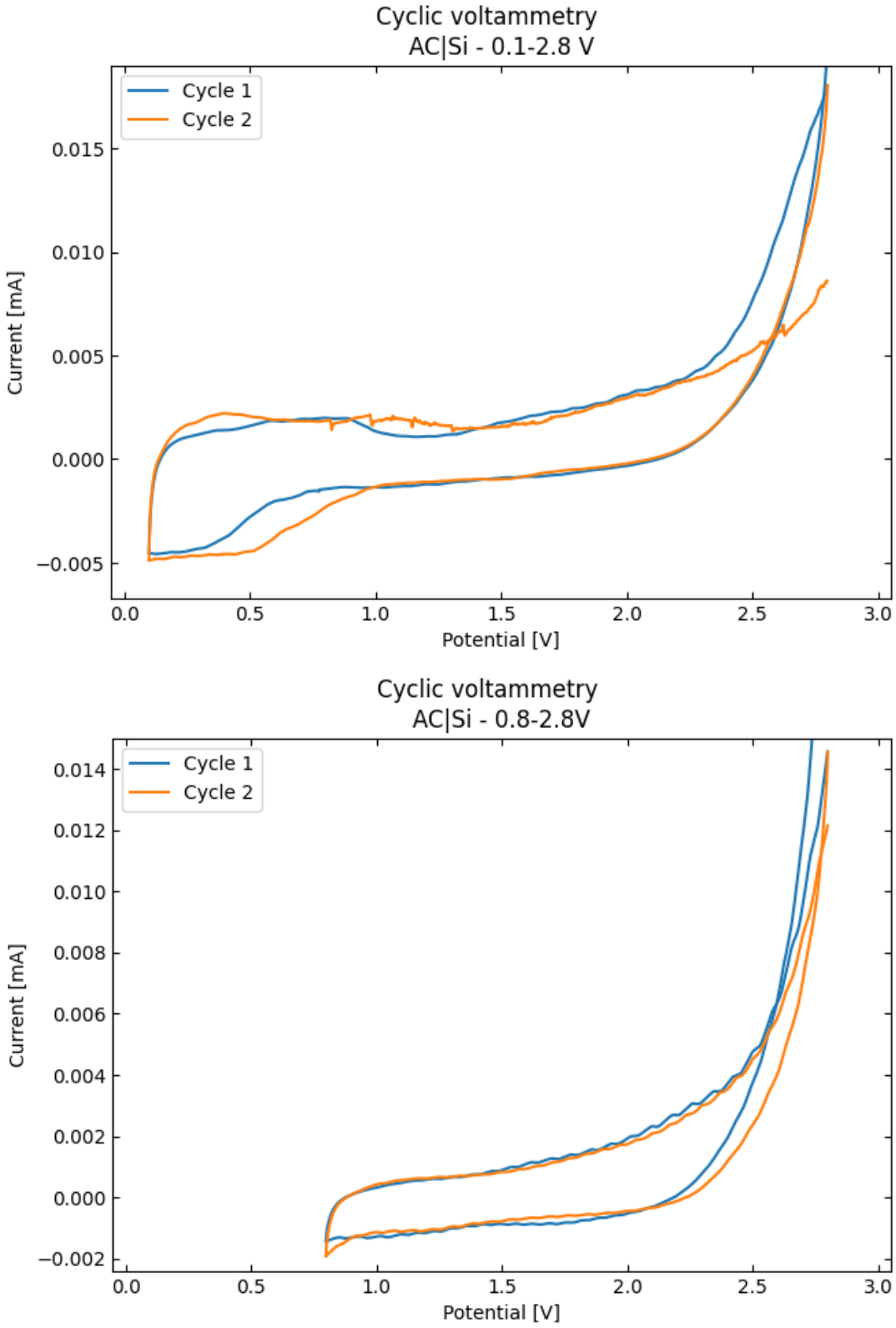

Figure 28: CV comparisons of AC|Si full cells. The top picture is cycled from 0.1 – 2.8 V, while the other one is cycled from 0.8-2.8 V.

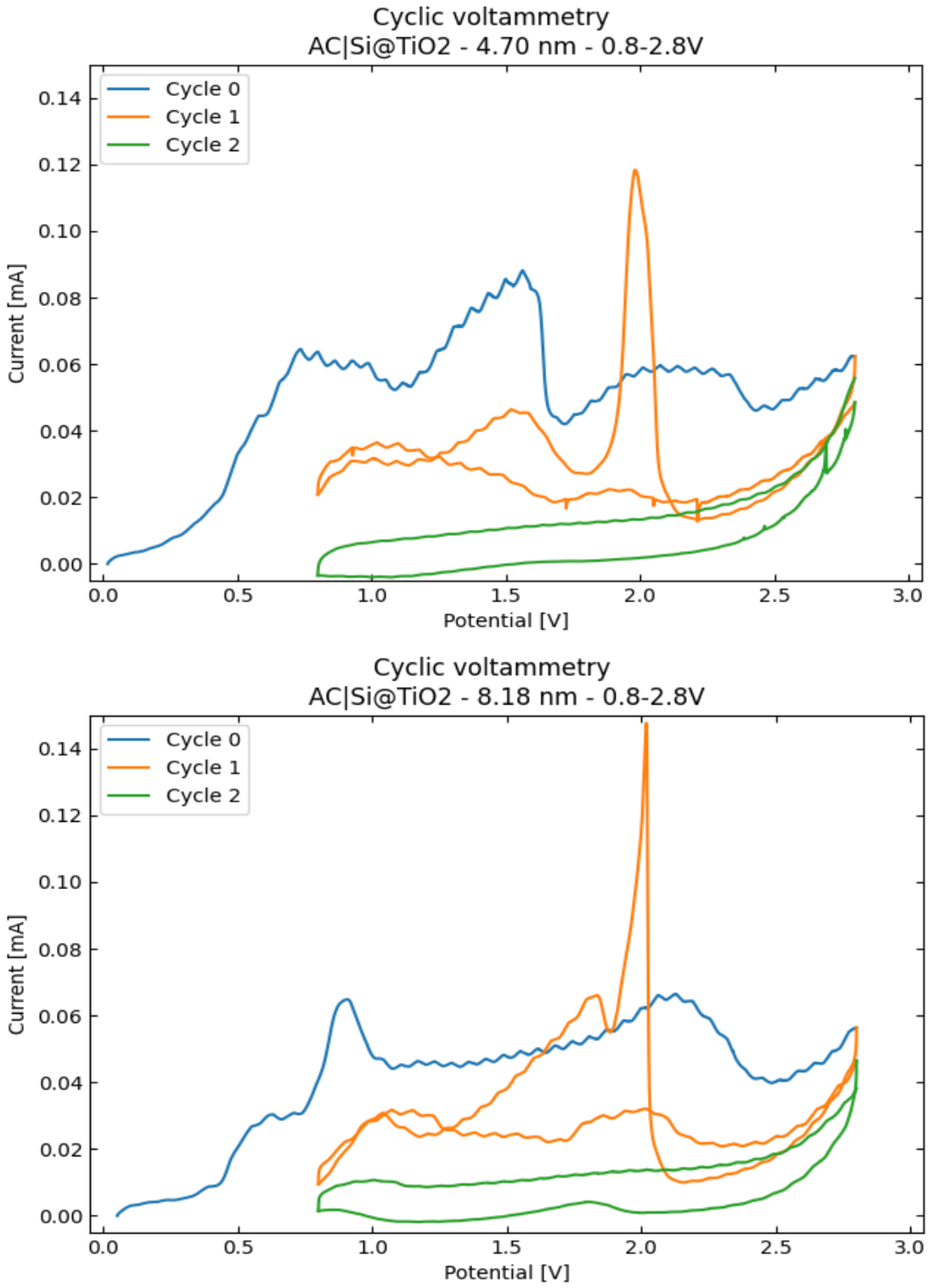

Figure 29: CV comparisons AC|Si@TiO2 full cells. The data are of cells with anodes coated with 5 and 8 nm thick TiO_2 layers, respectively. They are labeled as 4.70 nm and 8.18 nm.

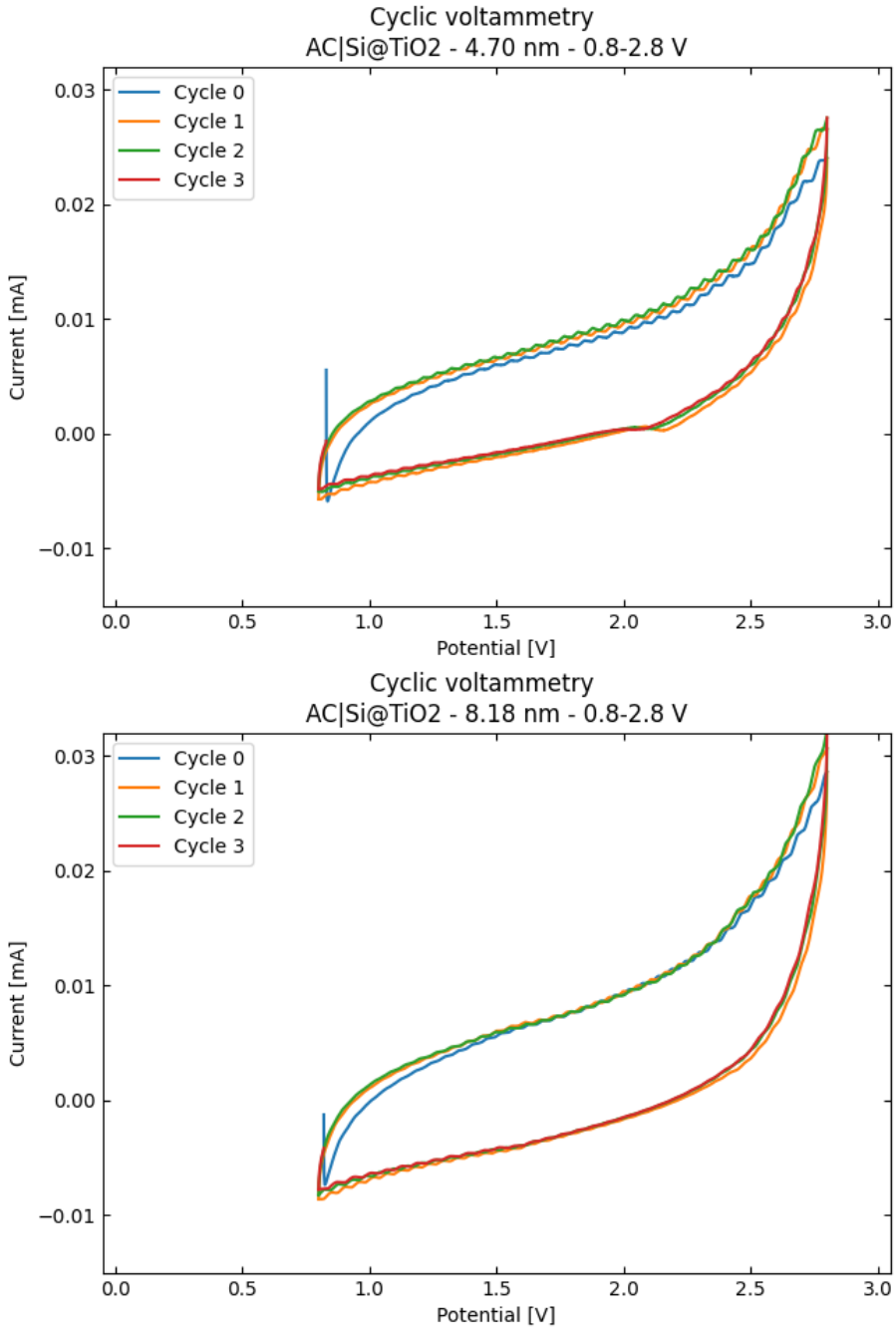

Figure 30: Data from the second set of CV scans for the two AC|Si@TiO2 full cells. This test is performed after the rate capability tests, but before the final long-term cycling.

The data from the second CV scan is presented in Figure 31. The idea behind adding this step to the script, is to run a diagnostic of the cell before and after the rate capability test. This scan is performed after the rate capability tests are done, but before the final long term GC measurements. There are no signs of any oxidation or reduction peaks here and the shape and size of the curves stays somewhat the same through cycling. As excepted, the shape and size of the curves are also similar between the cells, with only a slight increase of curve area for the one with an 8 nm coating.

5. Discussion

In the discussion chapter the results presented in the previous chapter will be compared with each other and other reported results from literature. The discussion chapter will be divided into two parts, where it first will focus on the electrochemical characterization of the cells, while the other part will discuss the synthesis of the coated anodes. Other topics relevant for this project will also be discussed where it is necessary.

5.1. Deposition of titanium oxide

ALD was chosen as the coating technique in this thesis, while there are other techniques being able to produce thin films as well. Some of the techniques generally used for making thin films are discussed in Jilani et al. [66]. It is generally divided into two main sections, being "physical deposition" and "chemical deposition". Only the most relevant techniques described in Jilani et al. will be discussed in this thesis. The normal limitations are connected to the precision connected to produce uniform thin films with thicknesses in the area 2 – 10 nm, while also avoiding damage of the electrode tape. This involves that the substrate should be exposed to temperatures in the area of 20 – 120 °C and ideally as close to room temperature as possible.

The reason why 120 °C was chosen as the temperature, is that it is a compromise between the electrode thermal stability and the temperature window of ALD synthesis from H_2O and $TiCl_4$ precursors. The CMC binder in the electrodes is starting to degrade over 100 °C while the ALD temperature window for coating TiO_2 using H_2O and $TiCl_4$ is from 120 - 230 °C under these conditions,[62]. Furthermore, it is important to discuss the characterization of the TiO_2 coatings on the electrodes. As mentioned before, it is not possible to measure the TiO_2 coating on the porous electrodes directly, but rather on the flat silicon wafers subjected to the same conditions.

Just as a comparison, Suntola's first working semi-ALE reactor had an cycle time of 2 cycles per second translating to 0.5 seconds per cycle, while the DUNE reactor in this thesis uses 254 seconds per cycle,[34]. It is worth noticing that it is an ALE-PVD hybrid reactor and modern physical vapor deposition (PVD) synthesis is reported to produce coatings in the area of 6 µm (6000 nm) in 5 hours,[67]. PVD also requires substantially higher operational temperatures making it unsuitable with the electrodes being used in this thesis.

By compared this to the DUNE reactor producing 5 nm in 15 hours at 120 °C, it becomes clear that the ALD synthesis method is necessarily not the most time efficient method, but for the purpose of this master thesis it is crucial to being able to produce high quality coatings in the area of 3-20 nm at low temperatures.

The GPC of the ALD experiments in this project are somewhat varying. See Table 11 and Table 13. From experience connected to this setup in this project, the most successful coatings have values of GPC around 0.021 - 0.039 nm/cycle. The average GPC for successful ALD experiments in this thesis is at 0.029 nm/cycle. By referring to literature, Desu reports of 0.028 nm/cycle for thin films at 170 °C,[68]. Furthermore, a more relevant article by Yvlivaara et al. reports of 0.0510 nm/cycles for 1924 cycles at a temperature of 110 °C,[69]. The authors point out that there is a linear relationship between the growth and number of cycles, except for when down at 194 ALD cycles. At this point, the GPC is lower than the trend is otherwise. This is relevant to this project as much of the experiments is performed with 200 ALD cycles. Other results close to this is Ritala et al. reporting of 0.042 nm/cycles at 150 °C while Ylilammi et al. reports of 0.054 nm/cycles for 1000 ALD cycles at 150°C,[70] [14]. The GPC in this project is somewhat lower than what is reported in other articles, due to both a small ALD cycle count and temperature. As a final remark, Aarvik reports of a general trend of rougher sample surfaces when the GCP increases,[71].

The most common titanium precursors for ALD synthesis of TiO_2 are according to Meng et al. $Ti(OCH(CH_3)_2)_4$) (TTIP) and $TiCl_4$, while ionized water (H_2O) is the most common oxygen precursor. H_2O_2 has also been reported in literature by Szeghalmi et al. being used as oxygen precursor ,[72]. The article furthermore points to TTIP giving TiO_2 a slightly higher refractive index than $TiCl_4$ would have given. Meng et al. also reports that the TTIP has some advantages versus the use of $TiCl_4$ as titanium precursors,[73]. These advantages are connected to the release of corrosive HCl gas from the $TiCl_4$ synthesis as well as chlorine inside the film.

Traces of Cl^- remnants inside the film has in the SilcRoad project been reported for coating of porous electrodes, using FIB-SEM. The coated electrodes studied in the SilcRoad project was very similar to the electrodes being produced in this thesis and should be further investigated. As mentioned, Meng et al. pointed this out to be a possibility when using $TiCl_4$ as precursor for titanium in the synthesis of TiO_2 thin films. This is unpublished results from an internal project. In the end, the decision to use $TiCl_4$ is due to the fact that TTIP more easily decompose, and in this environment it decomposed in temperature windows too close to the operational temperature of the DUNE reactor,[74].

5.1.1.1. Ellipsometry data

A point needs to be made when it comes to the representation of the data from ellipsometry measurements done in this project. As mentioned before, the measurement is done on a model Si-wafer instead of the Si-electrode itself, so there are some uncertainties connected to the relationship between these values. Furthermore, the measurements are taking three points along the A-substrate Si-wafer, as described in the experimental section. Referring to Table 10 and Table 13, we can see the variations of the measured thicknesses along the same Si-wafer. Despite this, all coatings are presented by two digits in figures and when referring to them. When speaking of the actual coating thickness, a more representative number is being used. This is done to differentiate the samples and is meant as a descriptive label, which do not consider the uncertainties of the measured electrode coating thickness.

5.2. Treatment of electrodes

When taking out electrodes from the reactor it is imperative to cool down the samples as slow as possible using at least two hours with a closed door. It is also important to let the samples “set” after being heat treated over time. This is also true when it comes to drying them in the Büchi oven before inserting them into the glovebox. If this procedure is not followed, the active material is in danger of delaminating from the surface of the cobber current collector.

This occurs when samples are using CMC as binder together with copper current collectors, due to the thermal expansion difference of CMC versus the copper foil. Furthermore, CMC is starting to lose some of its mechanical properties as it is heated, so it is not unproblematic to heat the samples. Some papers report of reduced cycling stability over 100 °C, while others state that 150 °C is the critical point where the CMC starts to “move” and reform in a very unfortunate fashion.

For a long period of time, samples having a 15 nm thick titania (TiO_2) coating was attempted unsuccessfully to be produced using ALD. Samples being treated for too long tended to crumble or detach from the cobber current collector. The reason behind this should be investigated further, but a trend in my experience is that the longer the samples are being subjected to heat, the more mechanically unstable the samples become. It may be related to the CMC, as discussed for the cooling procedure, not being stable at 120 °C and degrading over time. When making a 5 nm thick titania coating the samples are exposed to temperature of 120 °C for around 15 hours, while a 15 nm coating may expose the samples to temperatures of 120 °C for close to 36 hours.

5.3. Discussion on the electrochemical data

5.3.1. Representation of data

The data presented in this project will mainly be given in terms of capacity per area. This area is the planar surface area of the anode, which is 1.767 cm^2. In the field of thin-film batteries it is common to represent the data per surface, rather than per mass unit, as in bulk materials. To illustrate this with an example, the measured capacity of one the Si@TiO_2|Li half cells in this project is on cycle one 334 µAh, while the measured capacity of a Si|Li half-cell is 3628 µAh. The area of these are the same, but while the mass of Si in the electrode can be determined to be 1.2 mg by a weighting scale, the mass of the TiO_2 is not that easy to measure. What is known from our electrode is that the layer is 10 nm thick and on top of an electrode with area of 1.767 cm^2. By using a standard table density of TiO_2 at 4.23 g/cm^3, we can make an estimate of the mass of TiO_2. Using this estimate, we can make the measured capacity to specific and areal capacity for both Si and TiO_2.

Table 11: Comparison of areal and specific capacity of Si and Si@TiO_2 half cells.

Cell	Measured capacity	Areal capacity	Theoretical capacity	Specific Measured capacity
Units	[µAh]	µAh/cm^2	mAh/g	mAh/g
Si|Li	3628	189	~3600	3023
Si@TiO_2|Li	334	2050	~330	12594

Table 11 illustrates in the last two columns the weakness of representing thin-film electrodes by specific capacities. The weakness of an area specific capacity representations is that as soon as the mass increases, the measured capacity will also increase. This means that an increase of mass will always give higher values. The exception that is not representing its data as area capacity, is the bulk materials in this project where the active material is either AC, Si or SiP_x.

5.3.2. Data comparison

By looking at reviews, such as Madian et al., who are comparing the performance of TiO_2 in battery applications, the reported results from various works are varying a lot,[75]. The work most resembling this project was done in 2009 by Cheah et al.,[36]. In this article, 17 nm of TiO_2 was deposited on a 3D Al_2O_3 surface using ALD. As for the reported areal capacity, it was noted to be roughly 13 µAh/cm^2 for 50 cycles at 1 µA in a half cell setup. In comparison, Figure 25, shows a capacity of over 50 µAh/cm^2 for 5000 cycles at 30 µA (17 µA/cm^2) for similar half cells, only with ~8 nm a TiO_2 coating.

Another article by Madian et. al, reports that they achieved a areal capacity of 160 µAh/cm^2 for 100 cycles at 50 µA/cm^2,[17]. Here they build half cells from self-standing TiO_2 nanotubes, claiming that the electric conductivity is the main limiting factor for TiO_2. The solutions they come up with is to go to nanoscale and/or doping/coating with metal oxides or carbon. It is worth mentioning that this synthesis was carried out using ALD but was created using anodic oxidation and thermally annealed at 450 °C in air.

These are just some examples, out of many. In other words, since the electrical conductivity of the TiO_2 is a major limitation for achieving its theoretical capacity, the performance is highly dependent on the size and structure of the anodes. This makes comparisons between different components challenging.

5.3.3. *Half cells*

5.3.3.1. Half cells of Si@TiO_2|Li

In the ideal case, the shape of the pictures in Figure 25 should be similar except for slightly lower values for the capacity in the sample with a 5 nm (labeled 4.76 nm) thick TiO2 coating. This is not the case, as the capacity degradation is significantly higher in the first sample versus the sample coated with a 8 nm (labeled 7.88 nm) TiO2 layer. Furthermore, the first sample also seem to show an initial capacity in the first cycle which is higher than what is shown in all of sample two.

The upper figure of Figure 32 represents the data presented in Figure 25 and compares the specific capacity of the different coating thicknesses. This is meant more as a comparison between the two pictures. The specific capacity of TiO_2 should not be stable over 300 mAh/g, which is shown here, so the lower picture in Figure 32, representing areal capacity of the Si@TiO_2, will be a better comparison. The TiO2@Si|Li half cells having a 5 nm thick coating has a capacity of 13.3 µAh/cm^2 after 5000 cycles, while the ones having a 8 nm thick coating has a capacity of 13.3 µAh/cm^2 after 5000 cycles, both cycled at 34 µAh/cm^2.

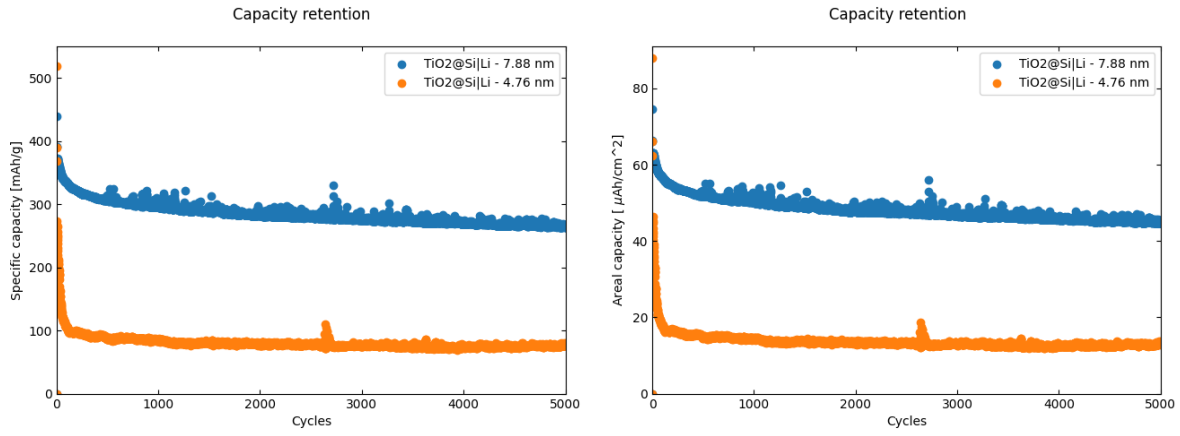

Figure 31: Comparison of the capacity contribution between the samples (labeled 7.88 and 4.76 nm) having 8 and 5 nm thick coatings on Si|TiO_2 electrodes. Shown in both specific and areal capacity

In both pictures we see a significant difference in capacity as the capacity in the electrodes coated with a 8 nm thick TiO_2 layer is around 3.4 times higher than the one coated with a 5 nm coating. This is roughly an 440 % increase in areal capacity by increasing the active material with an estimated 50 %.

5.3.4. CV discussion

In Figure 27 the data from CV measurements of the initial AC|Si@TiO_2 full cells were performed at different scan rates of 1 – 50 mV/s. When looking at the higher scan rates, there are no oxidation peaks, meaning there is no Faradaic charge transfer. The reported shape of this full cell is similar in shape to what is reported by Lai et al.,[7]. This indicates that for high scan rates, and hence high currents, the component works more like a capacitor. However, at 1 mV/s there are visible oxidation peaks indicating redox reactions. These oxidation peaks are decreasing in intensity, meaning that there are a performance limiting process taking place. This can be an irreversible structural change, or it could be related to poor conductivity. By inspecting the shape of the CV curves, it becomes clear that this not an ideal capacitor as the edges is rounded off. An ideal capacitor would have the shape of a perfect rectangle.

When looking at Figure 29, there was no sign of any oxidation peaks in the voltage range of 0.8 – 2.8 V. We may suggest that there are no redox reactions happening, and hence no Faradaic charge transfer. The contribution to capacity from Si is therefore neglectable in this potential window as expected. The shape of the CV curves is of a capacitive nature and is connected to the surface of the component.

Looking at the peak at around 2.02 V for picture Figure 30, it resembles what is reported in Wang et al. as oxidation peaks for anatase TiO_2. The small shift may be due to Wang et al using 0.2 mV/s for scan rate instead of 0.1 mV/s, as well as the size of the coating. Reduction peaks close to 1.7 V are also reported here is not present here,[76]. By comparing this to what was achieved by Cheah et al., we may have an even better comparison. Here they have coated 17 nm of TiO_2 on a porous Al_2O_3 structure, using ALD,[36].

Furthermore, the oxidation peaks present in Figure 30 only appears once, which may suggest that they are connected to a non-reversible process. The total loss of oxidation peaks from cycle two and forth indicates a more pseudocapacitive storage mechanism, as seen in SCs. This could be related to the lack of Li in the system. These peaks are not seen at all in the CV scan performed after the rate capability test, see Figure 31. This supports the claim that these reactions are non-reversible.

The initial peaks in the first half cycle (labeled cycle 0 in Figure 30) may be a formation of SEI on the Si, as the scan goes from 0 – 2.8 V in the first half circle. TiO_2 should according to literature not produce any SEI,[2]. The peaks appearing in the first full cycle (labeled cycle 1 in Figure 30)

In Figure 30 we have included the initial half-cycle which brings the potential from the open circuit voltage (OCV) up to the potential window. The OCV of the cells are measured to be only a couple of mV. This first half cycle passes by the oxidation peaks of Si and we therefore see a peak in this area even for the coated Si@TiO_2 electrodes. This may affect the performance of the cell as the Si structure underneath the TiO_2 coating seems to react and oxidize around 0.6 V. The formation of SEI is mentioned in the prior paragraph and if this is happening, this will irreversible trap some of Li in the system as the cell never goes to the oxidation/reduction potentials of Si again. By referring to literature, there should really be SEI-formation for Si-electrode when increasing the potential from 0 – 2.8 V as is done here,[2].

When it comes to the Si@TiO_2|Li half cells, there are unfortunately no CV measurement presented in this thesis, but a high capacity and capacity retention may indicate Faradaic processes of charge transfer.

5.3.5. Full cells

In Figure 33 a comparison of the specific capacity and capacity retention between different coating thicknesses has been made. Here we can see that the capacity increases significantly with the addition of a TiO_2 coating, and that a coating of 8.18 nm performs better than a coating of 4.70 nm. This could of course be related to the increase in mass the extra nm of film would give, as is pointed out in the "Representing data" section as one of the weaknesses of only giving areal capacities. From the results one can argue that a thicker coating may suggest that a higher areal capacity during the rate capability test.

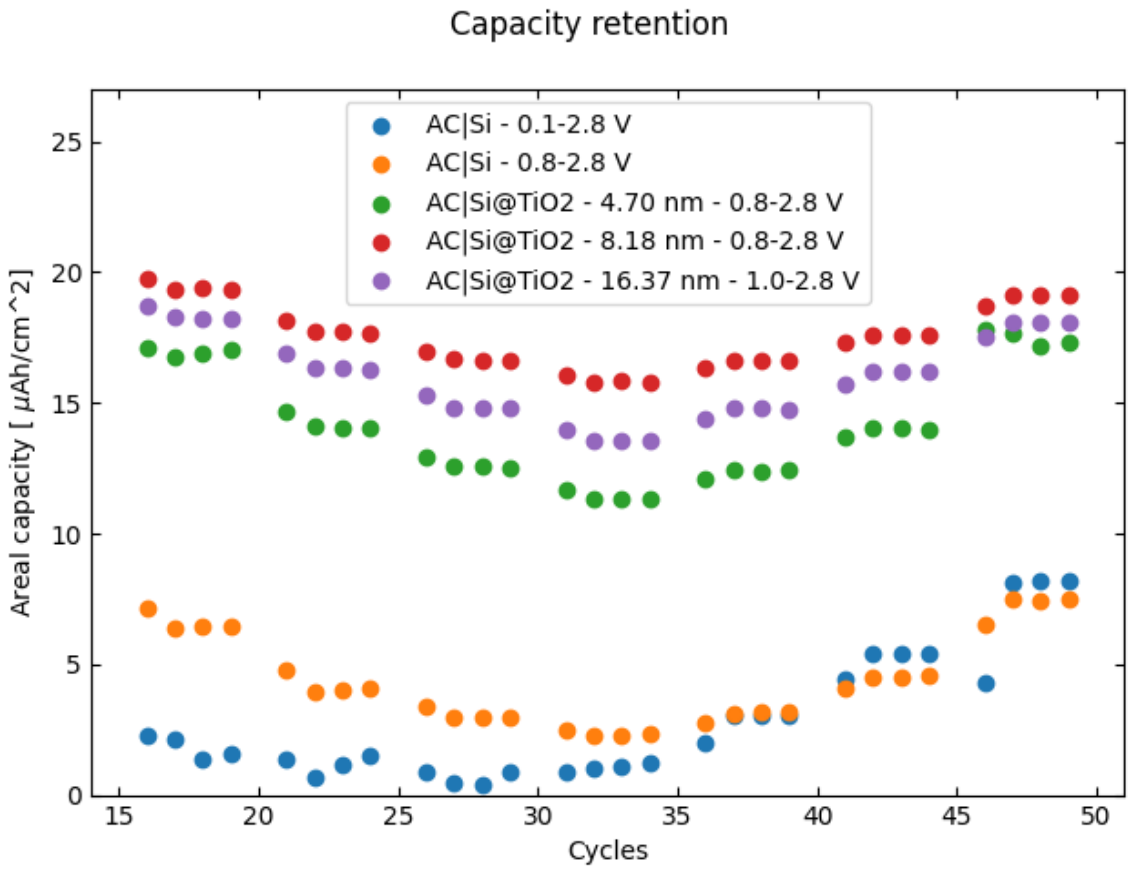

Figure 32: Rate capability comparison between full cells of AC|Si and AC|Si@TiO2 with 5, 8 and 16 nm coatings. The labels are, however, 4.70, 8.18 and 16.37 nm.

With this in mind, the AC|Si@TiO_2 with a 16 nm thick TiO_2 layer should outperform the AC|Si@TiO_2 with a 8 nm (labeled 8.18 nm) thick TiO_2 layer on capacity. The reason why this is not the case, is that these samples were tested in the voltage window of 1.0-2.8 V. It is worth mentioning that the 16 nm samples have twice the activate mass of AC and was tested using a different testing protocol, which is described in detail under "Experimental - Initial full cell tests". Therefore, they should not be compared in terms of numbers, other than to say that testing schedules and voltage windows affect the performance of the cell. From the results of this, it is possible to argue that a larger voltage window will give a larger capacity. What we know from theory is that for an ideal capacitor, the capacitance decreases proportional to the voltage range of the CV scan,[13]. This may indicate that the storage mechanism of the coated full cells is not strictly capacitive.

When moving the focus of study to the samples of AC|Si in the plot, some other interesting effects stats to appear. The capacity and capacity retention of these AC|Si cells are much lower than what is seen for the samples of AC|Si@TiO_2. As the current further increase, the difference in capacity also seems to grow. For the AC|Si cell cycled in the same voltage as the coated ones, this is to be expected as Li should not alloy with Si in this voltage window, as supported by Figure 29. What is more intriguing, is that the samples tested in the voltage window of 0.1 – 2.8 V, has an areal capacity very close to the areal capacity of the other samples of AC|Si.

In other words, even though the voltage window of the test includes the potential values of oxidation and reduction of Si, there is no extra capacity for the component at these current rates. Something else may be the limiting factor in this case.

To help answer if these trends are representative for the full test, the start and end of the rate capability have been shown in Figure 34. These were separated from the results in Figure 33 as they would hide the trends at high currents. Pay attention to the numbers on the y-axis and the large drop in capacity as the current increases when comparing the pictures in Figure 34 with Figure 33. A drop in capacity as the current rises is common, but by doubling the current from 15 µA to 30 µA, the capacity drops from roughly 350 µAh/cm^2 to 70 µAh/cm^2. By an 100 % increase in the current, the capacity is decreased to 20 % of what it was prior to the current change. In comparison, by increasing the current with the same percentage factor from 300 µA to 600 µA, the capacity of the cells decreases to roughly 85 % of the capacity the cells had prior to the current change. This may be due to the poor conductivity of TiO_2.

In Figure 34 we see that the initial capacity of roughly 350 µAh/cm^2 for samples coated with TiO_2 and cycled 0.8 – 2.8 V is preserved though the rate capability test. For high currents we could see in Figure 33 that the samples of 8.18 nm had a higher capacity than what the samples of 4.70 nm had. The samples of 16 nm (labeled 16.37 nm) also had higher capacity than the samples of 4.70 nm. This trend is absent at low currents, where the samples with a 8.2 and 4.7 nm (labeled 8.18 and 4.70 nm) thick coating produces similar capacities, while the samples of 16nm do not show the same increase of capacity.

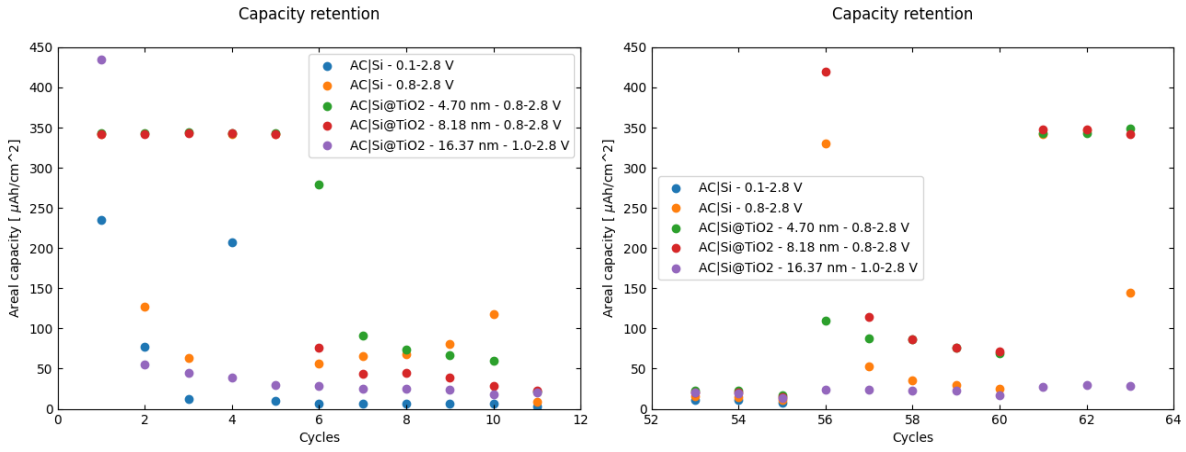

Figure 33: Continuation on the rate capability from Figure 32. Only the start and the end of the test are included. The first five points (1-5) are subjected to the same current as the final ones (61-64).

A high initial capacity for the samples with a 16 nm thick coating (label with 16.37 nm) is seen for the first cycle, before dropping substantially. This may be due to the testing script. At this point we aimed to test the absolute maximum capacity the device could achieve, and a max capacity test was performed in the first cycle, as described in the experimental section.

As mentioned before, the conductivity of TiO_2 is one of the greatest limitations to reaching the theoretical capacity, and hence the formation of the structure is imperative. By studying Figure 33 and Figure 34, there are indications of the thickness of the coating on the samples affecting the conductivity of the samples, as there is an increase in the capacity difference when going to lower currents.

Despite all of this, the proof of concept has been proven - a LIC with a titania anode will work without pre-lithiation.

5.4. Additives

In this project, cells with and without FEC and VC was tested. This was done to evaluate FEC was tested as an additive for symmetric silicon-graphite cells, and silicon-graphite half cells by Ha et al.,[77]. Half cells did, however, not show significant changes as the metallic Li electrode overshadows the behavior of the silicon graphite. Testing at 25, 45 and 70 °C showed that at 70 °C FEC presence increased the parasitic reactions more than the electrolyte without FEC, concluding that FEC is great for low temperatures. FEC additives is by Aurbach et al.[78] said to be the one that improves the passivation of the electrodes at wide temperature ranges the most. This, combined with Ha et al., it may be concluded that FEC is highly beneficial, but the performance increase is less visible at operating temperatures above 70 °C.

It is shown by Kitz et al.,[79], that using FEC and VC as additives in the electrolyte will increase the battery lifetime. The explanation behind this is that the "quality" of the SEI-layer is increased and the initial interphase mass loading is reduced by 30-50 %,[79]. The "quality" of the SEI-layer is by Kitz et al.,[79], defined properties such as electric resistance, thickness, mechanical/thermal stability and so on. Kitz et al. reports that small amounts of VC additive will lead to improved capacity retention, decreased SEI thickness and increased thermal stability of the interphase,[79]. However, since VC is oxidized above 4.3 V vs. Li^+/Li, cells using high-voltage cathodes will experience unfavorable effects on the cell impedance, especially for large amounts of VC. This can be somewhat compensated with the addition of FEC as it stabilizes the electrolyte for high voltage cathode cells. Further down the line, VC is also contributing to increasing the passivation of the SEI-layer on the anode permanently.

6. Conclusion

This project has explored the possibility of engineering a new material for LICs, specifically – titania-coated silicon-based anode. The use of such anode material will not require a pre-lithiation step – a major drawback for the technology at the present moment. The LIC work as a complementary energy storage device to capacitors and batteries in terms of performance.

Atomic layer deposition of TiO_2 on porous Si electrodes proved to be a successful approach to obtain coatings in the order of a few nanometers. The thickness of the coating was determined using ellipsometry measurements on the model systems, where the desired thicknesses were obtained with high precision. To further support this, data obtained through SEM characterization was utilized to characterize the particles and particle-based electrodes used for the present work. SEM showed agglomeration of Si particles and highlights the porous characteristics of the electrodes. Furthermore, it gives estimated particle size of 56 ± 20 nm with a 95 % representation by two population standard deviations. In the present work several thicknesses of TiO2 coating was explored to determine the optimal coating in terms of energy storage capacity and capacity retention during cycling.

Through galvanostatic cycling of half-cells (with Li foil as a counter electrode), the capacity of Si@TiO_2 electrodes with 5 and 8 nm (labeled 4.76 and 7.88 nm) coatings of TiO_2 were measured to be stable at 13.3 and 45.2 µAh/cm^2, after 5000 cycles at 34 µA/cm^2 for both. By performing galvanostatic cycling of AC|Si@TiO_2 full cells, we discovered that coatings of 5 and 8 nm (labeled 4.70 and 8.18 nm) are showing a capacity of 350 µAh/cm^2 at currents of 17 µA/cm^2, while they are dropping to around 50 µAh/cm^2 at currents of 34 µA/cm^2. The samples stabilized around 15 µAh/cm^2 for currents of 340 µA/cm^2. Furthermore, there are no capacity degradation after the rate capability test of the full cells, indicating a high capacity retention.

For samples having a 16 nm thick TiO_2 coating, the initial capacity is preserved through rate capability tests, but remains at a capacity value of roughly 30 µAh/cm^2. Due to the difference in testing schedules, a definite answer whether this is connected to the coating cannot be verified here. When comparing these with the AC|Si full cells, cycled in the different voltage windows already mentioned, AC|Si@TiO_2 had 2 – 3 times the capacity of the AC|Si at high voltages (85 – 340 µA/cm^2). For low currents of 17 µA/cm^2, the samples of AC|Si shows similar values of capacity as the AC|Si@TiO_2 full cell with a 16 nm thick TiO_2 coating.

With the use of cyclic voltammetry, the means of storage was determined for both half cells and full cells fabricated in this project. The first half cells of Si|Li have Faradaic charge transfer through redox reactions, as is known for LIBs. For the full cells of AC|Si@TiO_2 they initial Faradaic charge transfer through redox reactions before shifting to pseudocapacitive mechanisms as known for SCs. It was argued that this was because of conductivity problems.

Through the course of the present work, we have proven that titania coated silicon anodes does not require pre-lithiation, while the LIC can still function over the course of many cycles with excellent capacity retention. That proves the original hypothesis that anodes for LIC could be designed in a way completely different from the approach currently adopted in the field.

7. Future work

For future work, it could be beneficial to coat particles or thin films on more conductive surfaces, as they seem to show more promise based on the literature. One of the issues is that Si should not be electrochemically active to ensure high capacity retention. The compromise to lower all synthesis temperatures to ensure the survival of the Si anode also limits the possibility to heat treating the sample later. An XRD of the materials should also be included since it is important to determine the TiO_2 structure in order to understand the behavior during cycling. EDX characterization should also have been performed to map the elements in the given areas of the electrodes.

CV measurements of Si@TiO_2|Li half cells should also have been performed to obtain information on the storage mechanisms in these cells. Furthermore, the measurements performed at the full cells are both CV, rate capability and long-term GC measurements on the same cells. This may affect the results negatively as it puts the cells through a lot of degradation before the long-term cycling starts, and the experiments should ideally be performed on different cells to give more comparable results to other articles.

8. Appendix

8.1. AC slurry density calculations

Table 12: Calculation of average density of AC slurry.

Cell ID	Mass of electrode	Mass per electrode	Active mass per electrode
Units	**mg**	**mg**	**mg**
1	8.9	1.8	1.44
2	8.6	1.5	1.20
3	9.3	2.2	1.76
4	9.6	2.5	2.00
5	9.5	2.4	1.92
Ideal cell	7.5	0.42	0.33
Average	9.2	2.1	1.66

Active mass per area	Estimated density of slurry	Estimated coating thickness for 15 mm electrodes	Estimated coating thickness for 11 mm electrodes
mg/cm^2	**mg/cm^3**	**µm**	**µm**
0.82	60	147	274
0.68	50	123	228
1.00	73	180	334
1.13	83	204	380
1.09	80	196	365
0.19	14	34	63
0.94	**69**	170	316

8.2. ALD supporting spread sheet

Table 13: Table showing additional info on ALD samples measured by ellipsometry.

Run info	Sample ID	TiO_2 film thickness [nm]	PC thickness [nm]	Total Film thickness [nm]	C-substrate gradient [nm]	C-substrate second derivative [nm]
MR5009	A1	5.32	1.60	6.92		
20.10.2021	A2	5.37	1.60	6.97		
Cyc =	A3	5.70	1.60	7.30		
200	C1	3.51	1.60	5.11	-0.73	1.01
	C2	2.78	1.60	4.38	0.28	1.85
For all runs:	C3	3.06	1.60	4.66	2.13	-0.08
$TiCl_4 + H_2O$	C4	5.19	1.60	6.79	2.05	0.55
T = 120 Celsius	C5	7.24	1.60	8.84	2.60	-4.40
	C6	9.84	1.60	11.44	-1.80	
	C7	8.04	1.60	9.64		
MR5010	A2	3.68	1.60	5.28		
20.10.2021	A2.5	3.77	1.60	5.37		
Cyc =	A3	4.54	1.60	6.14		
200	C1	2.21	1.60	3.81	0.41	0.44
	C2	2.62	1.60	4.22	0.85	0.33
	C3	3.47	1.60	5.07	1.18	-1.69
	C4	4.65	1.60	6.25	-0.51	0.23
	C5	4.14	1.60	5.74	-0.28	0.79
	C6	3.86	1.60	5.46	0.51	
	C7	4.37	1.60	5.97		
MR5011	A1	6.45	1.60	8.05		
03.11.2021	A2	6.88	1.60	8.48		
Cyc =	A3	6.59	1.60	8.19		
200	C1	5.38	1.60	6.98	-3.20	4.70
	C2	2.18	1.60	3.78	1.50	1.16
	C3	3.68	1.60	5.28	2.66	-0.23
	C4	6.34	1.60	7.94	2.43	0.85
	C5	8.77	1.60	10.37	3.28	9.65
	C6	12.05	1.60	13.65	12.93	
	C7	24.98	1.60	26.58		

MR5012	A1	7.70	1.60	9.30		
12.11.2021	A2	9.26	1.60	10.86		
Cyc =	A3	6.96	1.60	8.56		
200	C1	7.55	1.60	9.15	-5.48	9.62
	C2	2.07	1.60	3.67	4.14	-1.70
	C3	6.21	1.60	7.81	2.44	-0.42
	C4	8.65	1.60	10.25	2.02	0.18
	C5	10.67	1.60	12.27	2.20	-4.88
	C6	12.87	1.60	14.47	-2.68	
	C7	10.19	1.60	11.79		
MR5013	A1	10.38	1.60	11.98		
13.11.2021	A2	11.09	1.60	12.69		
Cyc =	A3	10.79	1.60	12.39		
285						
MR5014	A1	12.44	1.60	14.04		
15.11.2021	A2	13.64	1.60	15.24		
Cyc =	A3	12.90	1.60	14.50		
353						
MR5015	A1	222.51	1.49	224.00		
16.11.2021	A2	309.22	1.78	311.00		
Cyc =	A3	200.11	1.89	202.00		
407						
MR5016	A1.5	23.52	1.62	25.14		
18.11.2021	A2	24.80	1.47	26.27		
Cyc =	A2.5	23.91	2.14	26.05		
353						
MR5017	A1	20.39	1.60	21.99		
19.11.2021	A2	24.23	1.60	25.83		
Cyc =	A3	17.45	1.60	19.05		
216						
MR5018	A1	8.77	1.64	10.41		
20.11.2021	A2	11.73	1.63	13.36		
Cyc =	A3	7.84	2.03	9.87		
132						
MR5019	A1	20.33	1.60	21.93		
24.11.2021	A2	28.82	1.60	30.42		
Cyc =	A3	15.92	1.60	17.52		
169						

MR5020	A1	7.11	1.60	8.71		
25.11.2021	A2	8.69	1.60	10.29		
Cyc =	A3	7.68	1.60	9.28		
145	C1	3.78	1.60	5.38	-1.78	3.22
	C2	2.00	1.60	3.60	1.44	1.37
	C3	3.44	1.60	5.04	2.81	-0.05
	C4	6.25	1.60	7.85	2.76	0.71
	C5	9.01	1.60	10.61	3.47	-1.42
	C6	12.48	1.60	14.08	2.05	
	C7	14.53	1.60	16.13		
MR5021	A1	6.35	1.73	8.08		
29.11.2021	A2	8.67	1.70	10.37		
Cyc =	A3	8.26	1.80	10.06		
185	C1	2.09	1.63	3.72	0.09	1.98
	C2	2.18	1.62	3.80	2.07	-0.19
	C3	4.25	1.60	5.85	1.88	-1.36
	C4	6.13	1.63	7.76	0.52	1.09
	C5	6.65	1.56	8.21	1.61	-1.25
	C6	8.26	1.59	9.85	0.36	
	C7	8.62	1.78	10.40		
MR5022	A1	12.69	1.91	14.60		
10.12.2022	A2	19.47	1.95	21.42		
Cyc =	A3	9.98	2.06	12.04		
238	C1	4.40	1.73	6.13	15.31	-30.93
	C2	19.71	1.71	21.42	-15.62	15.38
	C3	4.09	1.70	5.79	-0.24	0.01
	C4	3.85	1.72	5.57	-0.23	1.26
	C5	3.62	1.89	5.51	1.03	0.64
	C6	4.65	1.90	6.55	1.67	
	C7	6.32	2.04	8.36		
MR5023	A1	14.57	1.60	16.17		
14.12.2022	A2	26.60	1.60	28.20		
Cyc =	A3	12.01	1.60	13.61		
200	C1	2.63	1.60	4.23	-0.16	0.77
	C2	2.47	1.60	4.07	0.61	0.03
	C3	3.08	1.60	4.68	0.64	-0.40
	C4	3.72	1.60	5.32	0.24	0.53
	C5	3.96	1.60	5.56	0.77	0.61
	C6	4.73	1.60	6.33	1.38	
	C7	6.11	1.60	7.71		

MR5024	A1	19.80	1.37	21.17		
01.02.2022	A2	23.25	1.65	24.90		
Cyc =	A3	5.85	2.02	7.87		
200	C1	-1.19	3.83	2.64	1.40	1.22
	C2	0.21	2.28	2.49	2.62	6.48
	C3	2.83	2.45	5.28	9.10	-6.46
	C4	11.93	2.62	14.55	2.64	-3.74
	C5	14.57	1.93	16.50	-1.10	3.70
	C6	13.47	1.71	15.18	2.60	
	C7	16.07	2.00	18.07		
MR5025	A1	5.46	1.49	6.95		
02.02.2022	A2	4.70	1.62	6.32		
Cyc =	A3	5.63	1.84	7.47		
140	C1	1.84	1.76	3.60	1.15	-0.26
	C2	2.99	1.67	4.66	0.89	-1.50
	C3	3.88	1.96	5.84	-0.61	-0.21
	C4	3.27	2.03	5.30	-0.82	1.80
	C5	2.45	1.90	4.35	0.98	-0.18
	C6	3.43	1.77	5.20	0.80	
	C7	4.23	2.36	6.59		
MR5026	A1	3.58	1.67	5.25		
04.02.2022	A2	20.45	1.99	22.44		
Cyc =	A3	44.70	1.90	46.60		
160	C1	2.73	1.74	4.47	-0.93	1.30
	C2	1.80	1.72	3.52	0.37	0.07
	C3	2.17	2.26	4.43	0.44	0.47
	C4	2.61	2.09	4.70	0.91	-1.24
	C5	3.52	2.10	5.62	-0.33	0.30
	C6	3.19	2.52	5.71	-0.03	
	C7	3.16	2.46	5.62		
MR5027	A1	5.62	1.49	7.11		
06.02.2022	A2	9.56	1.55	11.11		
Cyc =	A3	6.08	1.78	7.86		
160	C1	1.31	1.76	3.07	-0.13	0.48
	C2	1.18	1.66	2.84	0.35	0.05
	C3	1.53	1.75	3.28	0.40	-0.09
	C4	1.93	1.64	3.57	0.31	0.16
	C5	2.24	1.67	3.91	0.47	-0.62
	C6	2.71	1.83	4.54	-0.15	
	C7	2.56	2.10	4.66		

MR5028	A1	6.04	1.81	7.85		
07.02.2022	A2	7.80	2.28	10.08		
Cyc =	A3	6.47	2.44	8.91		
180	C1	0.91	1.60	2.51	0.17	0.15
	C2	1.08	1.54	2.62	0.32	0.31
	C3	1.40	1.53	2.93	0.63	0.14
	C4	2.03	1.58	3.61	0.77	0.22
	C5	2.80	1.58	4.38	0.99	0.42
	C6	3.79	1.59	5.38	1.41	
	C7	5.20	1.90	7.10		
MR5029	A1	6.86	1.66	8.52		
08.02.2022	A2	8.85	1.49	10.34		
Cyc =	A3	7.48	1.63	9.11		
220	C1	0.95	1.96	2.91	0.81	-1.05
	C2	1.76	1.98	3.74	-0.24	1.79
	C3	1.52	1.92	3.44	1.55	-0.77
	C4	3.07	1.75	4.82	0.78	0.36
	C5	3.85	1.70	5.55	1.14	0.19
	C6	4.99	1.69	6.68	1.33	
	C7	6.32	1.79	8.11		
MR5030	A1	8.22	2.27	10.49		
09.02.2022	A2	13.94	2.05	15.99		
Cyc =	A3	13.58	1.66	15.24		
285	C1	1.19	1.61	2.80	-0.03	0.39
	C2	1.16	1.57	2.73	0.36	0.12
	C3	1.52	1.50	3.02	0.48	0.51
	C4	2.00	1.60	3.60	0.99	0.86
	C5	2.99	1.77	4.76	1.85	-0.23
	C6	4.84	1.70	6.54	1.62	
	C7	6.46	1.81	8.27		
MR5031	A1	8.69	1.60	10.29		
22.02.2022	A2	10.11	1.60	11.71		
Cyc =	A3	9.82	1.60	11.42		
310	C1	2.88	1.60	4.48	0.85	0.68
	C2	3.73	1.60	5.33	1.53	-0.20
	C3	5.26	1.60	6.86	1.33	-0.27
	C4	6.59	1.60	8.19	1.06	0.15
	C5	7.65	1.60	9.25	1.21	2.76
	C6	8.86	1.60	10.46	3.97	
	C7	12.83	1.60	14.43		

MR5032	A1	8.72	1.71	10.43		
23.02.2022	A2	9.88	1.53	11.41		
Cyc =	A3	11.61	1.60	13.21		
310	C1	1.72	1.62	3.34	-0.96	2.94
	C2	0.76	2.13	2.89	1.98	-1.27
	C3	2.74	1.58	4.32	0.71	-0.99
	C4	3.45	1.70	5.15	-0.28	1.61
	C5	3.17	1.76	4.93	1.33	0.07
	C6	4.50	1.71	6.21	1.40	
	C7	5.90	1.99	7.89		
MR5033	A1	0.00	1.60	1.60		
25.02.2022	A2	0.00	1.60	1.60		
Cyc =	A3	0.00	1.60	1.60		
310	C1	0.00	1.60	1.60	0.00	0.00
Dry deposition	C2	0.00	1.60	1.60	0.00	0.00
	C3	0.00	1.60	1.60	0.00	0.00
	C4	0.00	1.60	1.60	0.00	0.00
	C5	0.00	1.60	1.60	0.00	0.00
	C6	0.00	1.60	1.60	0.00	
	C7	0.00	1.60	1.60		
MR5034	A1	2.87	1.47	4.34		
02.03.2022	A2	3.24	1.42	4.66		
Cyc =	A3	2.99	1.53	4.52		
140	C1	0.60	2.11	2.71	0.15	-0.05
	C2	0.75	1.98	2.73	0.10	0.51
	C3	0.85	2.07	2.92	0.61	-0.22
	C4	1.46	1.55	3.01	0.39	-0.12
	C5	1.85	1.43	3.28	0.27	0.08
	C6	2.12	1.47	3.59	0.35	
	C7	2.47	1.46	3.93		
MR5035	A1	4.95	1.46	6.41		
03.03.2022	A2	5.09	1.43	6.52		
Cyc =	A3	4.58	1.66	6.24		
200	C1	0.86	1.69	2.55	0.22	0.14
	C2	1.08	1.51	2.59	0.36	-0.07
	C3	1.44	1.51	2.95	0.29	0.41
	C4	1.73	1.50	3.23	0.70	0.55
	C5	2.43	1.45	3.88	1.25	0.04
	C6	3.68	1.44	5.12	1.29	
	C7	4.97	1.48	6.45		

MR5036	A1	7.91	1.73	9.64		
14.03.2022	A2	8.65	1.51	10.16		
Cyc =	A3	6.54	1.63	8.17		
205	C1	3.18	1.99	5.17	1.65	-1.11
	C2	4.83	2.26	7.09	0.54	-1.81
	C3	5.37	3.21	8.58	-1.27	2.96
	C4	4.10	4.10	8.20	1.69	-0.67
	C5	5.79	3.21	9.00	1.02	1.61
	C6	6.81	3.33	10.14	2.63	
	C7	9.44	2.35	11.79		
MR5037	A1	9.04	1.37	10.41		
15.03.2022	A2	9.43	1.42	10.85		
Cyc =	A3	9.55	1.45	11.00		
310	C1	1.29	1.47	2.76	3.12	-3.64
	C2	4.41	1.46	5.87	-0.52	0.40
	C3	3.89	1.49	5.38	-0.12	0.36
	C4	3.77	1.52	5.29	0.24	1.56
	C5	4.01	1.45	5.46	1.80	0.48
	C6	5.81	1.42	7.23	2.28	
	C7	8.09	1.43	9.52		
MR5038	A1	9.03	2.18	11.21		
16.03.2022	A2	8.77	2.48	11.25		
Cyc =	A3	8.99	2.13	11.12		
330	C1	1.29	1.70	2.99	1.23	-0.91
	C2	2.52	2.01	4.53	0.32	0.70
	C3	2.84	1.88	4.72	1.02	-0.16
	C4	3.86	1.84	5.70	0.86	-0.03
	C5	4.72	2.56	7.28	0.83	-1.13
	C6	5.55	3.25	8.80	-0.30	
	C7	5.25	3.03	8.28		
MR5039	A1	7.17	1.45	8.62		
17.03.2022	A2	8.37	1.43	9.80		
Cyc =	A3	6.43	1.60	8.03		
205	C1	2.04	0.14	2.18	-0.92	1.06
	C2	1.12	1.42	2.54	0.14	0.51
	C3	1.26	1.46	2.72	0.65	0.30
	C4	1.91	1.46	3.37	0.95	0.14
	C5	2.86	1.48	4.34	1.09	0.15
	C6	3.95	1.48	5.43	1.24	
	C7	5.19	1.53	6.72		

MR5040	A1	7.44	2.28	9.72		
22.03.2022	A2	8.75	2.50	11.25		
Cyc =	A3	7.45	2.30	9.75		
205	C1	4.85	1.93	6.78	0.75	-0.95
	C2	5.60	1.86	7.46	-0.20	-0.81
	C3	5.40	1.95	7.35	-1.01	1.24
	C4	4.39	2.11	6.50	0.23	1.30
	C5	4.62	2.71	7.33	1.53	-1.14
	C6	6.15	1.92	8.07	0.39	
	C7	6.54	1.63	8.17		
MR5041	A1	4.68	1.88	6.56		
23.03.2022	A2	5.19	1.53	6.72		
Cyc =	A3	4.40	1.52	5.92		
205	C1	2.95	1.86	4.81	-0.57	0.55
	C2	2.38	1.71	4.09	-0.02	0.03
	C3	2.36	1.68	4.04	0.01	0.41
	C4	2.37	1.68	4.05	0.42	0.03
	C5	2.79	1.60	4.39	0.45	0.26
	C6	3.24	1.59	4.83	0.71	
	C7	3.95	1.53	5.48		
MR5042	A1	7.74	2.37	10.11		
24.03.2022	A2	9.28	2.13	11.41		
Cyc =	A3	8.04	2.77	10.81		
310	C1	2.67	1.51	4.18	-0.42	0.36
	C2	2.25	1.47	3.72	-0.06	0.38
	C3	2.19	1.48	3.67	0.32	0.16
	C4	2.51	1.46	3.97	0.48	0.74
	C5	2.99	1.48	4.47	1.22	0.20
	C6	4.21	1.46	5.67	1.42	
	C7	5.63	1.61	7.24		
MR5043	A1	8.52	1.93	10.45		
25.03.2022	A2	9.44	1.56	11.00		
Cyc =	A3	8.19	1.59	9.78		
405	C1	1.92	1.82	3.74	-0.23	0.76
	C2	1.69	1.86	3.55	0.53	0.10
	C3	2.22	1.61	3.83	0.63	0.55
	C4	2.85	1.68	4.53	1.18	0.42
	C5	4.03	1.75	5.78	1.60	-1.41
	C6	5.63	1.77	7.40	0.19	
	C7	5.82	1.89	7.71		

MR5044	A1	7.67	1.61	9.28		
21.04.2022	A2	8.70	1.57	10.27		
Cyc =	A3	8.17	1.60	9.77		
215	C1	4.62	1.82	6.44	0.12	0.64
	C2	4.74	1.86	6.60	0.76	-0.45
	C3	5.50	1.61	7.11	0.31	-0.38
	C4	5.81	1.68	7.49	-0.07	3.93
	C5	5.74	1.75	7.49	3.86	-1.92
	C6	9.60	1.77	11.37	1.94	
	C7	11.54	1.89	13.43		
MR5045	A1	13.71	2.39	15.32		
23.04.2022	A2	18.90	2.22	20.47		
Cyc =	A3	16.50	3.86	18.10		
197	C1	3.30	2.09	5.12	0.94	-1.53
	C2	4.24	2.09	6.10	-0.59	0.01
	C3	3.65	1.95	5.26	-0.58	0.82
	C4	3.07	1.80	4.75	0.24	2.80
	C5	3.31	1.79	5.06	3.04	-0.33
	C6	6.35	1.71	8.12	2.71	
	C7	9.06	2.51	10.95		
MR5046	A1	4.11	1.55	5.66		
25.04.2022	A2	5.15	1.52	6.67		
Cyc =	A3	3.93	1.58	5.51		
160	C1	1.47	1.55	3.02	0.43	-0.34
	C2	1.90	1.48	3.38	0.09	0.02
	C3	1.99	1.49	3.48	0.11	0.14
	C4	2.10	1.48	3.58	0.25	0.06
	C5	2.35	1.53	3.88	0.31	0.15
	C6	2.66	1.55	4.21	0.46	
	C7	3.12	1.62	4.74		
MR5047	A1	3.30	1.58	4.88		
26.04.2022	A2	3.51	1.66	5.17		
Cyc =	A3	3.15	1.51	4.66		
170	C1	3.47	1.63	5.10	-0.71	1.82
	C2	2.76	1.53	4.29	1.11	-1.76
	C3	3.87	1.57	5.44	-0.65	-0.08
	C4	3.22	1.54	4.76	-0.73	1.13
	C5	2.49	1.55	4.04	0.40	-0.29
	C6	2.89	1.59	4.48	0.11	
	C7	3.00	1.85	4.85		

MR5048	A1	4.56	1.55	6.11		
28.04.2022	A2	5.05	1.43	6.48		
Cyc =	A3	4.48	1.55	6.03		
205	C1	1.09	1.41	2.50	1.11	-0.33
	C2	2.20	1.51	3.71	0.78	-1.40
	C3	2.98	1.64	4.62	-0.62	1.16
	C4	2.36	1.68	4.04	0.54	0.22
	C5	2.90	1.87	4.77	0.76	0.21
	C6	3.66	1.80	5.46	0.97	
	C7	4.63	2.14	6.77		
MR5049	A1	4.32	1.63	5.95		
29.04.2022	A2	4.98	1.62	6.60		
Cyc =	A3	4.88	1.68	6.56		
215	C1	1.53	1.77	3.30	0.64	-0.46
	C2	2.17	1.62	3.79	0.18	-0.29
	C3	2.35	1.68	4.03	-0.11	0.37
	C4	2.24	1.71	3.95	0.26	0.21
	C5	2.50	1.86	4.36	0.47	-0.36
	C6	2.97	2.28	5.25	0.11	
	C7	3.08	3.32	6.40		
MR5050	A1	6.16	1.55	7.71		
30.04.2022	A2	7.12	1.69	8.81		
Cycles =	A3	6.11	1.51	7.62		
300	C1	0.96	1.54	2.50	0.39	-0.18
	C2	1.35	1.51	2.86	0.21	0.11
	C3	1.56	1.52	3.08	0.32	0.37
	C4	1.88	1.51	3.39	0.69	0.18
	C5	2.57	1.42	3.99	0.87	-0.01
	C6	3.44	1.44	4.88	0.86	
	C7	4.30	1.83	6.13		

9. References

(1) Abdullah, A.; Mohammed, A. Scanning Electron Microscopy (SEM): A Review. **2019**.

(2) Korthauer, R. *Lithium-Ion Batteries: Basics and Applications*; 2018. DOI: 10.1007/978-3-662-53071-9.

(3) Aarik, J.; Karlis, J.; Mändar, H.; Uustare, T.; Sammelselg, V. Influence of structure development on atomic layer deposition of TiO2 thin films. *Applied Surface Science* **2001**, *181* (3-4), 339-348. DOI: 10.1016/s0169-4332(01)00430-5.

(4) Nowak, S.; Winter, M. The Role of Sub- and Supercritical CO2 as "Processing Solvent" for the Recycling and Sample Preparation of Lithium Ion Battery Electrolytes. *Molecules* **2017**, *22* (3), 403. DOI: 10.3390/molecules22030403.

(5) Brennhagen, A. Synthesis and electrochemical characterization

of thin film iron phosphates as cathode material

for Li-ion batteries. University of Oslo, DUO, 2019. https://www.duo.uio.no/handle/10852/70523 (accessed 24.01.2022).

(6) YassineMrabet. Basic Diagram of a Fluidized Bed Reactor. Wikimedia Commons: Wikipedia, 2009; pp {{Information |Description={{en|1=Basic Diagram of a Fluidized Bed Reactor}} |Source={{own}} bazed on raster version |Author={{User:YassineMrabet/mysign}} {{inkscape}} |Date=2009-2010-2027 |Permission=PD (see below).

(7) Lai, S. Y.; Cavallo, C.; Abdelhamid, M. E.; Lou, F.; Koposov, A. Y. Advanced and Emerging Negative Electrodes for Li-Ion Capacitors: Pragmatism vs. Performance. *Energies* **2021**, *14* (11), 3010. DOI: 10.3390/en14113010.

(8) Lukatskaya, M. R.; Dunn, B.; Gogotsi, Y. Multidimensional materials and device architectures for future hybrid energy storage. *Nature Communications* **2016**, *7* (1), 12647. DOI: 10.1038/ncomms12647.

(9) Michan, A. L.; Parimalam, B. S.; Leskes, M.; Kerber, R. N.; Yoon, T.; Grey, C. P.; Lucht, B. L. Fluoroethylene Carbonate and Vinylene Carbonate Reduction: Understanding Lithium-Ion Battery Electrolyte Additives and Solid Electrolyte Interphase Formation. *Chemistry of Materials* **2016**, *28* (22), 8149-8159. DOI: 10.1021/acs.chemmater.6b02282.

(10) Sohani, A.; Sayyaadi, H. Providing an accurate method for obtaining the efficiency of a photovoltaic solar module. *Renewable Energy* **2020**, *156*, 395-406. DOI: 10.1016/j.renene.2020.04.072.

(11) Soman, S. S.; Zareipour, H.; Malik, O.; Mandal, P. A review of wind power and wind speed forecasting methods with different time horizons. **2010**. DOI: 10.1109/naps.2010.5619586.

(12) Barthelmie, R. J.; Jensen, L. E. Evaluation of wind farm efficiency and wind turbine wakes at the Nysted offshore wind farm. *Wind Energy* **2010**, *13* (6), 573-586. DOI: 10.1002/we.408.

(13) Gharbi, O.; Tran, M. T. T.; Tribollet, B.; Turmine, M.; Vivier, V. Revisiting cyclic voltammetry and electrochemical impedance spectroscopy analysis for capacitance measurements. *Electrochimica Acta* **2020**, *343*, 136109. DOI: https://doi.org/10.1016/j.electacta.2020.136109.

(14) Ylilammi, M.; Ylivaara, O. M. E.; Puurunen, R. L. Modeling growth kinetics of thin films made by atomic layer deposition in lateral high-aspect-ratio structures. *Journal of Applied Physics* **2018**, *123* (20), 205301. DOI: 10.1063/1.5028178.

(15) Moitzheim, S.; Balder, J. E.; Ritasalo, R.; Ek, S.; Poodt, P.; Unnikrishnan, S.; De Gendt, S.; Vereecken, P. M. Toward 3D Thin-Film Batteries: Optimal Current-Collector Design and Scalable Fabrication of TiO₂ Thin-Film Electrodes. *ACS Applied Energy Materials* **2019**, *2* (3), 1774-1783. DOI: 10.1021/acsaem.8b01905.

(16) Ding, M.; Zhai, J.; Zeng, P.; Zhang, C.; Ping, Y. Introduction of amorphous TiO2 coating layer to improve the lithium storage of SiO2 nanospheres anode. *Ionics* **2022**, *28* (3), 1081-1089. DOI: 10.1007/s11581-021-04435-w. Madian, M.; Klose, M.; Jaumann, T.; Gebert, A.; Oswald, S.; Ismail, N.; Eychmüller, A.; Eckert, J.; Giebeler, L. Anodically fabricated TiO₂–SnO₂nanotubes and their application in lithium ion batteries. *Journal of Materials Chemistry A* **2016**, *4* (15), 5542-5552. DOI: 10.1039/c6ta00182c.

(17) Madian, M.; Giebeler, L.; Klose, M.; Jaumann, T.; Uhlemann, M.; Gebert, A.; Oswald, S.; Ismail, N.; Eychmüller, A.; Eckert, J. Self-Organized TiO₂/CoO Nanotubes as Potential Anode Materials for Lithium Ion Batteries. *ACS Sustainable Chemistry & Engineering* **2015**, *3* (5), 909-919. DOI: 10.1021/acssuschemeng.5b00026.

(18) Sciences, T. R. S. A. o. Press release: The Nobel Prize in Chemistry 2019. In *They created a rechargeable world*, Nevelius, E., Ed.; https://www.nobelprize.org/prizes/chemistry/2019/press-release/, 2019; p 1.

(19) Krämer, K. *The lithium pioneers*. Chemsitry World, 2019. https://www.chemistryworld.com/features/the-lithium-pioneers/4010510.article (accessed 2022 25.01).

(20) Placke, T.; Kloepsch, R.; Dühnen, S.; Winter, M. Lithium ion, lithium metal, and alternative rechargeable battery technologies: the odyssey for high energy density. *Journal of Solid State Electrochemistry* **2017**, *21* (7), 1939-1964. DOI: 10.1007/s10008-017-3610-7.

(21) Kotal, M.; Jakhar, S.; Roy, S.; Sharma, H. K. Cathode materials for rechargeable lithium batteries: Recent progress and future prospects. *Journal of Energy Storage* **2021**, 103534. DOI: 10.1016/j.est.2021.103534.

(22) John B. Goodenough, A. K. P., K. S. Nanjundaswamy, Christian Masquelier. Cathode materials for secondary (rechargeable) lithium batteries. United States 5 910 382, 1996.

(23) Reddy, M. V.; Mauger, A.; Julien, C. M.; Paolella, A.; Zaghib, K. Brief History of Early Lithium-Battery Development. *Materials* **2020**, *13* (8), 1884. DOI: 10.3390/ma13081884.

(24) Raj, H.; Sil, A. Effect of carbon coating on electrochemical performance of LiFePO4 cathode material for Li-ion battery. *Ionics* **2018**, *24* (9), 2543-2553. DOI: 10.1007/s11581-017-2423-0.

(25) Park, J.; Xu, Z.-L.; Kang, K. Solvated Ion Intercalation in Graphite: Sodium and Beyond. *Frontiers in Chemistry* **2020**, *8*, Review. DOI: 10.3389/fchem.2020.00432.

(26) Asenbauer, J.; Eisenmann, T.; Kuenzel, M.; Kazzazi, A.; Chen, Z.; Bresser, D. The success story of graphite as a lithium-ion anode material – fundamentals, remaining challenges, and recent developments including silicon (oxide) composites. *Sustainable Energy & Fuels* **2020**, *4* (11), 5387-5416. DOI: 10.1039/d0se00175a.

(27) Mauger, A.; Julien, C. M.; Goodenough, J. B.; Zaghib, K. Tribute to Michel Armand: from Rocking Chair – Li-ion to Solid-State Lithium Batteries. *Journal of The Electrochemical Society* **2020**, *167* (7), 070507. DOI: 10.1149/2.0072007jes.

(28) Jin, Y.; Kneusels, N.-J. H.; Marbella, L. E.; Castillo-Martínez, E.; Magusin, P. C. M. M.; Weatherup, R. S.; Jónsson, E.; Liu, T.; Paul, S.; Grey, C. P. Understanding Fluoroethylene Carbonate and Vinylene Carbonate Based Electrolytes for Si Anodes in Lithium Ion Batteries with NMR Spectroscopy. *Journal of the American Chemical Society* **2018**, *140* (31), 9854-9867. DOI: 10.1021/jacs.8b03408.

(29) Gogotsi, Y.; Penner, R. M. Energy Storage in Nanomaterials – Capacitive, Pseudocapacitive, or Battery-like? *ACS Nano* **2018**, *12* (3), 2081-2083. DOI: 10.1021/acsnano.8b01914.

(30) Muzaffar, A.; Ahamed, M. B.; Deshmukh, K.; Thirumalai, J. A review on recent advances in hybrid supercapacitors: Design, fabrication and applications. *Renewable and Sustainable Energy Reviews* **2019**, *101*, 123-145. DOI: 10.1016/j.rser.2018.10.026.

(31) Naskar, P.; Kundu, D.; Maiti, A.; Chakraborty, P.; Biswas, B.; Banerjee, A. Frontiers in Hybrid Ion Capacitors: A Review on Advanced Materials and Emerging Devices. *ChemElectroChem* **2021**, *8* (8), 1393-1429. DOI: 10.1002/celc.202100029.

(32) Amatucci, G. G.; Badway, F.; Du Pasquier, A.; Zheng, T. An Asymmetric Hybrid Nonaqueous Energy Storage Cell. *Journal of The Electrochemical Society* **2001**, *148* (8), A930. DOI: 10.1149/1.1383553.

(33) George, S. M. Atomic Layer Deposition: An Overview. *Chemical Reviews* **2010**, *110* (1), 111-131. DOI: 10.1021/cr900056b.

(34) Puurunen, R. L. A Short History of Atomic Layer Deposition: Tuomo Suntola's Atomic Layer Epitaxy. *Chemical Vapor Deposition* **2014**, *20* (10-11-12), 332-344. DOI: 10.1002/cvde.201402012.

(35) O'Neill, B. J.; Jackson, D. H. K.; Lee, J.; Canlas, C.; Stair, P. C.; Marshall, C. L.; Elam, J. W.; Kuech, T. F.; Dumesic, J. A.; Huber, G. W. Catalyst Design with Atomic Layer Deposition. *ACS Catalysis* **2015**, *5* (3), 1804-1825. DOI: 10.1021/cs501862h.

(36) Cheah, S. K.; Perre, E.; Rooth, M.; Fondell, M.; Hårsta, A.; Nyholm, L.; Boman, M.; Gustafsson, T.; Lu, J.; Simon, P.; et al. Self-Supported Three-Dimensional Nanoelectrodes for Microbattery Applications. *Nano Letters* **2009**, *9* (9), 3230-3233. DOI: 10.1021/nl9014843.

(37) Longrie, D.; Deduytsche, D.; Detavernier, C. Reactor concepts for atomic layer deposition on agitated particles: A review. *Journal of Vacuum Science & Technology A: Vacuum, Surfaces, and Films* **2014**, *32* (1), 010802. DOI: 10.1116/1.4851676.

(38) Lai, S. Y.; Knudsen, K. D.; Sejersted, B. T.; Ulvestad, A.; Mæhlen, J. P.; Koposov, A. Y. Silicon Nanoparticle Ensembles for Lithium-Ion Batteries Elucidated by Small-Angle Neutron Scattering. *ACS Applied Energy Materials* **2019**, *2* (5), 3220-3227. DOI: 10.1021/acsaem.9b00071.

(39) University, B. *How do lithium batteries work*. CADEX, 2021. https://batteryuniversity.com/article/bu-204-how-do-lithium-batteries-work (accessed 2022 26.01).

(40) Whittingham, M. S. Intercalation chemistry and energy storage. *Journal of Solid State Chemistry* **1979**, *29* (3), 303-310. DOI: 10.1016/0022-4596(79)90187-7.

(41) Chen, X.; Li, H.; Yan, Z.; Cheng, F.; Chen, J. Structure design and mechanism analysis of silicon anode for lithium-ion batteries. *Science China Materials* **2019**, *62* (11), 1515-1536. DOI: 10.1007/s40843-019-9464-0.

(42) Priyono, B.; Winowatan, P. W.; Syahrial, A. Z.; Faizah; Subhan, A. Optimizing the performance of Li₄Ti₅O₁₂/LTO by addition of silicon microparticle in half cell litium-ion battery anode. *IOP Conference Series: Earth and Environmental Science* **2018**, *105*, 012121. DOI: 10.1088/1755-1315/105/1/012121.

(43) McKinnon, W. R. Insertion electrodes I: Atomic and electronic structure of the hosts and their insertion compounds. In *Solid State Electrochemistry*, Bruce, P. G. Ed.; Chemistry of Solid State Materials, Cambridge University Press, 1994; pp 163-198.

(44) Moitzheim, S.; De Gendt, S.; Vereecken, P. M. Investigation of the Li-Ion Insertion Mechanism for Amorphous and Anatase TiO₂Thin-Films. *Journal of The Electrochemical Society* **2019**, *166* (2), A1-A9. DOI: 10.1149/2.1091816jes.

(45) Phadatare, M.; Patil, R.; Blomquist, N.; Forsberg, S.; Örtegren, J.; Hummelgård, M.; Meshram, J.; Hernández, G.; Brandell, D.; Leifer, K.; et al. Silicon-Nanographite Aerogel-Based Anodes for High Performance Lithium Ion Batteries. *Scientific Reports* **2019**, *9* (1). DOI: 10.1038/s41598-019-51087-y.

(46) Lewandowski, A.; Świderska-Mocek, A. Ionic liquids as electrolytes for Li-ion batteries—An overview of electrochemical studies. *Journal of Power Sources* **2009**, *194* (2), 601-609. DOI: 10.1016/j.jpowsour.2009.06.089.

(47) Nakai, H.; Kubota, T.; Kita, A.; Kawashima, A. Investigation of the Solid Electrolyte Interphase Formed by Fluoroethylene Carbonate on Si Electrodes. *Journal of The Electrochemical Society* **2011**, *158* (7), A798-A801. DOI: 10.1149/1.3589300.

(48) Westerlund, S.; Ekstam, L. Capacitor theory. *IEEE Transactions on Dielectrics and Electrical Insulation* **1994**, *1* (5), 826-839. DOI: 10.1109/94.326654.

(49) Biesheuvel, M.; Porada, S.; Dykstra, J. *The difference between Faradaic and non-Faradaic electrode processes*; 2018.

(50) Maher, M.; Hassan, S.; Shoueir, K.; Yousif, B.; Abo-Elsoud, M. E. A. Activated carbon electrode with promising specific capacitance based on potassium bromide redox additive electrolyte for supercapacitor application. *Journal of Materials Research and Technology* **2021**, *11*, 1232-1244. DOI: 10.1016/j.jmrt.2021.01.080.

(51) Stc, H. Characterization of Activated Carbons Produced from Oleaster Stones. InTech, 2011.

(52) Burt, R.; Birkett, G.; Zhao, X. S. A review of molecular modelling of electric double layer capacitors. *Physical Chemistry Chemical Physics* **2014**, *16* (14), 6519. DOI: 10.1039/c3cp55186e.

(53) Nilsen, O.; Karlsen, O. B.; Kjekshus, A.; Fjellvåg, H. Simulation of growth dynamics in atomic layer deposition. Part I. Amorphous films. *Thin Solid Films* **2007**, *515* (11), 4527-4537. DOI: https://doi.org/10.1016/j.tsf.2006.11.023.

(54) Killi, V. A.-L. K. Tynne filmer av ruthenater med atomlagsdeposisjon (ALD). The University of Oslo, DUO.uio.no, 2020. https://www.duo.uio.no/handle/10852/79794?show=full (accessed 25.01.2022).

(55) Palagonia, M. S.; Erinmwingbovo, C.; Brogioli, D.; La Mantia, F. Comparison between cyclic voltammetry and differential charge plots from galvanostatic cycling. *Journal of Electroanalytical Chemistry* **2019**, *847*, 113170. DOI: 10.1016/j.jelechem.2019.05.052.

(56) Elgrishi, N.; Rountree, K. J.; McCarthy, B. D.; Rountree, E. S.; Eisenhart, T. T.; Dempsey, J. L. A Practical Beginner's Guide to Cyclic Voltammetry. *Journal of Chemical Education* **2018**, *95* (2), 197-206. DOI: 10.1021/acs.jchemed.7b00361.

(57) Tiurin, O.; Ein-Eli, Y. A Critical Review: The Impact of the Battery Electrode Material Substrate on the Composition and Properties of Atomic Layer Deposition (ALD) Coatings. *Advanced materials interfaces* **2019**, *6* (24), 1901455-n/a. DOI: 10.1002/admi.201901455.

(58) 1-Methyl-2-pyrrolidinone. https://pubchem.ncbi.nlm.nih.gov/compound/1-Methyl-2-pyrrolidinone#datasheet=LCSS&section=GHS-Classification&fullscreen=true (accessed.

(59) Aarik, J.; Aidla, A.; Mändar, H.; Uustare, T. Atomic layer deposition of titanium dioxide from TiCl4 and H2O: investigation of growth mechanism. *Applied Surface Science* **2001**, *172* (1), 148-158. DOI: https://doi.org/10.1016/S0169-4332(00)00842-4.

(60) Niemelä, J.-P.; Marin, G.; Karppinen, M. Titanium dioxide thin films by atomic layer deposition: a review. *Semiconductor Science and Technology* **2017**, *32* (9), 093005. DOI: 10.1088/1361-6641/aa78ce.

(61) Calcagno, G.; Lotsari, A.; Dang, A.; Lindberg, S.; Palmqvist, A. E. C.; Matic, A.; Cavallo, C. Fast charging negative electrodes based on anatase titanium dioxide beads for highly stable Li-ion capacitors. *Materials Today Energy* **2020**, *16*, 100424. DOI: 10.1016/j.mtener.2020.100424.

(62) Porro, S.; Jasmin, A.; Bejtka, K.; Conti, D.; Perrone, D.; Guastella, S.; Pirri, C. F.; Chiolerio, A.; Ricciardi, C. Low-temperature atomic layer deposition of TiO2 thin layers for the processing of memristive devices. *Journal of Vacuum Science & Technology A: Vacuum, Surfaces, and Films* **2016**, *34* (1), 01A147. DOI: 10.1116/1.4938465.

(63) Lai, S. Y.; Mæhlen, J. P.; Preston, T. J.; Skare, M. O.; Nagell, M. U.; Ulvestad, A.; Lemordant, D.; Koposov, A. Y. Morphology engineering of silicon nanoparticles for better performance in Li-ion battery anodes. *Nanoscale Advances* **2020**, *2* (11), 5335-5342. DOI: 10.1039/d0na00770f.

(64) Jerliu, B.; Hüger, E.; Dörrer, L.; Seidlhofer, B. K.; Steitz, R.; Horisberger, M.; Schmidt, H. Lithium insertion into silicon electrodes studied by cyclic voltammetry and operando neutron reflectometry. *Physical Chemistry Chemical Physics* **2018**, *20* (36), 23480-23491. DOI: 10.1039/c8cp03540g. Chen, P.; Huang, W.; Liu, H.; Cao, Z.; Yu, Y.; Liu, Y.; Shan, Z. Enhanced cyclability of silicon anode via synergy effect of polyimide binder and conductive polyacrylonitrile. *Journal of Materials Science* **2019**, *54* (12), 8941-8954. DOI: 10.1007/s10853-019-03518-4.

(65) Liu, D.; Yu, Q.; Liu, S.; Qian, K.; Wang, S.; Sun, W.; Yang, X.-Q.; Kang, F.; Li, B. Evolution of Solid Electrolyte Interface on TiO₂ Electrodes in an Aqueous Li-Ion Battery Studied Using Scanning Electrochemical Microscopy. *The Journal of Physical Chemistry C* **2019**, *123* (20), 12797-12806. DOI: 10.1021/acs.jpcc.9b01412.

(66) Jilani, A.; Abdel-Wahab, M. S.; Hammad, A. H. Advance Deposition Techniques for Thin Film and Coating. InTech, 2017.

(67) Baptista, A.; Silva, F.; Porteiro, J.; Míguez, J.; Pinto, G. Sputtering Physical Vapour Deposition (PVD) Coatings: A Critical Review on Process Improvement and Market Trend Demands. *Coatings* **2018**, *8* (11), 402. DOI: 10.3390/coatings8110402.

(68) Desu, S. B. Ultra-thin TiO2 films by a novel method. *Materials Science and Engineering: B* **1992**, *13* (4), 299-303. DOI: https://doi.org/10.1016/0921-5107(92)90132-S.

(69) Ylivaara, O. M. E.; Langner, A.; Liu, X.; Schneider, D.; Julin, J.; Arstila, K.; Sintonen, S.; Ali, S.; Lipsanen, H.; Sajavaara, T.; et al. Mechanical and optical properties of as-grown and

thermally annealed titanium dioxide from titanium tetrachloride and water by atomic layer deposition. *Thin Solid Films* **2021**, *732*, 138758. DOI: https://doi.org/10.1016/j.tsf.2021.138758.

(70) Ritala, M.; Leskelä, M.; Nykänen, E.; Soininen, P.; Niinistö, L. Growth of titanium dioxide thin films by atomic layer epitaxy. *Thin Solid Films* **1993**, *225* (1), 288-295. DOI: https://doi.org/10.1016/0040-6090(93)90172-L.

(71) Aarik, J.; Aidla, A.; Uustare, T.; Sammelselg, V. Morphology and structure of TiO2 thin films grown by atomic layer deposition. *Journal of Crystal Growth* **1995**, *148* (3), 268-275. DOI: https://doi.org/10.1016/0022-0248(94)00874-4.

(72) Szeghalmi, A.; Helgert, M.; Brunner, R.; Heyroth, F.; Gösele, U.; Knez, M. Atomic layer deposition of Al_2O_3 and TiO_2 multilayers for applications as bandpass filters and antireflection coatings. **2009**, 1727. DOI: 10.1364/AO.48.001727.

(73) Meng, X.; Geng, D.; Liu, J.; Li, R.; Sun, X. Controllable synthesis of graphene-based titanium dioxide nanocomposites by atomic layer deposition. *Nanotechnology* **2011**, *22* (16), 165602. DOI: 10.1088/0957-4484/22/16/165602.

(74) Reinke, M.; Kuzminykh, Y.; Hoffmann, P. Surface Reaction Kinetics of Titanium Isopropoxide and Water in Atomic Layer Deposition. *The Journal of Physical Chemistry C* **2016**, *120* (8), 4337-4344. DOI: 10.1021/acs.jpcc.5b10529.

(75) Madian, M.; Eychmüller, A.; Giebeler, L. Current Advances in TiO2-Based Nanostructure Electrodes for High Performance Lithium Ion Batteries. *Batteries* **2018**, *4* (1), 7. DOI: 10.3390/batteries4010007.

(76) Wang, F.; Zhang, S.; Zhang, J.; Han, M.; Pan, G.; Chen, M. Rational synthesis of silicon into polyimide-derived hollow electrospun carbon nanofibers for enhanced lithium storage. *e-Polymers* **2020**, *20* (1), 491-499. DOI: 10.1515/epoly-2020-0023. Wang, Y.; Zhang, J. Ultrafine TiO2(B) nanowires for ultrahigh-rate lithium-ion batteries. *Ionics* **2020**, *26* (3), 1159-1164. DOI: 10.1007/s11581-019-03291-z.

(77) Ha, Y.; Finegan, D. P.; Colclasure, A. M.; Trask, S. E.; Keyser, M. Evaluating temperature dependent degradation mechanisms of silicon-graphite electrodes and the effect of fluoroethylene carbonate electrolyte additive. *Electrochimica Acta* **2021**, *394*, 139097. DOI: 10.1016/j.electacta.2021.139097.

(78) Aurbach, D.; Talyosef, Y.; Markovsky, B.; Markevich, E.; Zinigrad, E.; Asraf, L.; Gnanaraj, J. S.; Kim, H.-J. Design of electrolyte solutions for Li and Li-ion batteries: a review. *Electrochimica Acta* **2004**, *50* (2-3), 247-254. DOI: 10.1016/j.electacta.2004.01.090.

(79) Kitz, P. G.; Lacey, M. J.; Novák, P.; Berg, E. J. Operando investigation of the solid electrolyte interphase mechanical and transport properties formed from vinylene carbonate and fluoroethylene carbonate. *Journal of Power Sources* **2020**, *477*, 228567. DOI: 10.1016/j.jpowsour.2020.228567.